ABSTRACT

Title of Dissertation:	INTENSE LASER INTERACTIONS IN THE ATMOSPHERE
	Gavin Blair Doctor of Philosophy, 2025
Dissertation directed by:	Professor Phillip Sprangle Department of Physics Department of Electrical and Computer Engineering

This dissertation consists of three research projects which deal with laser-matter interactions and potential applications of the processes.

In the first part of this dissertation, I present, analyze, and simulate a mechanism for remotely generating RF radiation in air by using a laser pulse train (LPT). The LPT ionizes the air through photo detachment and collisional ionization, generating a plasma filament. The ponderomotive forces associated with the LPT drive radial and longitudinal plasma currents. These plasma currents generate radiation at the LPT repetition rate, which can be tuned in the 0.5 – 6.0 GHz range. Of particular interest is the RF generation in the 1.4-1.7 GHz regime, which is the operating frequency range of all GPS signals. The analysis and simulation results of the RF radiation are shown to be in agreement with experimental data. The experiments were performed in collaboration with the theory and computational work at the University of Maryland.

The second part of this dissertation analyzes and simulates long range propagation and stability of laser pulses traveling vertically through the turbulent atmosphere. By tailoring the initial laser pulse parameters, the pulse can be focused transversely and longitudinally at remote locations (>50 km) with intensity enhancements of > 10^3. In addition, nonlinear self-focusing of the laser pulse and dispersion lead to the growth of a hybrid modulation-filamentation instability, which causes both transverse and longitudinal pulse breakup. This hybrid instability is analyzed and numerically simulated for pulses propagating in the atmosphere. The potential application of this research is on the long-range generation of RF signals in a turbulent atmosphere.

The third part of this dissertation presents a mechanism for generating tunable low frequency radiation in the ionosphere (F layer) and propagating the low frequency signal back to the ground. This process has the potential to be used as a new type of over-the-horizon (OTH) radar which would be compact, mobile, and far less costly than conventional OTH systems. Conventional OTH radar systems utilize dipole antenna arrays that span multiple kilometers, and can cost well over a billion dollars. Most major countries employ conventional OTH radar systems. The proposed new mechanism relies on a ground-based, modulated RF source. By tuning the modulation frequency to the local plasma frequency in the ionosphere (F layer), a current can be resonantly excited by the ponderomotive force of the modulated signal. This current grows in time and generates a low frequency signal at the local plasma frequency, which is in the MHz range. The low frequency signal propagates back to the ground, far from the source, where it can be detected. We find that using available RF sources, i.e., gyrotrons, detectable low frequency signals can be generated and detected on the ground. The minimum detectable intensity is ~10^{-18} W/m^2, though the theoretical limit may be lower. This mechanism has the potential to detect OTH objects using a compact, mobile, and far less expensive system than presently exists.

INTENSE LASER INTERACTIONS IN THE ATMOSPHERE

by

Gavin Blair

Dissertation submitted to the Faculty of the Graduate School of the
University of Maryland, College Park, in partial fulfillment
of the requirements for the degree of
Doctor of Philosophy
2025

Advisory Committee:
Professor Phillip Sprangle, Chair
Professor Thomas Antonsen
Professor Wendell Hill III (Dean’s Representative)
Professor Howard Milchberg
Professor Thomas Murphy

Dedication

To my parents, Joe and Julie, and siblings, Ian, Anna, and Colin, for always supporting me.

Acknowledgements

It would require another dissertation for me to appropriately thank those who have helped me along my path towards a PhD. So, I will just list a few here who are especially deserving of acknowledgements.

First, I would like to thank my PhD advisor, Prof. Phillip Sprangle, for his help and support. It would be difficult to find a more helpful advisor. He was always available when I had questions and always pushed me to leave no stone unturned in research. I also appreciated his advice on how to deal with alligators in your life.

I would also like to thank Dr. Bahman Hafizi and Dr. Vladimir Markov. I had the privilege of working closely with both of them on different research projects throughout my PhD. Dr. Markov kept our research grounded in reality with his experimental work. Dr. Hafizi helped me examine problems from new angles. They both provided fresh perspectives and I am extremely appreciative of their collaborations, discussions, and continued support in research.

I would also like to thank Prof. Tom Antonsen, Prof. Howard Milchberg, Prof. Tom Murphy, and Prof. Wendell Hill for serving on my committee. I know that it is not an insignificant task to serve on a dissertation committee, and I appreciate the time that you are committing to do so.

Additionally, I would like to thank my parents, Joe and Julie, and siblings, Ian, Anna, and Colin. They have always supported my goals of pursuing a PhD in physics, even if they do not always understand what it is that I am doing. I would like to acknowledge my friends who have supported me as well, especially those who have listened to me give countless unsolicited lectures on physics on long bike rides.

Finally, I would like to thank the University of Maryland and the funding agencies who have supported my research. Those agencies include the U.S. Office of Naval Research (in particular Quentin Saulter, Directed Energy program manager), the Air Force Office of Scientific Research, the Army Research Office, and the National Defense Science and Engineering Graduate Research Fellowship, which supported me for 3 years of my PhD.

Table of Contents

List of Tables

List of Figures

List of Abbreviations

RF – Radiofrequency

LPT – Laser pulse train

OTH – Over-the-horizon

GPS – Global positioning system

GVD – Group velocity dispersion

LEO – Low-earth-orbit

ICBM – Intercontinental ballistic missile

HF – High frequency

Chapter 1: Introduction

This dissertation consists of three research projects dealing with laser interactions in the atmosphere and the applications of these processes.

1. **RF Generation by Laser Pulse Trains in Air** (Chapter 2): published in Physical Review E [1] and the Journal of Directed Energy [2]

In the second chapter of this dissertation, a method for generating RF radiation using low-intensity laser pulse trains (LPTs) is presented. The LPT ionizes the air, first through photo detachment of ambient negative ions, i.e., O_2^-, and then through collisional (avalanche) ionization. The ambient free electron density in the atmosphere is not high enough to initiate collisional ionization. However, the ambient negative ion density, O_2^-, is quite high, and after the negative ions are photo detached, the free electron density is high enough for collisional ionization to occur. This ionization process can generate a plasma filament with an electron density near air density. The micropulses of the LPT drive oscillations of the electrons in the plasma filament by the ponderomotive force. Electrons are driven off-axis by the radial ponderomotive force and return on-axis by the resulting space charge field. The electron current oscillations generate radiation at the micropulse repetition rate. The micropulse repetition rate can be tuned to cover the entire GPS regime.

2. **Stability and Propagation of Laser Pulses in the Atmosphere** (Chapter 3): published in Physical Review A [3]

In the third chapter, the propagation and stability of laser pulses over long distances is analyzed and numerically simulated. The long-range propagation model is for pulses propagating vertically over distances >50 km. Envelope equations for the laser spot size and pulse duration are derived, which include the effects of linear and nonlinear dispersion, turbulence, and nonlinear self-focusing. The change in air density, dispersion, and the nonlinear refractive index of air with altitude is included in the model. By properly tailoring the pulse parameters, i.e., the initial wavefront curvature, chirp, and ratio of laser power to nonlinear focusing power, the pulse can be focused at remote locations with a significant intensity enhancement. The stability of the laser pulse is also analyzed. The solution of the envelope equations is treated as a dynamic equilibrium for the system. The dynamic equilibrium solution is perturbed, and the growth of the perturbation is studied. A dispersion relation describing the longitudinal growth of the perturbation is derived. The perturbation leads to a hybrid filamentation-modulation instability, which causes the pulse to break up both transversely and longitudinally. Simulation results for the hybrid instability are presented which show the beams break up transversely into beamlets, each with a power approximately equal to the nonlinear focusing power.

3. **Parametric Frequency Conversion in the Ionosphere for Over-the-Horizon Radar** (Chapter 4): published in Physical Review Applied [4]

The fourth chapter presents a mechanism for generating low frequency signals in the ionosphere which could be used for over-the-horizon (OTH) radar or measuring ionospheric parameters. The mechanism relies on a ground-based, modulated, RF source, which is directed into the ionosphere. The modulation of the source is tuned to the local plasma frequency in the ionosphere and resonantly drives plasma oscillations. The plasma oscillations emit radiation at the local plasma frequency, which is in the range of 3-10 MHz in the F layer of the ionosphere. These low frequency signals then propagate back to the ground where they can be detected. The signals can also propagate back to the detectors via surface waves on seawater. This mechanism provides a compact, mobile, and low-cost alternative to conventional OTH radar systems, which cost billions of dollars and can span many miles.

Chapter 2: RF Generation by Laser Pulse Trains in Air

2.1. Introduction

There has been a great deal of work done in recent decades on the generation of plasma filaments in air by high-intensity, ultra-short laser pulses [5-18]. In these studies, the laser pulse duration was typically in the multi femtosecond to picosecond regime and the intensities high enough to induce tunneling ionization ($10^{18} - 10^{19}\,\mathrm{W/m^2}$) in air. Recent work has shown that multiple laser pulses can be generated and used to generate extended plasma filaments [19,20]. For example, 30 laser pulses of duration $\sim 30\,\mathrm{fs}$, separated by $\sim 0.5\ \mathrm{ns}$ and having a total energy of $\sim 600\ \mathrm{mJ}$, were used to generate plasma filaments in air [21].

Laser-plasma filament interactions have been used to generate terahertz (THz) radiation. For example, THz radiation has been produced by two-color laser pulses interacting in ionized air [22,23].

The generation of radiation by the interaction of laser pulses with plasma filaments is also of interest because of its potential applications in remote sensing, communications, and electronic countermeasures [22-28].

The present work focuses on the generation of radiofrequency (RF) radiation in air by low intensity laser pulse trains (LPT). The O_2^- ions, which are generated by ambient levels of ionizing radiation, play a major role in the initiation of the plasma filaments. The negative ions are readily photo detached by the low intensity LPT. For example, O_2^- ions have a low ionization potential, i.e., $0.46\ \mathrm{eV}$ [29], and are ionized by the low intensity LPT. The photo detachment of the negative ions provide seed electrons for collisional (avalanche) ionization to take place at relatively low laser intensities [26,27].

In this chapter, I present analysis and numerical simulations of a LPT propagating and ionizing air by a combination of photo detachment and collisional ionization processes. The ionized electrons are acted on by ponderomotive and space charge forces and undergo oscillations in the radial and longitudinal directions. The oscillating currents generate RF radiation. As micropulses propagate through the plasma filament, ponderomotive forces drive the electrons radially outward, and forward and backward, and space charge forces tend to drive the electrons radially inward. The oscillating current density generates RF radiation. The RF frequency spectrum is determined by the LPT repetition rate and micropulse duration. The fractional linewidth scales as the inverse of the number of micro-pulses in the LPT. For example, for a micropulse separation time of 650 ps, the fundamental RF frequency is 1.6 GHz. By varying the LPT repetition rate and micropulse duration, the RF frequency spectrum can be varied over a wide range.

The proposed method has the potential to generate directed and tunable RF in the atmosphere at extended ranges. Preliminary experimental studies, conducted by Dr. Vladimir Markov at Advanced Systems and Technologies, Inc., support the proposed RF generation mechanism. Since the RF wavelength can cover the entire GPS spectrum, this approach has potential applications in electronic communications and countermeasures.

2.2. Ionization and RF Generation Model

In our model, the low intensity LPT propagates in air and initiates photo detachment of the ambient negative molecular ions, e.g., O_2^- ions. The photo detached electrons become the seed electrons for collisional ionization, which becomes the dominant ionization process after a few pulses of the LPT. The effective ponderomotive field associated with the LPT accelerates electrons radially outward, and forward and backward, creating a radial space charge field and a current

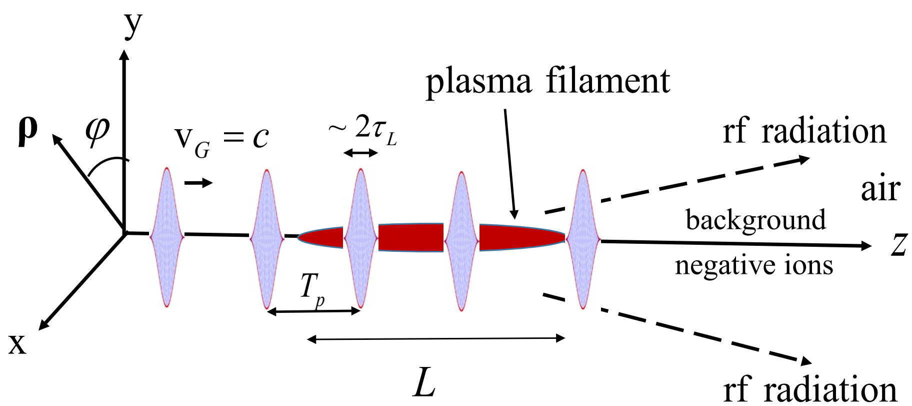

Figure 2.1. Schematic overview of the LPT generating a plasma filament in air by a combination of photo detachment of background negative ions and collisional ionization processes. The radial plasma currents induced by the ponderomotive LPT fields generate RF radiation in the forward and backward directions.

density. The space charge field is created by the radial flow of electrons and the stationary positive ions. The space charge field together with the ponderomotive field drive electron oscillations having a frequency related to the laser pulse separation time. The RF radiation has a fundamental frequency given by $1/T_p$, where T_p is the micro-pulse separation time, as well as harmonics. The LPT undergoes defocusing as the plasma filament develops. This defocusing limits further ionization and limits the LPT-plasma interaction length. Figure 2.1 shows a schematic overview of the process of generating a plasma filament in the air through a combination of photo detachment and collisional ionization from the LPT. The LPT and plasma fields induce currents that generate directed RF radiation.

2.2.1. Laser Pulse Train

The LPT interacts with the ionized plasma electrons in the region from $z = 0$ to $z = L$, where L is the length of the plasma filament. The LPT intensity consists of multiple, equally spaced micropulses. The micropulse intensity, in cylindrical geometry, is

$$I_{pulse}(\rho,\tau) = I_{peak}\exp(-2\rho^2/\rho_0^2)\exp(-2\tau^2/\tau_L^2), \tag{2.1}$$

where I_{peak} is the peak intensity, ρ_0 is the spot size, $\tau = t - z/c$, and τ_L is the micropulse duration. The energy in a single laser micropulse is given by $W_{pulse} = (\pi/2)^{3/2}\rho_0^2\tau_L I_{peak}$.

The LPT consists of $N_p >> 1$ micropulses separated in time by $T_p > \tau_L$. The Fourier series representation of the injected probe pulse train is

$$I_{LPT}(\rho, z, \tau) = I_0 \exp(-2\rho^2/\rho_0^2)\left(1+\sum_{n=1}^{\infty} g_n \cos(\omega_n(\tau - \tau_L/2))\right)\mathrm{T}(\tau), \qquad (2.2)$$

where $I_0 = \sqrt{\pi/2}(\tau_L/T_p)I_{peak}$, the Fourier intensity coefficients are $g_n = 2\exp(-(\omega_n\tau_L/2)^2/2)$, $\omega_n = 2\pi n/T_p$, $n = 0,1,2,...$, $\mathrm{T}(\tau) = \Theta(\tau) - \Theta(\tau - T)$, and $\Theta(\tau)$ is a Heaviside step function. The LPT has an axial electric field which is neglected since its amplitude is down by the factor $\lambda_0/(2\pi\rho_0) << 1$. A typical plot of the LPT used in our simulations is shown in Fig. 2.2, where the laser parameters are taken from Table 2.1.

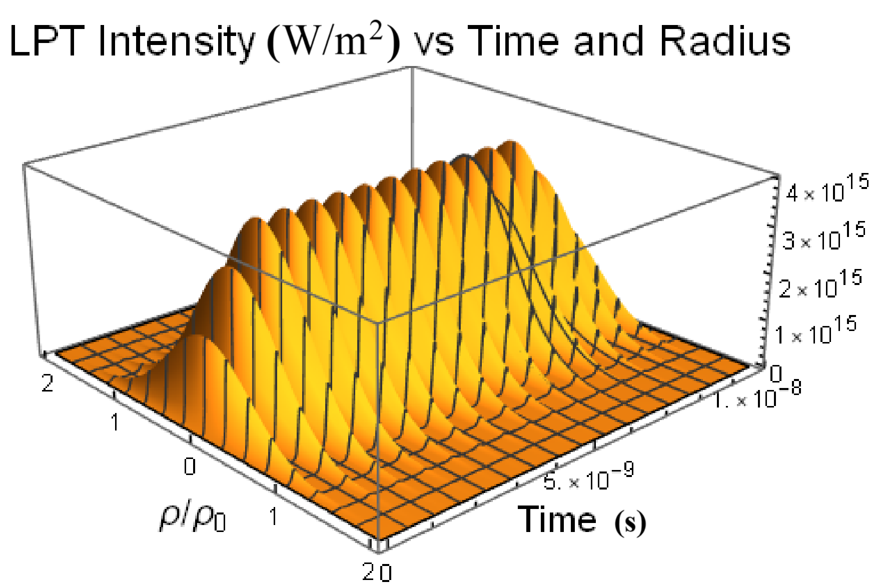

Figure 2.2. LPT intensity I_{LPT} verses ρ/ρ_0 and $\tau = t - z/\mathrm{v}_G$. Parameters for this plot are $I_{peak} = 4\times10^{15}$ W/m^2, $\tau_L = 100$ ps, $T_p = 0.65$ ns, $\rho_0 = 100$ μm, and $N_p = 15$.

2.2.2. Photo Detachment and Collisional Ionization

Background ionizing radiation is the primary process through which negative ions are generated in air. Gamma rays, originating from cosmic and/or ground sources, can ionize air molecules. The ionized high-energy electrons cascade down to thermal energies and attach to, for example, oxygen molecules. A single MeV gamma ray can produce as many as $\sim 3\times10^4$ thermal electrons [11,30]. These electrons attach mainly to O_2 molecules to create O_2^- ions which have a relatively long lifetime. The background radiation disintegration rate, at ground level, is $Q_{rad}\sim10^7$ pairs/(m$^3-$s) which results in a negative ion density of $N_{O_2^-}\sim3\times10^9\ \mathrm{m}^{-3}$ [11]. The background density of free electrons is, however, far less than the negative ion density. The ionization potential of O_2^- is $0.46\,\mathrm{eV}$, while the photon energy for $\lambda_0=1\,\mu\mathrm{m}$ is $1.24\,\mathrm{eV}$. Therefore, O_2^- ions can be ionized by single-photon detachment and thus, provide seed electrons for collisional ionization to further increase the electron density. Multiphoton ionization can be neglected when these parameters are used because the ionization potential for O_2 is 12 eV, which would require 8-10 photons, and the laser intensity is far below the threshold for tunneling ionization (~10^{18} W/m^2).

The photo detachment rate for O_2^- is given by $\nu_{O_2^-}=\sigma_{ion}I/\left(\hbar\omega_0\right)$, where σ_{ion} is the ionization cross section, I is the intensity, and ω_0 is the frequency. The experimental value is $\sigma_{ion}\approx5\times10^{-23}\ \mathrm{m}^2$ for $\lambda_0=1\,\mu\mathrm{m}$ [29] and the single-photon detachment rate for O_2^- is $\nu_{O_2^-}[\mathrm{s}^{-1}]=2.5\times10^{-4}I(\rho,\tau)[\mathrm{W/m}^2]$. This rate is sufficient to deplete the O_2^- ions in the optical volume for intensities in the range of $10^{15}-10^{16}\ \mathrm{W/m}^2$.

The collisional ionization rate in air can be written in the form [31,32], $\nu_{col} = \nu_{col}(N_2) + \nu_{col}(O_2)$, where the rate for N_2 and O_2 is $\nu_{col} = \nu_X \left(T_e / U_X\right)^{3/2} \left(U_X / T_e + 2\right) \exp\left(-U_X / T_e\right)$, ν_X is a characteristic frequency for species, X, i.e., $\nu_{N_2} = 7.6\times10^{11}\,\mathrm{s}^{-1}$, $\nu_{O_2} = 10^{11}\,\mathrm{s}^{-1}$, T_e is the electron temperature in eV, and U_X is the molecular ionization potential for species X, i.e., $U_{N_2} \approx 15.6\,\mathrm{eV}$, $U_{O_2} \approx 12.1\,\mathrm{eV}$.

The electron collision frequency is the sum of the electron-neutral and electron-ion collision frequencies, i.e., $\Gamma = \nu_{en} + \nu_{ei}$. The electron-neutral collision frequency [31] is given by $\nu_{en}[\mathrm{s}^{-1}] = 2.8\times10^{6}\sigma_n[\mathrm{m}^2]N_n[\mathrm{m}^{-3}](T_e[\mathrm{eV}])^{1/2}$ where $\sigma_n \approx 10^{-20}$ m^2 is the molecular area. Setting the neutral molecular density equal to $N_n = N_{air} - N_e$, the electron-neutral collision frequency $\nu_{en}[\mathrm{s}^{-1}] = 2.8\times10^{-14}(N_{air}[\mathrm{m}^{-3}] - N_e[\mathrm{m}^{-3}])(T_e[\mathrm{eV}])^{1/2}$, where $N_{air} = 2.7\times10^{25}\,\mathrm{m}^{-3}$ is the air density. The electron-ion collision frequency is, for singly ionized plasmas, i.e., $N_i = N_e$, given by $\nu_{ei}[\mathrm{s}^{-1}] = 2.9\times10^{-11}N_e[\mathrm{m}^{-3}](T_e[\mathrm{eV}])^{-3/2}$, where the Coulomb logarithm was set equal to 10 [31].

2.2.3. Ponderomotive Force

The plasma currents that drive the RF radiation are induced by the ponderomotive forces associated with the LPT. The ponderomotive force is a second order force in the field amplitude. In the absence of collisions, the electromagnetic ponderomotive effective electric field (nonrelativistic limit) is given by [33,34]

$$\mathbf{E}_{pond}(\mathbf{r},t) = -\frac{q}{m\omega^2}\frac{1}{2}\nabla\left(\mathbf{E}\cdot\mathbf{E}\right), \tag{2.3}$$

where the terms on the right-hand side of Eq. (2.3) are averaged over an optical period, ω is the laser frequency, $\mathbf{E}$ is the electric field amplitude, m is the electron mass, and q is the electron charge. However, collisions may play an important role in determining the ponderomotive force. The ponderomotive force, when collisions are included, is

$$\mathbf{F}_{pond,DC} = -\frac{q^2}{m(\omega^2+\Gamma^2)}\left(\nabla\left|\hat{E}\right|^2 - 2\frac{\Gamma}{c}\left|\hat{E}\right|^2\hat{\mathbf{z}}\right). \tag{2.4}$$

where $\mathbf{E}(\mathbf{r},t) = \hat{\mathbf{E}}(\mathbf{r},t)\exp(-i\omega t) + c.c.$ and Γ is the electron collision frequency. The derivation of Eq. (2.4) is presented in Appendix A. In the absence of collisions, i.e., $\Gamma = 0$, Eq. (2.4) reduces to Eq. (2.3). This derivation is valid under the assumption that the longitudinal laser electric field is small compared to the transverse field, i.e., $E_x >> E_z$, which is true for the parameters considered here.

The first term of Eq. (2.4) is dominated by the radial term. For the micropulse, with an intensity given by Eq. (2.1), the transverse and longitudinal components of the effective ponderomotive electric fields are respectively

$$E_{pond,\rho} = E_P(\rho/\rho_0)\exp(-2\rho^2/\rho_0^2)\exp(-2\tau^2/\tau_L^2), \tag{2.5a}$$

$$E_{pond,z} = E_P(\Gamma\rho_0/2c)\exp(-2\rho^2/\rho_0^2)\exp(-2\tau^2/\tau_L^2), \tag{2.5b}$$

where $E_P = 2qZ_0 I_{peak}/(m\omega^2\rho_0)$. For the parameters used in the simulations, the radial ponderomotive field dominates the longitudinal field. The ratio between the two is $E_{pond,\rho}/E_{pond,z} = 2c\rho/\Gamma\rho_0^2$. In the parameter regime considered in this analysis, $2c >> \Gamma\rho_0$ so that the radial ponderomotive force due to the gradient term dominates.

Later in this section, we will present the case where the longitudinal force dominates the radial force. The collisional term in Eq. (2.4) can be important. For the parameters

$\Gamma \approx 10^{12} - 10^{13}$ s^{-1} and $\rho_0 > 100$ μm, the ratio between the radial and longitudinal terms approaches unity. It can be noted that the longitudinal term due to collisions comes from the $\mathbf{v} \times \mathbf{B}$ force term.

In the case of the LPT, with an intensity given in Eq. (2.2), the transverse and longitudinal components of the effective ponderomotive electric field are respectively

$$E_{LPT,\rho} = E_P \frac{I_0}{I_{peak}} \frac{\rho}{\rho_0} \exp(-2\rho^2 / \rho_0^2) \left(1 + \sum_{n=1}^{\infty} g_n \cos(\omega_n(\tau - \tau_L / 2))\right) \mathrm{T}(\tau), \quad (2.6a)$$

$$E_{LPT,z} = E_P \frac{I_0}{I_{peak}} \frac{\Gamma \rho_0}{2c} \exp(-2\rho^2 / \rho_0^2) \left(1 + \sum_{n=1}^{\infty} g_n \cos(\omega_n(\tau - \tau_L / 2))\right) \mathrm{T}(\tau). \quad (2.6b)$$

2.2.4. Fluid Equations

The fluid equations used to model the system are derived by taking moments of the Boltzmann equation. The Boltzmann equation for this system is given by

$$\left(\frac{\partial}{\partial t} + \mathbf{v} \cdot \nabla + \mathbf{a} \cdot \frac{\partial}{\partial \mathbf{v}}\right) f_e(\mathbf{r}, \mathbf{v}, t) = Q_{rad} \delta(\mathbf{v}) + \nu_{O_2^-} N_{O_2^-} \delta(\mathbf{v} - \mathbf{v}_0) + (\nu_{col} - \eta_A) f_e(\mathbf{r}, \mathbf{v}, t), \quad (2.7)$$

where $f_e(\mathbf{r}, \mathbf{v}, t)$ is the electron distribution function, $\mathbf{r} = (\rho, \varphi, z)$, $\mathbf{a} = q\mathbf{E} / m$, the electric field is comprised of both the effective ponderomotive field and the space charge field, and the ionized electrons are created with velocity $\mathbf{v}_0$. The moments of the Boltzmann equation can be evaluated where $N_e(\mathbf{r}, t) = \int_{-\infty}^{\infty} f_e(\mathbf{r}, \mathbf{v}, t) d^3\mathbf{v}$ is the electron density and $N_e(\mathbf{r}, t)\mathbf{V}(\mathbf{r}, t) = \int_{-\infty}^{\infty} \mathbf{v} f_e(\mathbf{r}, \mathbf{v}, t) d^3\mathbf{v}$ is the current density. Taking these moments and setting $\mathbf{v}_0 = 0$ yields.

$$\frac{\partial N_e}{\partial t} + \nabla \cdot (N_e \mathbf{V}) = Q_{rad} + \nu_{O_2^-} N_{O_2^-} + (\nu_{col} - \eta_A - \beta_e N_{ion}) N_e, \quad (2.8a)$$

$$\frac{\partial (N_e \mathbf{V})}{\partial t} + \nabla \cdot (N_e \mathbf{V}\mathbf{V}) = (q N_e / m)\left(\mathbf{E}_{sc}(\mathbf{r}, t) + \mathbf{E}_{pond}(\mathbf{r}, t)\right) + (\nu_{col} - \eta_A - \beta_e N_{ion}) N_e \mathbf{V}, \quad (2.8b)$$

where $\mathbf{V}$ is the electron fluid velocity, Q_{rad} is the background radioactivity ionization rate, $\nu_{O_2^-}$ is the photo detachment rate of O_2^- ions, $N_{O_2^-}$ is the density of O_2^- ions, ν_{col} is the collisional ionization rate of neutral molecules, $\eta_A \approx 10^8\ \mathrm{s}^{-1}$ is the electron reattachment rate, $\beta_e \approx 2\times10^{-14}\ \mathrm{m}^3/\mathrm{s}$ is the electron-ion recombination rate [31,35], N_{ion} is the positive ion density, $\mathbf{E}_{sc}$ is the space charge field, and $\mathbf{E}_{pond}$ is the effective ponderomotive field, i.e., Eq. (2.4). The thermal fluctuations in the fluid velocity are assumed to be small and are neglected. This assumption allows the stress tensor to be written in the simplified form of $\nabla\cdot\left(N_e\mathbf{VV}\right)$. The gradient terms in Eqs. (2.8a) and (2.8b) can be neglected if $\left|\mathbf{V}/c\right| << \rho_0/(c\tau_L)$.

Writing Eqs. (2.8a) and (2.8b) in component form and changing the variable $t\rightarrow\tau$ gives [24]

$$\frac{\partial N_e}{\partial\tau} = Q_{rad} + \nu_{O_2^-}N_{O_2^-} + \left(\nu_{col} - \eta_A - \beta_e N_{ion}\right)N_e, \tag{2.9a}$$

$$\frac{\partial V_\rho}{\partial\tau} = \frac{q}{m}\Big(E_{sc,\rho}(\rho,\tau) + E_{pond,\rho}(\rho,\tau)\Big) - \frac{V_\rho}{N_e}\Big(Q_{rad} - \nu_{O_2^-}N_{O_2^-}\Big), \tag{2.9b}$$

$$\frac{\partial V_z}{\partial\tau} = \frac{q}{m}\Big(E_{sc,z}(\rho,\tau) + E_{pond,z}(\rho,\tau)\Big) - \frac{V_z}{N_e}\Big(Q_{rad} - \nu_{O_2^-}N_{O_2^-}\Big). \tag{2.9c}$$

In obtaining Eqs. (2.9a), (2.9b), and (2.9c), the thermal fluctuations in the fluid velocity are assumed to be small and are neglected. In addition, the magnitude of the fluid velocity is $<< c$, so the pressure tensor and flux term in the time derivatives can be neglected. These approximations are checked and validated in the numerical simulations. For the remainder of the current analysis, I will assume that the radial ponderomotive force dominates the longitudinal force. This is true in the case of a small spot size and low collision frequency. Later in this section, I will present an analysis of the case where the longitudinal force dominates.

For the range of parameters used in the simulations, the ambipolar diffusion coefficient is estimated to be $D_A \sim 10^{-3}[\mathrm{m}^2/\mathrm{s}]$ and the diffusion time $r_0^2 / D_A \geq 1\mu\mathrm{s}$ [36]. The diffusion time is much longer than any time in the present process; therefore, diffusion effects are neglected.

An equation for the electron temperature can also be written

$$\frac{3}{2}\frac{\partial(N_e T_e)}{\partial\tau} = \langle \mathbf{J}\cdot\mathbf{E}\rangle - Q_{cool}, \tag{2.10}$$

where T_e is the electron temperature in units of eV, $\langle \mathbf{J}\cdot\mathbf{E}\rangle$ is the ohmic heating due to the LPT, and Q_{cool} contains all of the cooling terms. The ohmic heating term is given by $\langle \mathbf{J}\cdot\mathbf{E}\rangle = \omega_{pe}^2 \varepsilon_0 E_{eff}^2 / (2\nu_e)$ where $\omega_{pe} = \left(q^2 N_e / (m\varepsilon_0)\right)^{1/2}$ is the plasma frequency, $E_{eff} = (\nu_e / \omega_0) E_0 / (1 + (\nu_e / \omega_0)^2)^{1/2}$ is the effective laser field and $E_0 = (2 Z_0 I_0 / n_0)^{1/2}$ is the peak laser field ($n_0 = 1$). The cooling term contains elastic electron-neutral collisional cooling, electronic excitation of neutrals, cooling due to ionization, cooling due to radiation emitted by the electrons, and cooling due to electron transport. The cooling terms are neglected in the simulations.

The rate equations for the positive ion density, N_{ion}, and the negative ion density, $N_{O_2^-}$, are given by

$$\frac{\partial N_{ion}}{\partial\tau} = \nu_{col} N_e - \beta_e N_e N_{ion}, \tag{2.11a}$$

$$\frac{\partial N_{O_2^-}}{\partial\tau} = -\nu_{O_2^-} N_{O_2^-} + \eta_A N_e. \tag{2.11b}$$

The radial space charge electric field is given by $(1/\rho)\partial(\rho E_{sc,\rho})/\partial\rho = q(N_e - N_{ion})/\varepsilon_0$. Using the continuity equation, $\partial(N_e - N_{ion})/\partial\tau = -(1/\rho)\partial(\rho N_e V_\rho)/\partial\rho$, the radial component of the space field is given by

$$\partial E_{sc,\rho} / \partial \tau = -qN_e V_\rho / \varepsilon_0 . \tag{2.12}$$

In obtaining Eq. (2.12) the self-magnetic field has been neglected since the fluid velocities are << c.

In the absence of space charge and ionization, the maximum electron velocity from a micro-pulse due to the ponderomotive field in Eq. (2.4) is $(V_{pond} / c)_{\max} \approx I_0 \tau_L (r_e / \rho_0) \lambda_0^2 / (\pi mc^2)$, where $r_e = q^2 / (4\pi\varepsilon_0 mc^2)$ is the classical electron radius. For example, if $I_0 = 10^{16}\,\mathrm{W/m^2}$, $\rho_0 = 100\,\mu\mathrm{m}$, $\lambda_0 = 1\,\mu\mathrm{m}$ and $\tau_L = 100\,\mathrm{ps}$ the maximum electron velocity due to the ponderomotive force is $(V_{pond})_{\max} \approx 10^{-4} c$. The velocity in the presence of space charge fields is reduced.

Changes in air density due to thermal expansion are neglected in this model. The laser pulse train duration is $T \sim 10$ ns and the spot size is $\rho_0 \sim 100\ \mu$m. The air density depression due to the thermal blooming process occurs on a time scale of $\sim \rho_0 / \mathrm{v}_s$, where $\mathrm{v}_s \sim 300$ m/s is the sound speed in air. The density depression time is $\rho_0 / \mathrm{v}_s \sim 0.3\ \mu$s, which is much longer than the laser pulse train duration.

As the electron plasma density increases, it can reach a level where the attractive radial space charge force balances the repulsive radial ponderomotive force. When the increment in electron density caused by a single micro-pulse is large enough, the net radial force is substantially reduced. This balance occurs when the space charge field is equal to the ponderomotive field.

2.2.5. Plasma Defocusing

The electron plasma density is peaked on axis and, therefore, the refractive index is minimum on axis. The plasma filament, as well as diffraction, tend to defocus the micro-pulses in the LPT. To estimate the degree of defocusing, we assume that the radial variation of the electron density near the axis is given by $N_e(\rho) \approx N_{e0}(1-\rho^2/\rho_f^2)$, where $\rho < \rho_f$ is the characteristic radial size of the plasma filament. The plasma frequency, $\omega_{pe}(\rho) = \left(q^2 N_e(\rho)/(m\varepsilon_0)\right)^{1/2}$, is peaked on axis. The axial variation of the laser field amplitude spot size $R(z)$ is given by [5],

$$\frac{\partial^2 R}{\partial z^2} = \frac{4c^2}{\omega_0^2 R^3}\left(1 + \frac{\omega_{p0}^2}{4c^2\rho_f^2} R^4\right), \tag{2.13}$$

where $\omega_{p0} = \omega_{pe}(\rho = 0)$ is the plasma frequency on axis. The peak power P in the micro-pulses is far below the nonlinear focusing power in air, i.e., $P_{NL} = \lambda_0^2/(8\pi n_2) \sim 1\,\mathrm{GW}$, where $n_2 \approx 3\times10^{-23}\ \mathrm{m^2/W}$ is the Kerr refractive index for air at $\lambda_0 = 1\mu m$. Nonlinear focusing, therefore, has a negligible effect for our parameters. In addition, not shown in Eq. (2.13) is the relativistic focusing power [5,37], i.e., $P_{\mathrm{rel}} = 17.4(\omega_0/\omega_{p0})^2[\mathrm{GW}]$, which is also far greater than the micropulse power and, therefore, does not contribute to focusing of the pulses. Plasma defocusing dominates both diffractive defocusing and nonlinear focusing for the parameters considered. Under these conditions, Eq. (2.13) reduces to $\partial^2 R/\partial z^2 = R/L_{DF}^2$, and the spot size is $R(z) = R(0)\exp(z/L_{DF})$, where $L_{DF} = (\omega_0/\omega_{p0})\rho_f$, is the defocusing length.

The peak micro-pulse intensity I_0 is no longer constant in the LPT but varies as

$$I_0(z) = I_0(0)\exp(-2z/L_{DF}), \tag{2.14}$$

due to defocusing. When the electron density in the filament approaches air density ($2.7\times10^{25}\ \mathrm{m^{-3}}$), the effect of plasma defocusing becomes significant. For example, when the plasma electron density approaches air density, the defocusing length $L_{DF} \sim 10^{-5}$ m. Incoming micropulses will be able to maintain the high electron plasma density through ionization at the front of the filament, and the filament will continue to generate RF radiation at this elevated electron density.

2.2.6. RF Radiation

The RF intensity and power generated by the plasma electrons interacting with the ponderomotive and self-fields associated with the LPT and plasma filament are obtained in this section. The ponderomotive and self-electric fields are the dominant forces acting on the plasma electrons. Although the electrons are essentially stationary axially, the ionizing process propagates in the forward direction. The RF frequency spectrum can be controlled by varying the repetition rate and micropulse duration of the LPT. The configuration used in obtaining the RF Poynting flux is shown in Fig. 2.3.

The vector potential associated with the RF in the radiation zone is reduced to

$$\mathbf{A}(\mathbf{r},t) = \frac{\mu_0}{4\pi r}\int_{V'} \mathbf{J}\left(\mathbf{r}', t - r/c + \mathbf{r}'\cdot\hat{\mathbf{r}}/c\right) d^3\mathbf{r}', \tag{2.15}$$

where $\mathbf{J}$ is the radial current density and the integration is over the current density source, $d^3\mathbf{r}' = \rho' d\rho' d\varphi' dz'$. In the radiation zone the fields are $\mathbf{E}(\mathbf{r},t) = \hat{\mathbf{r}}\times(\hat{\mathbf{r}}\times\partial\mathbf{A}/\partial t)$ and

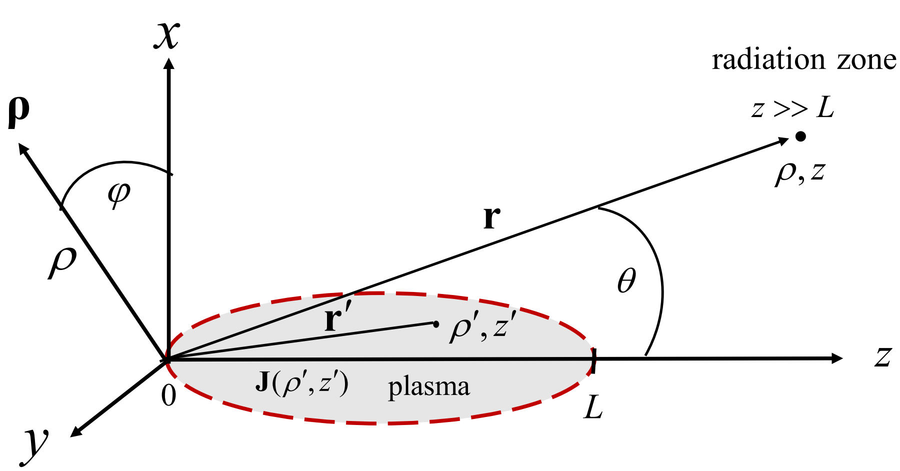

Figure 2.3. Configuration used in the evaluation of the RF intensity. The localized current and the charge density are confined to the region with the dotted red curve.

$\mathbf{B}(\mathbf{r},t) = -c^{-1}\hat{\mathbf{r}} \times \partial \mathbf{A} / \partial t$, where $\hat{\mathbf{r}}$ is the radial unit vector from the origin. The Poynting flux associated with the RF radiation is given by

$$\mathbf{S}(\mathbf{r},t) = (1/Z_0)\left|\hat{\mathbf{r}} \times \partial \mathbf{A}(\mathbf{r},t)/\partial t\right|^2 \hat{\mathbf{r}}, \tag{2.16}$$

where $Z_0 = \sqrt{\mu_0/\varepsilon_0}$. The angular distribution of the RF power is given by $dP(\mathbf{r},t)/d\Omega = r^2\mathbf{S}(\mathbf{r},t)\cdot\hat{\mathbf{r}}$, where $d\Omega = \sin\theta d\theta d\varphi$, and the total power radiated is $P = r^2\int \mathbf{S}(\mathbf{r},t)\cdot\hat{\mathbf{r}}d\Omega$. The vector potential in the radiation zone is

$$\mathbf{A}(\rho,z,t) = \frac{\mu_0}{2r}\int_0^L\int_0^\infty \mathbf{J}(\rho',z',t_R)\rho' d\rho' dz', \tag{2.17}$$

where the radial current density is $\mathbf{J} = qN_eV_\rho\hat{\boldsymbol{\rho}}$, $t_R = t - r/c + (\rho'\sin\theta + z'\cos\theta)/c$ is the retarded time, $\rho = r\sin\theta$ and $z = r\cos\theta$. The current density $J = qN_eV_\rho$ is obtained by numerically solving Eqs. (2.9a), (2.9b), (2.10), (2.11a), (2.11b), and (2.12).

The power radiated into the solid angle, $d\boldsymbol{\Omega} = d\Omega\hat{\mathbf{r}}$, where $d\Omega = \sin\theta d\theta d\varphi$, is $dP(\mathbf{r},t) = \mathbf{S}(\mathbf{r},t)\cdot d\mathbf{A} = r^2\mathbf{S}(\mathbf{r},t)\cdot d\boldsymbol{\Omega}$ and the total radiated power is $P = r^2\int \mathbf{S}(\mathbf{r},t)\cdot\hat{\mathbf{r}}d\Omega$. The angular power distribution is given by

$$dP(\mathbf{r},t)/d\Omega = r^2Z_0^{-1}\left|\hat{\mathbf{r}} \times \partial\mathbf{A}(\mathbf{r},t)/\partial t\right|^2 = r^2Z_0^{-1}\left|\mathbf{E}(\mathbf{r},t)\right|^2, \tag{2.18}$$

and is independent of r.

2.3. Simulation Results

In this section, Eqs. (2.9a), (2.9b), and (2.10) together with Eqs. (2.11a) and (2.11b) and Eq. (2.12) are solved numerically for the electron density and the radial space charge field. Equation (2.12) is used to evaluate the radial current density. The simulations assume that the collision frequency is significantly small so that the radial ponderomotive force dominates. At the end of the LPT, the radial space charge field balances the radial ponderomotive field, i.e., $E_{sc,\rho} \approx -E_{pond,\rho}$. This approximation is used to simplify the simulations at the tail end of the LPT. The radial plasma current density is used in Eq. (2.17) to obtain the vector potential associated with the RF radiation in the radiation zone. The Poynting flux and angular distribution of the radiation is obtained using Eqs. (2.16) and (2.18) respectively. These equations were solved using the various programs in Mathematica 12.0. The parameters used in the simulations are given in Table 2.1.

The energy depletion of the LPT can be neglected in the ionization process, since the energy needed to ionize the air is significantly less than the LPT energy.

Parameter	
Peak laser intensity, I_{peak}	4×10^{15} W/m^2
LPT energy	150 mJ
Average LPT power	7.4 MW
Pulse length, τ_L	100 ps
Pulse separation time, T_p	650 ps
Number of pulses, N_p	25
LPT duration, T_{LPT}	16 ns
Spot size, ρ_0	100 μm
Peak pulse power, P_0	60 MW
Initial electron density, N_0	10^3 m^{-3}

Table 2.1. Parameters used in simulations.

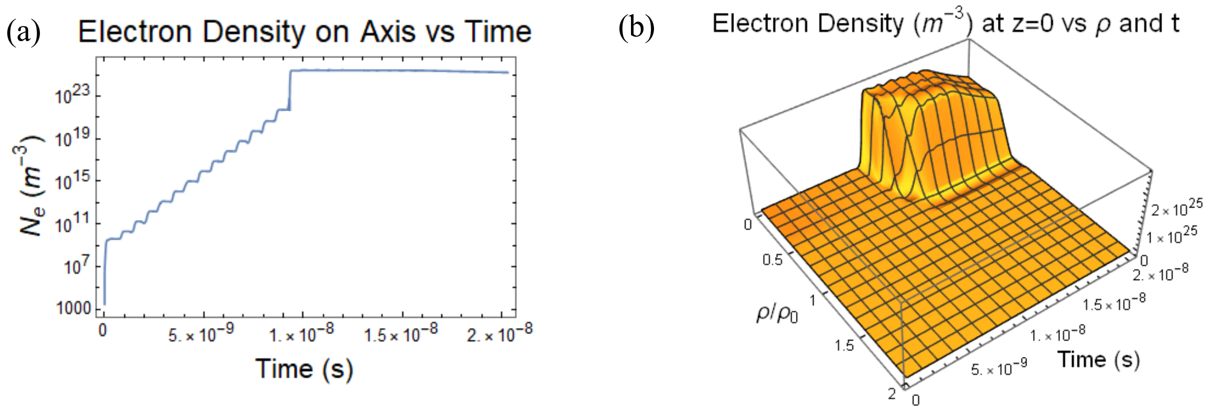

Figure 2.4. Electron density as a function of time in the laser pulse frame for a LPT with 25 micro pulses. Peak laser intensity is $I_0 = 4\times10^{15}$ W/m^2. (a) Logarithmic plot of the electron density along the axis of propagation. (b) Electron density as a function of time and radius, normalized to the spot size, from the axis of propagation.

2.3.1. Fluid Simulation Results

Here the LPT propagates into air and photo detaches the ambient negative ions to initiate collisional ionization. Figure 2.4(a) shows the electron density, N_e, on axis as a function of time. Figure 2.4(b) shows the electron density as a function of time and radius. The maximum electron density reached by the plasma filament is $\sim 10^{25}\,\mathrm{m}^{-3}$. The electron density is localized on axis and

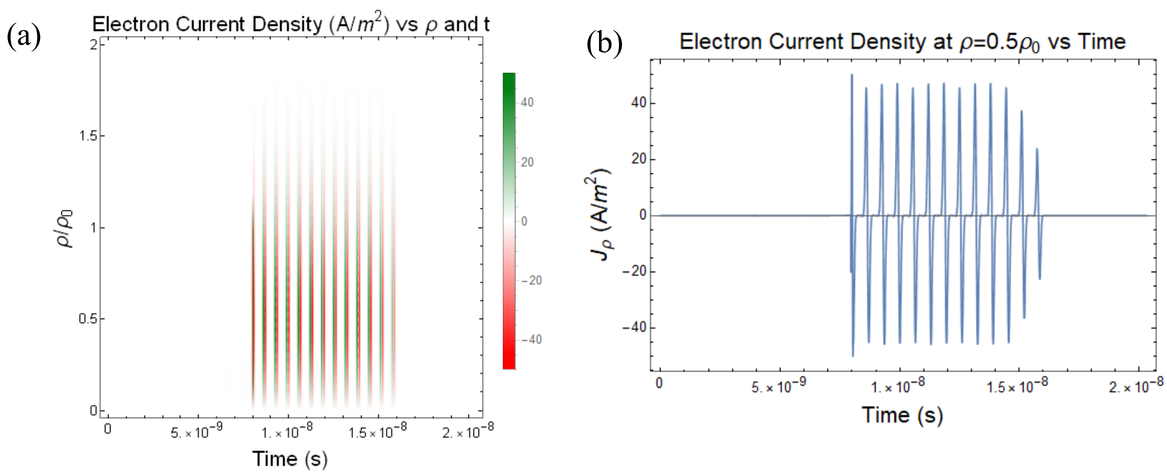

Figure 2.5. Radial electron current density for a LPT of 25 micro-pulses having a peak intensity of $I_0 = 4\times10^{15}$ W/m^2. (a) Radial current density as a function of radius, normalized to the spot size, and time in the laser pulse frame. (b) Radial electron current density as a function of time in the laser pulse frame at $\rho = 0.5\rho_0$.

increases toward the end of the LPT. The space charge electric field is less than the ponderomotive field at the beginning of the LPT. Therefore, there is little restoring force on the electrons. Once the space charge electric field becomes comparable to the ponderomotive field, the electron fluid velocity, and the current density, reach a maximum. Figure 2.5(a) shows the electron current density as a function of radius and time. The current density is highest near the end of the LPT, where the electron density is high and the space charge field is comparable to the ponderomotive field. Figure 2.5(b) shows the electron current density at $\rho = 0.5\rho_0$ as a function of time.

2.3.2. RF Radiation

Figure 2.6 shows a comparison of our simulated RF spectrum with an experimental spectrum [2,20,24] employing very similar LPT parameters. The experiment employed a LPT consisting of >30 micro-pulses with a micro-pulse separation of $T_p = 650$ ps. The focused LPT, having a total energy of $E_{LPT} = 510$ mJ, generated a plasma filament in air. The peak intensity of the micro-pulses is estimated to be $I_{peak} \approx 5\times10^{15}$ W/m^2. A loop antenna was used to detect the

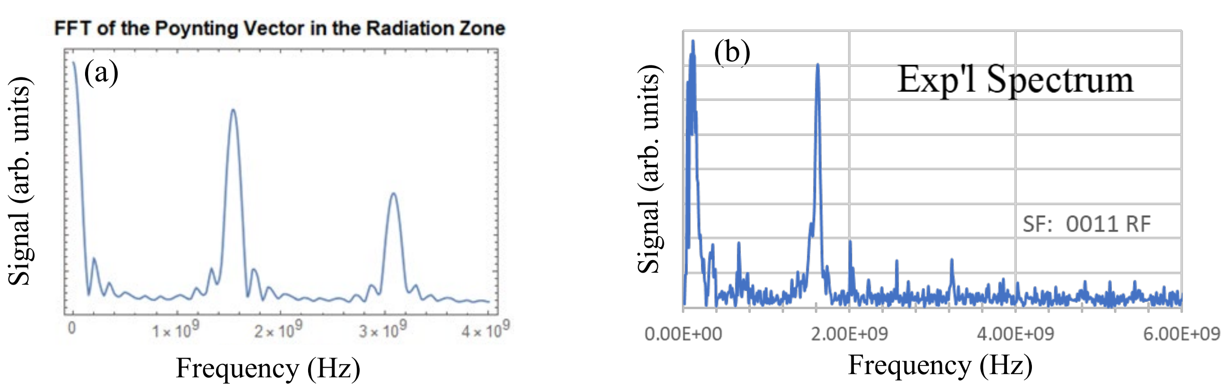

Figure 2.6. The calculated and experimental spectra of the RF in arb. units. (a) The calculated spectrum from a LPT with 40 micro pulses and (b) the experimentally measured spectrum. The fundamental peak is at 1.6 GHz in both spectra. Note that the harmonics are not shown in the experimental spectrum since the receiving antenna was tuned to only a narrow range of frequencies. The harmonics, however, have been measured experimentally [2].

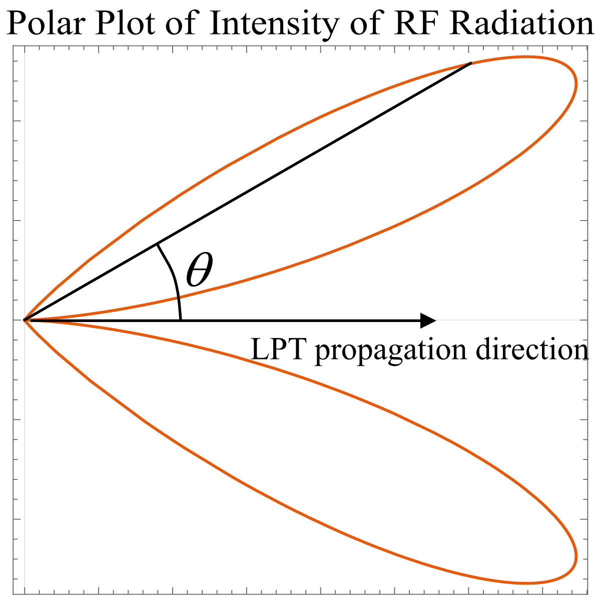

Figure 2.7. Polar plot of the angular distribution of the intensity of the RF radiation. The radiation is azimuthally symmetric and directed at an angle θ from the direction of propagation of the LPT.

RF signal generated by the plasma filament [2,20,24]. Figure 2.6(a) shows the spectrum by taking a Fourier transform of Eq. (2.16). The peak intensity of the total calculated RF signal, approximately half a meter from the filament, is $\sim 10^{-10}$ W/m^2 ($E_{rf} \sim 10^{-4}$ V/m). Figure 2.6(b) shows the experimental spectrum. The antenna in the experiment is tuned to receive a narrow range of frequencies. Therefore, harmonics that are present in the calculated spectrum are not shown in the experimental data.

The angular dependence of the RF radiation is shown in Fig. 2.7. The radiation due to a dominant radial electron current is in a cone directed forward at approximately 30°. The radiation is azimuthally symmetric.

2.4. Dominant Longitudinal Force Case

In this subsection I will present the results for the case when the longitudinal ponderomotive force dominates the radial ponderomotive force. The longitudinal force is dominant over the radial force when the ratio $2c/\Gamma\rho_0 << 1$. For $\Gamma \sim 10^{13}$ s^{-1} and $\rho_0 > 100$ μm, this is the case. The ionization process is the same as the previous simulations, and electron diffusion is still negligible in our parameter regime.

The longitudinal space charge field needs is

$$\partial E_{sc,z} / \partial \tau = -qN_eV_z / \varepsilon_0 . \tag{2.19}$$

The electric field is obtained in the same manner as in Section 2.2.4. When the plasma filament approaches air density, the space charge field balances the ponderomotive field as before, i.e., $E_{sc,z} \approx -E_{pond,z}$. Therefore, the longitudinal current is $J_z = \varepsilon_0 \partial E_{pond,z} / \partial \tau$. This expression for the current density can be used in Eq. (2.17) to calculate the RF radiation.

The radiation will be the same frequency as before, however, the magnitude and direction of the radiation will be different. The vector potential will be increased by the ratio $\Gamma\rho_0 / 2c$. Because the current is only in the longitudinal direction, it will radiate like a dipole. The radiation is in the direction transverse to the LPT propagation direction.

2.5. Experimental Results

Experiments have been performed by Dr. Vladimir Markov at Advanced Systems and Technologies, Inc., which demonstrate the generation of RF radiation using a LPT [2,24]. In these experiments, the LPT has similar parameters to those used in the simulations. The LPT produces a plasma spark and drives electron currents, which generate RF radiation. The strength and directionality of the RF signal was measured. The mechanism was also used to demonstrate jamming of a GPS antenna.

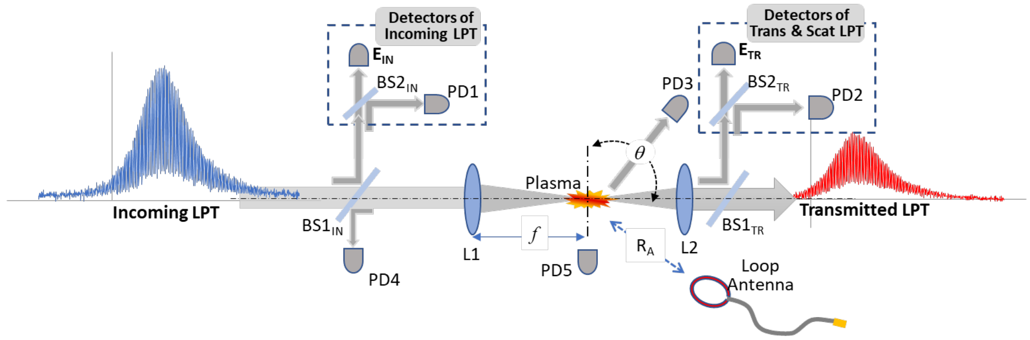

Figure 2.8. Schematic of the plasma generation and analysis setup. The transmitted LPT profile (red) has a lower amplitude compared to the input LPT profile (blue) to indicate the significant attenuation caused by the ignited plasma at certain conditions.

2.5.1. Experimental Setup

Figure 2.8 illustrates the schematic of the experimental setup used to study the LPT-generated plasma in air. The beamsplitters $BS1_{IN}$ and $BS2_{IN}$ sample the incoming LPT beam to measure both its energy, with the energy meter E_{IN}, and temporal profile, with the photodiode PD1. The incoming LPT beam is then focused by the lens L1 of focal length f = 38 mm into a spot in the focal plane where the laser-induced plasma is generated. This occurs once the intensity of the laser beam exceeds the threshold for laser breakdown of air. The laser beam transmitted through the focal spot is incident onto lens L2, and is then split into two parts by the sampling beamsplitter $BS1_{TR}$. The transmitted part of the laser beam can be used for detection and analysis of its spatial spatter. The reflected light is received by detectors of the transmitted LPT module, where it is split into two parts to measure both the transmitted pulse energy, with energy meter E_{TR}, and its temporal profile, using the photodiode PD2. Photodiodes PD3 and PD4 are used to detect the dynamics of the side- and back-scattered radiation. The angular distribution of the side-scattered laser radiation detected by the photodiode PD3 can be measured by changing its angular position with the hemispherical angle -80º > θ > 10º. Photodiode PD5 is used to detect a timeline of plasma luminescence.

The loop antenna, placed at a distance $R_A \leq 20$ cm from the plasma spark, was used to detect and characterize the plasma-generated RF signal. The antenna can be rotated azimuthally about the LPT propagation axis. To prevent contamination of the RF data by secondary reflection, the number of support components within the measurement box was minimized and they were made of plastic. The quality of the RF signal was verified and validated by comparing its characteristics to a non-laser generated RF signal of controlled amplitude and length. Figure 2.9 shows a picture of the experimental setup on the optical table.

2.5.2. LPT and measured RF Radiation

LPTs with energy levels exceeding 100 mJ induce visible light sparks. These light sparks remain for durations on the order of ~100 ns. The plasma recombination time is ~10 ns. In these

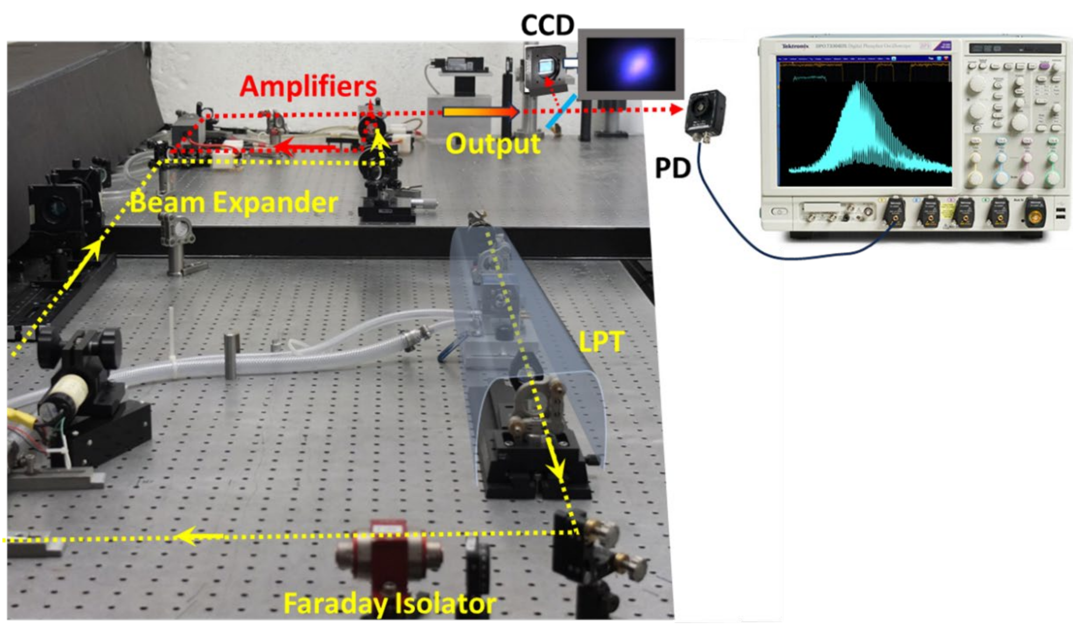

Figure 2.9. Picture of the experimental setup. The image shows the optical components that generate the LPT and the devices that make the measurements.

experiments, detection of the RF signal was performed by using the RFEAH-25 H-Loop magnetic antenna (see the setup in Fig. 2.8) designed for near-field measurements. The digitized representation of the RF signal and its Fourier spectrum are shown with red trace in Figs. 2.10(a) and 2.10(b), respectively. Blue graphs demonstrate the underlining LPT temporal profile and its discrete Fourier transform spectrum. The LPT profile carries an amplitude modulation at a frequency of 1.25 GHz that translates into a signature amplitude peak of the same frequency for the RF signal. Spectral data for the LPT and RF signals shown in Fig. 2.10 is in a good agreement with the results of the analysis of the laser induced plasma performed in the laser pulse train regime, published in previous work [1,24,38,39].

Other broadband spikes are present in the RF spectrum. Likely, all these spikes are the signals from other external RF radiation sources that are not related to our experiment. In particular, the spikes at about 2.1 GHz may come from the WiFi network. We conclude that the detected RF radiation is driven solely by the LPT micro-pulses. The RF strength reaches a maximum when the filament density is sufficiently high. The RF strength remains high until the LPT amplitude begins to decrease.

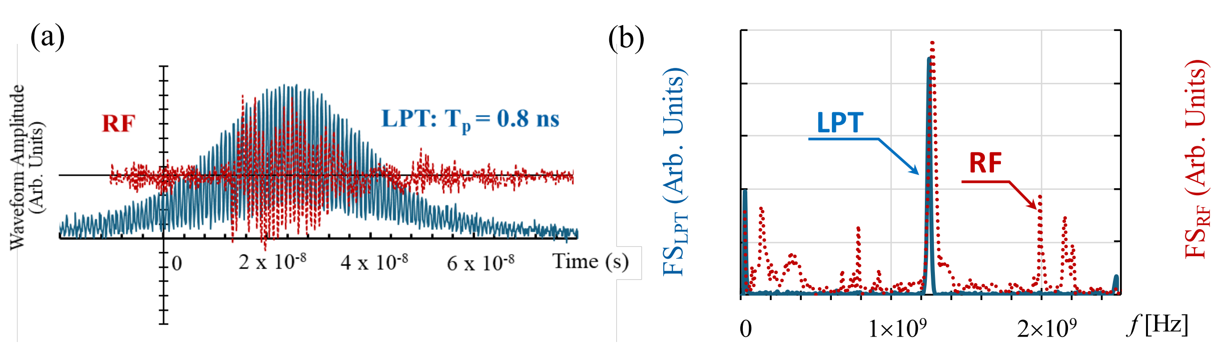

Figure 2.10. (a) The digitized trace of the LPT (blue) and RF (red) signals; (b) the overlapped Fourier spectra FS_{LPT} and FS_{RF} of the LPT and RF signals shown in (a). The graph (a) is in arb. units and seconds; (b) has arbitrary units for amplitude and Hz for frequency scale.

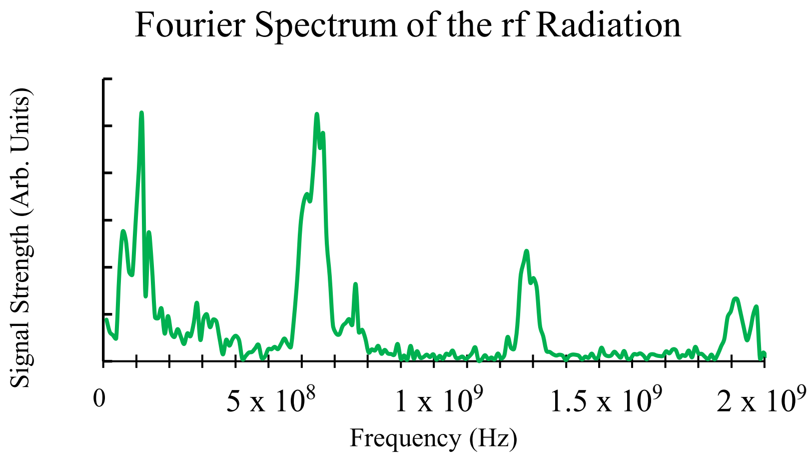

Figure 2.11. Fourier Spectrum of the RF signal. The LPT had a laser pulse separation time of T_p = 1.5 ns, which gives a fundamental RF frequency of 650 MHz. The harmonics are also visible at 1.3 GHz and 1.95 GHz.

Figure 2.11 shows the measured harmonics of the RF signal. The LPT has a pulse separation T_p = 1.5 ns. This pulse separation corresponds to a fundamental frequency of ~650 MHz. The harmonics can be seen at 1.3 GHz and 1.95 GHz. Figure 2.12 shows the tunability

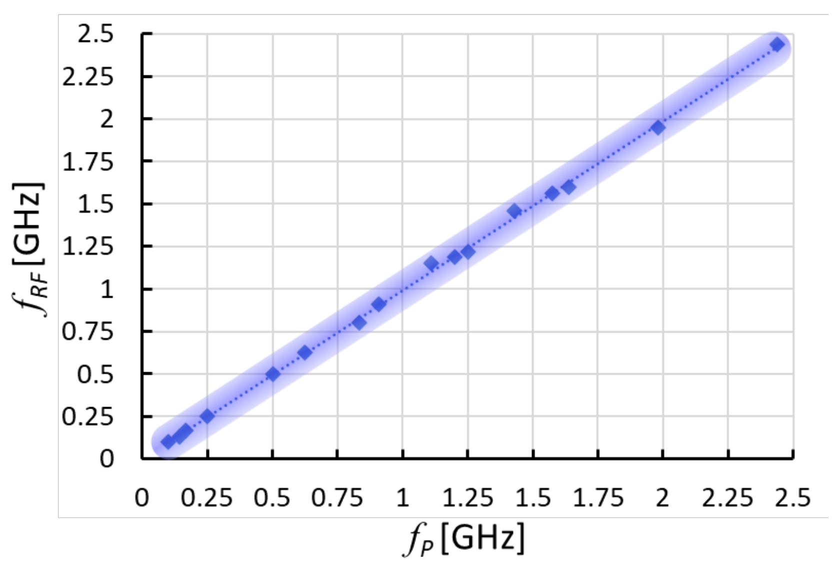

Figure 2.12. Plot of the micro-pulse frequency of the LPT and the produced RF frequency, showing the range of tunability of the LPT and the RF. The RF frequency is the same as the micro-pulse frequency for all values of f_p.

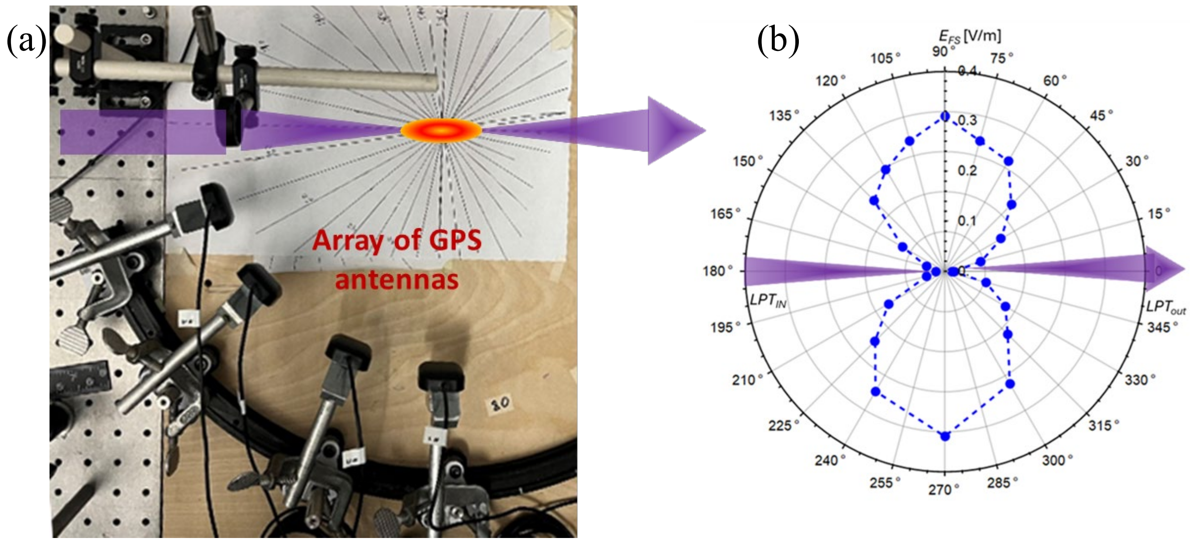

Figure 2.13. (a) The experimental setup of the measurement. GPS antennas were placed in an array around the plasma filament and the strength of the RF signal was measured. (b) Polar data of the directionality of the RF radiation. The plot shows that the RF radiation is peaked in the direction that is transverse to the direction of propagation of the LPT. The peak field amplitude of the RF signal measured 60 cm from the filament is 0.3 V/m, which is 5 orders of magnitude above the GPS signal strength at ground level.

of the LPT, and, therefore, the RF frequency produced. The linear relationship of the micro-pulse repetition frequency to the RF frequency can be seen.

The directionality of the RF radiation is shown in Fig. 2.13. The radiation is directed 90° from the direction of propagation of the LPT. The directionality indicates that the currents generating the RF radiation are in the longitudinal direction. This indicates that the experimental parameters are different from the simulation parameters. If radial oscillations were dominant, then the RF would be directed forward in a cone shape around 30° from the direction of propagation of the LPT. This suggests that the spot size of the LPT is larger than 100 μm at the focus, or that the electron collision frequency is higher than what was estimated. The peak electric field amplitude of the RF signal at 60 cm from the plasma filament is 0.3 V/m. The GPS signal strength at ground level is ~5 μV/m.

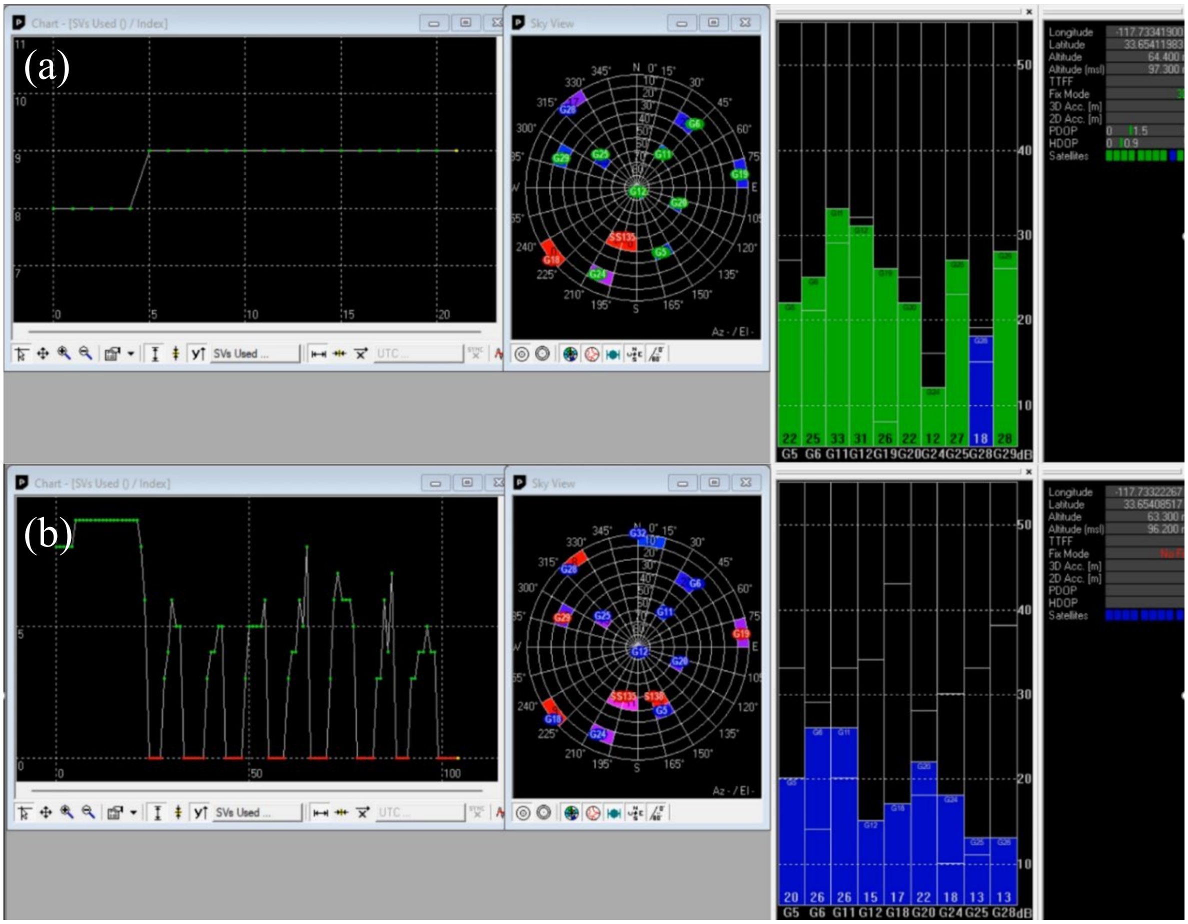

Figure 2.14. Depiction of GPS jamming due to the RF radiation. The total signal strength is shown in the left graphs. The GPS satellites and their connection strength are shown in the middle and right charts. (a) GPS signal before the jamming starts, showing a strong connection. (b) GPS signal during operation of the LPT, showing successful jamming.

Jamming of a GPS antenna was demonstrated experimentally by the LPT. By operating the laser at a 10 Hz repetition rate, the generated RF signal was able to disrupt communications between a GPS antenna and the GPS satellites. Figure 2.14 shows the measurment of the jamming. The graphs on the left of the figure show the total GPS signal strength as a function of time. The charts in the middle show the GPS satellites. The charts on the right show the signal strength from each of the satellites. The top row of the figure, Fig. 2.14(a), shows the GPS signal before the LPT begins operating. The bottom row of the figure, Fig. 2.14(b) shows the signal while the LPT is operating. This shows succesful jamming of the GPS signal.

2.6. Discussion

In this chapter, I proposed, analyzed, and numerically simulated a mechanism for generating RF radiation in air by using low intensity laser pulse trains (LPT). In the model, the LPT propagates in air and photo detaches the ambient negative molecular ions, which are present due to background (ambient) radiation. The photo detached electrons provide the seed electrons for collisional ionization to take place and become the dominant ionization process. The build up of electrons form a plasma filament. The ionized plasma electrons are acted on by the ponderomotive forces (radial and axial) associated with the LPT. The formation of the plasma filament tends to defocus the trailing pulses in the LPT which can limit the length of the plasma filament. The plasma oscillations provide a driving current density which generates RF radiation. The duration of the RF signal is determined by the duration of the LPT. The peak intensity of the RF signal, 60 cm from the filament, is measured to be $\sim 10^{-4}\ \mathrm{W/m^2}$ ($E_{rf} \sim 10^{-1}\ \mathrm{V/m}$). The frequency spectrum of the RF radiation is determined by the harmonics of the micropulse separation time and duration. The frequency spectrum can be controlled by varying the pulse repetition rate and duration of the micro-pulses. For a particular set of LPT parameters, our numerically simulated frequency spectrum is in general agreement with the experimental spectrum. The experiment demonstrated effective jamming of a GPS antenna.

Chapter 3: Stability and Propagation of Laser Pulses in the Atmosphere

Propagation of laser pulses over extended distances in the atmosphere has numerous applications [1,40-43]. The atmosphere is dispersive, nonlinear, and turbulent, thereby resulting in distortion of the laser pulse. Atmospheric turbulence can lead to transverse spreading and centroid wandering of the pulse's spot size [44-48] as well as fluctuations in the laser pulse arrival time and temporal pulse broadening [49-52]. Turbulence can also cause pulse breakup to occur during propagation, even under weak turbulence conditions [53]. For many applications, the laser intensity is limited by the requirement to avoid ionization. However, nonlinearities associated with neutral air molecules can lead to instabilities [37,54-56]. Neutral air molecules can produce self-phase modulation which is responsible for a hybrid filamentation-modulation instability. This instability can break up the laser pulse transversely and longitudinally in air [5,57-63] and in plasmas [64-66]. The transverse and longitudinal instabilities are generally treated individually. However, they are inherently coupled and hence we treat them together.

In this chapter I present analysis and simulations of the propagation and stability of laser pulses in air over extended distances in the vertical direction. In the stability model, the equilibrium state of the laser pulse is dynamic so that the spot size, pulse duration, wavefront curvature, phase, chirp parameter, and pulse length evolve along the propagation path. The laser pulse parameters are tailored in such a way that the maximum transverse and longitudinal focusing occur at nearly the same remote location, thereby resulting in a significant intensity enhancement. Our propagation model includes turbulence effects and the simulations are performed for long propagation distances that are typically computationally challenging [67-70]. The dispersion relation describing the hybrid filamentation-modulation instability is obtained by perturbing the dynamic equilibrium of the laser pulse. The instability is due to the coupling between the transverse filamentation and the longitudinal modulation instabilities. An analytic expression is given in the case where the spot size and pulse duration are constant, i.e., independent of z. In the general case, where the spot size and pulse duration evolve, the simulations indicate that the laser pulse breaks up transversely and longitudinally. Our model allows for laser pulse propagation simulations over extended distances. The model is valid in the paraxial approximation, where the pulse envelope changes slowly with respect to the wavelength. Using full-scale wave-optics simulations, which use phase screens to model turbulence, to study these instabilities over extended distances can be computationally challenging.

3.1. Propagation Model

A propagation equation is derived which describes the dynamics of a laser pulse propagating in the atmosphere. It describes the evolution of the laser pulse amplitude and phase in the paraxial limit, and includes the effects of linear and nonlinear dispersion. The variation of air density and level of turbulence along the propagation path is taken into account. This section follows a derivation similar to that in [5,55]. The wave equation is given by

$$\left(\nabla_\perp^2 + \frac{\partial^2}{\partial z^2} - \frac{1}{c^2}\frac{\partial^2}{\partial t^2}\right)\mathbf{E}(\mathbf{r}_\perp, z, t) = \mu_0 \frac{\partial^2 \mathbf{P}(\mathbf{r}_\perp, z, t)}{\partial t^2}, \tag{3.1}$$

where the polarization field $\mathbf{P} = \mathbf{P}_L + \mathbf{P}_{NL}$ consists of a linear $\mathbf{P}_L$ and nonlinear $\mathbf{P}_{NL}$ contribution. The laser electric field is given by

$$\mathbf{E}(\mathbf{r}_\perp, z, t) = (1/2) A(\mathbf{r}_\perp, z, t) \exp(i\psi(z,t))\hat{\mathbf{e}}_\perp + c.c., \tag{3.2}$$

where $\psi(z,t) = k_0 z - \omega_0 t$ is the carrier phase, k_0 is the wavenumber, ω_0 is the frequency, A is the complex amplitude, which is assumed to be slowly varying in z and t compared to the carrier phase, $\hat{\mathbf{e}}_\perp$ is a unit vector in the transverse direction, $\nabla_\perp^2$ is the transverse Laplacian operator, and *c.c.*

denotes the complex conjugate. The laser intensity is given by $I(\mathbf{r},t) = n_L \left|A\right|^2 / (2Z_0)$, where n_L is the linear index of refraction and $Z_0 = \sqrt{\mu_0 / \varepsilon_0} = 377\ \Omega$.

3.1.1. Polarization Fields

The linear polarization field is given by

$$\mathbf{P}_L(\mathbf{r}_\perp, z, t) = (1/2) P_L(\mathbf{r}_\perp, z, t) \exp(i\psi(z,t)) \hat{\mathbf{e}}_\perp + c.c.. \tag{3.3}$$

And the linear source term is

$$\mu_0 \frac{\partial^2 \mathbf{P}_L}{\partial t^2} = (1/2) S_L(\mathbf{r}_\perp, z, t) \exp(i\psi(z,t)) \hat{\mathbf{e}}_\perp + c.c., \tag{3.4}$$

where $S_L(\mathbf{r}_\perp, z, t) = \sum_{s=0}^{\infty} Q_s(z,\omega_0) \partial^s A / \partial t^s$, $Q_s(z,\omega_0) = c^{-2} \dfrac{(i)^s}{s!} \dfrac{\partial^s(\omega_0^2(1 - n_L^2(z,\omega_0)))}{\partial \omega_0^s}$, $s = 0, 1, 2 \ldots$.

The sum over s comes from an expansion of the electric field amplitude about t = 0. Defining $\beta_s(z,\omega_0) = c^{-1}\partial^s(\omega_0 n_L(z,\omega_0)) / \partial\omega_0{}^s$, we note that $Q_0(z,\omega_0) = (\omega_0^2 / c^2)(1 - n_L^2(z,\omega_0))$, $Q_1(z,\omega_0) = 2ic^{-2}\omega_0\left(1 - cn_L(z,\omega_0)\beta_1(z,\omega_0)\right)$ and $Q_2(z,\omega_0) = -c^{-2}\left(1 - c^2\left(\beta_1^2(z,\omega_0) + \beta_0(z,\omega_0)\beta_2(z,\omega_0)\right)\right)$. The group velocity is $\mathrm{v}_g = c\left(\partial(\omega_0 n_L(\omega_0)) / \partial\omega_0\right)^{-1} = 1/\beta_1$. Typical values for the group velocity dispersion parameters in air at approximately $\lambda = 1\ \mu\mathrm{m}$ are $\beta_2 \approx 20\ \mathrm{fs}^2/\mathrm{m}$ and $\beta_3 \approx 10\ \mathrm{fs}^3/\mathrm{m}$ [71]. It is necessary to include the third order dispersion Q_3 for pulse durations < 30 fs in the absence of a chirp. For the parameters used here the higher order dispersion term Q_3 can be neglected. A detailed derivation of the dispersion coefficients is presented in Appendix B.

The nonlinear polarization field is given by

$$\mathbf{P}_{NL}(\mathbf{r}_\perp, z, t) = (1/2) P_{NL}(\mathbf{r}_\perp, z, t) \exp(i\psi(z,t)) \hat{\mathbf{e}}_\perp + c.c.. \tag{3.5}$$

For an isotropic medium, the nonlinear polarization field amplitude is $P_{NL} = (3/4)\varepsilon_0 \chi_3 |A|^2 A$, and χ_3 is the third order scalar susceptibility. The nonlinear source term is

$$\mu_0 \frac{\partial^2 \mathbf{P}_{NL}}{\partial t^2} = (1/2) S_{NL}(\mathbf{r}_\perp, z, t) \exp(i\psi(z,t)) \hat{\mathbf{e}}_\perp + c.c., \tag{3.6}$$

where $S_{NL} = -(3/8)(\omega_0^2 / c^2)\chi_3 \left(1 + 2i(1/\omega_0)\partial/\partial t\right)|A|^2 A$.

3.1.2. Propagation Equation

Substituting Eqs. (3.2), (3.4), and (3.6) into Eq. (3.1) yields the reduced wave equation, in the paraxial limit, for the laser field amplitude,

$$\begin{aligned} &\left(\nabla_\perp^2 - k_0^2 + \frac{\omega_0^2}{c^2} + 2ik_0 \frac{\partial}{\partial z} + 2i\frac{\omega_0}{c^2}\frac{\partial}{\partial t} + \frac{\partial^2}{\partial z^2} - \frac{1}{c^2}\frac{\partial^2}{\partial t^2} - \sum_{s=0}^{\infty} Q_s(z,\omega_0)\frac{\partial^s}{\partial t^s}\right) A = \\ &\qquad - 2k_0 \gamma_{NL}\left(1 + i\frac{2}{\omega_0}\frac{\partial}{\partial t}\right)|A|^2 A \end{aligned}, \tag{3.7}$$

where $\gamma_{NL} = (3/16)k_0 \chi_3$. In terms of the nonlinear (Kerr) refractive index n_2, defined by $n = n_L + n_2 I$, $\gamma_{NL} = (1/2)k_0 n_2 / Z_0$, where $\chi_3 = (8/3)n_2 / Z_0$. Keeping linear dispersion terms up to order $Q_2(z,\omega_0)$, Eq. (3.7) becomes

$$\begin{aligned} &\left(\nabla_\perp^2 - k_0 \Delta k(z) + 2ik_0 \frac{\partial}{\partial z} + \frac{\partial^2}{\partial z^2} + i\frac{2k_0}{\mathrm{v}_g(z)}\frac{\partial}{\partial t} - \left(1 + c^2 Q_2(z,\omega_0)\right)\frac{1}{c^2}\frac{\partial^2}{\partial t^2}\right) A = \\ &\qquad - 2k_0 \gamma_{NL}\left(1 + i\frac{2}{\omega_0}\frac{\partial}{\partial t}\right)|A|^2 A \end{aligned}, \tag{3.8}$$

where $\Delta k(z) = (k_0^2 - n_L^2 \omega_0^2 / c^2)/k_0$, $\mathrm{v}_g(z) = k_0 / (\beta_0(z,\omega_0)\beta_1(z,\omega_0))$ is the group velocity, $\beta_0(z,\omega_0) = n_L \omega_0 / c$, and $\beta_1(z,\omega_0) = (n_L / c)(1 + \omega_0 \partial \ln(n_L)/\partial\omega_0)$.

Laser beams generally undergo focusing when the laser power exceeds a nonlinear focusing power P_K given by

$$P_K = \frac{\pi c}{4 Z_0 \omega_0 \gamma_{NL}} = \frac{4\pi}{3 Z_0} \frac{c^2}{n_L \omega_0^2} \frac{1}{\chi_3} = \frac{\lambda_0^2}{8\pi} \frac{n_L}{n_2}. \tag{3.9}$$

The quantity $2\gamma_{NL} |A|^2$ in Eq. (3.8) is proportional to the intensity and is the driving term for the instabilities. In terms of the laser power $P_{laser} = I_{laser} \pi R^2(z)/2$, the driving term is $2\gamma_{NL} |A|^2 = 2k_0 n_2 I_{laser} = 4k_0 n_2 P_{laser} / (\pi R^2(z)) = I_{laser} \lambda_0 / (2P_K)$, where $I_{laser} = |A|^2 / 2Z_0$ is the peak intensity and $R(z)$ is the spot size. In terms of the laser power and nonlinear power, $k_0 \gamma_{NL} |A|^2 R^2(z) = P_{laser} / P_K$. The nonlinear focusing power for air at $\lambda_0 = 1\ \mu\text{m}$ is $P_K \sim 3\,\text{GW}$ [5,37], where, $n_2 = 3\times 10^{-23}\,\text{m}^2/\text{W}$ and $I_{laser} = 10^{16}\,\text{W/m}^2$. In the remainder of the section $n_L \approx 1$. The various defined quantities take on the following values, $\beta_0 = \omega_0 / c$, $\beta_1 \approx 1/c$, $\Delta k = 0$, $\text{v}_g = c$, and $k_0 = \omega_0 / c$.

It is convenient to perform a change of independent variables from z and t to $\eta = z$ and $\tau = t - z/\text{v}_g$. Using $\partial/\partial t = \partial/\partial\tau$, $\partial/\partial z = \partial/\partial\eta - \text{v}_g^{-1}\partial/\partial\tau$, and $\partial^2/\partial z^2 = \partial^2/\partial\eta^2 - 2\text{v}_g^{-1}\partial^2/\partial\eta\partial\tau + \text{v}_g^{-2}\partial^2/\partial\tau^2$, the wave equation in Eq. (3.8) becomes

$$\left(\nabla_\perp^2 + 2ik_0 \frac{\partial}{\partial\eta} - k_0 \beta_{GVD}(\eta) \frac{\partial^2}{\partial\tau^2} - \frac{2}{\text{v}_g} \frac{\partial^2}{\partial\eta\,\partial\tau} \right) A = -2k_0 \gamma_{NL} |A|^2 A, \tag{3.10}$$

where the term $\partial^2/\partial\eta^2$ has been neglected compared to $k_0 \partial/\partial\eta$, as has the $\partial/\partial\tau$ term on the right-hand side of Eq. (3.8). These approximations are valid in the paraxial limit. The group velocity dispersion parameter is $\beta_{GVD}(\eta) = ((\omega_0/c) n_L(\eta) \beta_2(\eta) + \beta_1^2(\eta) - 1/c^2)/k_0$. Although $n_L \approx 1$, we have a finite group velocity dispersion parameter $\beta_{GVD} \approx \beta_2$. For example, at ground level for $\lambda_0 = 0.85\ \mu\text{m}$, $\beta_{GVD} = 2.1\times 10^{-29}\ \text{s}^2/\text{m}$.

3.2. Dynamic Equilibrium

A set of coupled nonlinear envelope equations is derived for the laser pulse spot size, pulse duration, phase, and amplitude. It is customary to use the symbol z for the distance in the direction of propagation instead of η.

The axially symmetric equilibrium laser pulse amplitude $A_{eq}(r,z,\tau)$ shown in Fig. 3.1, is represented as [5],

$$A_{eq}(r,z,\tau) = E(z)\exp\left(i\varphi(z)\right)\exp\left(-(1+i\alpha(z))r^2 / R^2(z)\right)\exp\left(-(1+i\beta(z))\tau^2 / T^2(z)\right), \tag{3.11}$$

where $E(z)$ is the amplitude, $\varphi(z)$ denotes the phase, $\alpha(z)$ denotes phase wavefront curvature, $\beta(z)$ is the chirp parameter, $R(z)$ is the spot size, $T(z)$ is the laser pulse length, and the quantities E, φ, α, and β are real.

By inserting Eq. (3.11) into Eq. (3.10) and expanding the Gaussian terms to second order in the radial and temporal dimensions, Eq. (3.11) reduces to

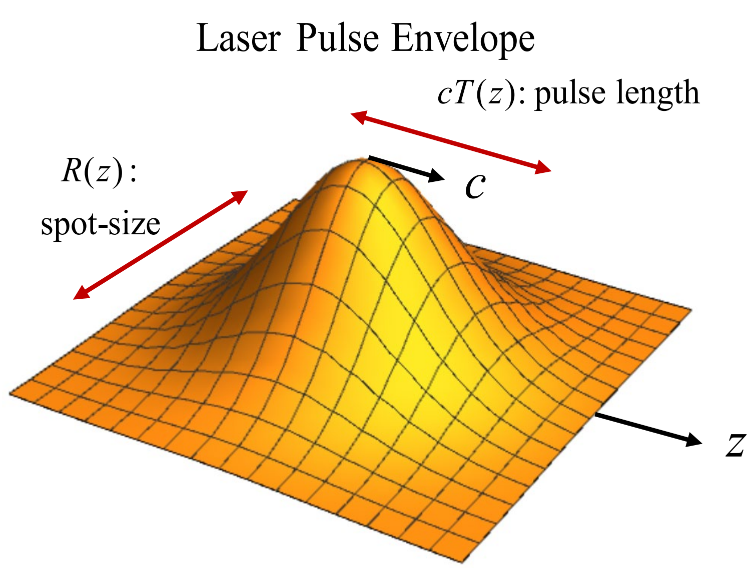

Figure 3.1. Schematic of the laser pulse indicating the spot size and pulse duration. The pulse propagates along the z-axis. The spot size and pulse duration are denoted by $R(z)$ and $T(z)$.

$$\left(\nabla_\perp^2 + 2ik_0\frac{\partial}{\partial z} - k_0\beta_{GVD}(z)\frac{\partial^2}{\partial\tau^2}\right)A_{eq} \approx -2k_0\gamma_{NL}E^2(z)\left(1-2\frac{r^2}{R^2(z)}-2\frac{\tau^2}{T^2(z)}\right)A_{eq}, \quad (3.12)$$

where the quantities E, φ, α, and β satisfy the following equations,

$$\frac{2}{k_0R^2}+\frac{\partial\varphi}{\partial z}-\frac{\beta_{GVD}}{T^2}=\gamma_{NL}E^2, \quad (3.13a)$$

$$-2\frac{\alpha}{k_0R^2}+\frac{1}{E}\frac{\partial E}{\partial z}+\beta_{GVD}\frac{\beta}{T^2}=0, \quad (3.13b)$$

$$\frac{(1-\alpha^2)}{k_0R^2}+\frac{1}{2}\frac{\partial\alpha}{\partial z}-\alpha\frac{1}{R}\frac{\partial R}{\partial z}=\gamma_{NL}E^2 \ , \quad (3.13c)$$

$$R\frac{\partial R}{\partial z}=-\frac{2}{k_0}\alpha, \quad (3.13d)$$

$$\frac{1}{2}\frac{\partial\beta}{\partial z}-\frac{\beta}{T}\frac{\partial T}{\partial z}-(1-\beta^2)\frac{\beta_{GVD}}{T^2}=\gamma_{NL}E^2, \quad (3.13e)$$

$$\frac{\partial T}{\partial z}=2\frac{\beta_{GVD}\beta}{T}. \quad (3.13f)$$

Equation (3.12) defines the dynamic equilibrium associated with the field A_{eq} and is valid for values of r and τ which are not significantly greater than the spot size or pulse duration. The term containing the cross-derivative in Eq. (3.10) is neglected since $\mathrm{v}_g^{-1}\partial/\partial\tau << k_0$. From Eqs. (3.13b), (3.13d), and (3.13f) we find the relationship $E^2(z)R^2(z)T(z)=E_0^2R_0^2T_0$, which is a result of energy conservation. As there is no ionization taking place, the energy of the system is in the laser electromagnetic field and the kinetic energy of the bound electrons. The kinetic energy imparted to the bound electrons from the laser is negligible compared to the laser pulse energy. As filamentation occurs, the energy in the pulse is redistributed spatially, however, the total energy remains constant. The conservation of energy has been verified in the numerical simulations.

The instantaneous frequency of the laser pulse is given by $\omega(\mathbf{r}_\perp, z, \tau) = -\partial\Psi(\mathbf{r}_\perp, z, \tau)/\partial\tau$, where Ψ is the phase of the electric field, $E(\mathbf{r}_\perp, z, t) = (1/2)A_{eq}(r, z, \tau)\exp(i(k_0 z - \omega_0 t)) + c.c.$, and $A_{eq}(r, z, \tau)$ is given by Eq. (3.11). The instantaneous frequency is

$$\omega(\mathbf{r}_\perp, z, \tau) = \omega_0 + 2\beta(z)\tau / T^2(z) = \omega_0 + (\tau / \beta_{GVD})\partial \ln(T(z)) / \partial z, \tag{3.14}$$

where the chirp parameter is given by $\beta(z) = 1/(4\beta_{GVD}(z))\partial T^2(z)/\partial z$.

Equations (3.13a) - (3.13f) can be combined to yield coupled nonlinear envelope equations for the spot size R and pulse duration T as a function of propagation distance,

$$\frac{\partial^2 R(z)}{\partial z^2} = \frac{4}{k_0^2 R^3(z)}\left(M_{eff}^4(z) - \frac{P_{laser}(z)}{P_K(z)}\right), \tag{3.15a}$$

$$\frac{\partial^2 T(z)}{\partial z^2} = \frac{4\beta_{GVD}^2(z)}{T^3(z)}\left(1 + \frac{P_{laser}(z)}{P_K(z)}\frac{1}{k_0\beta_{GVD}(z)}\frac{T^2(z)}{R^2(z)}\right) + \frac{1}{\beta_{GVD}(z)}\frac{\partial\beta_{GVD}(z)}{\partial z}\frac{\partial T(z)}{\partial z}, \tag{3.15b}$$

where the laser power is $P_{laser}(z) = \pi E^2(z) R^2(z)/(4Z_0)$. The beam quality factor, M_{eff}^2, is heuristically introduced. The validity of this was benchmarked in full-scale wave-optics simulations and experiments [70,72] over distances of ~4 km.

In the case where the pulse propagates in vacuum, i.e., $\beta_{GVD} = 0$ and $\gamma_{NL} = 0$ $(P_K = \infty)$, the solutions to the dynamic equilibrium equations are $E(z) = E_0 R_0 / R(z)$,

$$R(z) = R_0\sqrt{1 - 2\alpha_0 z / Z_{R0} + (1 + \alpha_0^2) z^2 / Z_{R0}^2}, \tag{3.16}$$

$\alpha(z) = \alpha_0 - (1 + \alpha_0^2) z / Z_{R0}$, $T(z) = T_0$, $\varphi(z) = \tan^{-1}\left((\alpha_0 - Z_{R0}/z)^{-1}\right)$, and $\beta(z) = \beta_0$, where $Z_{R0} = k_0 R_0^2 / 2$ is the initial Rayleigh length.

3.2.1. Turbulence Model

In Eq. (3.15a) the quantity M_{eff}^2 is the effective beam quality factor which includes turbulence effects [67,68,70,72]. Atmospheric turbulence causes the spot size to spread and the centroid to wander. The effective spreading angle, for a Gaussian beam, due to diffraction and turbulence can be written as $\Theta_{eff}(z) = M_{eff}^2(z) R_0 / (\pi \lambda_0)$, where $M_{Eff}^2(z) = \sqrt{M_{BQ}^4 + M_{Turb}^4(z)}$ consists of the intrinsic beam quality factor and the turbulence contribution. For an ideal TEM_{00} Gaussian beam, $M_{BQ}^2 = 1$. An increase in M^2 above unity can arise from the presence of higher order modes at the source, termed intrinsic beam quality, M_{BQ}^2. The increase can also be due to the effects of the propagation medium, e.g., turbulence, denoted by M_{Turb}^2. The contribution due to turbulence has the form [72]

$$M_{Turb}^2(z) = 1.7 R_0 / r_0(z), \tag{3.17}$$

where $R_0 = R(0)$ is the initial spot size, $r_0(z) = 0.185 \lambda^{6/5} \left(\int_0^z C_n^2(z') dz' \right)^{-3/5}$ is the transverse coherence length [73], $z << 1/(k_0 C_n^2(z) l_0^{5/3})$, ℓ_0 is the inner scale-length of the turbulence [67,68,70] and is typically on the order of 1 mm, and $C_n^2(z)$ is the refractive index structure constant. The inequality on the propagation distance is well satisfied in our examples. The expression for $M_{Turb}^2(z)$ in Eq. (3.17) is shown to be in good agreement with full-scale wave-optic simulations [70] and experimental results [72]. Typical values for M_{BQ}^2 and M_{Turb}^2 used in our simulations are $M_{BQ}^2 \sim 1$ and $M_{Turb}^2 \sim 0 - 3$.

Laser beam wander can be an important effect [53]. In this analysis, we have estimated the amount of wander for the example in the following sections using the expressions in [47,73] and found the beam wander to be less than a few spot sizes. Note that in the dynamic equilibrium equation the spot size is directly affected by the turbulence, whereas the pulse duration is indirectly affected by turbulence through the spot size.

3.2.2. Possibility of Ionization and Defocusing

It can be seen that the effects on the laser spot size due to ionization in the atmosphere which lead to plasma defocusing are negligible in our parameter regime. The strength of effect of plasma defocusing can be evaluated by comparing terms in the envelope equations. Assuming the filament has a parabolic shape in the radial direction, with peak electron density on axis and radius $\rho_f \sim R(z)$, where $R(z)$ is the spot size, the envelope equation is

$$\frac{\partial^2 R(z)}{\partial z^2} = \frac{4}{k_0^2 R^3(z)}\left(M_{Eff}^4(z) - \frac{P_L(z)}{P_{NL}(z)} + \frac{k_p^2}{4\rho_f^2} R^4(z) \right), \tag{3.18}$$

where k_0 is the wavenumber associated with the wavelength of the laser, M_{eff}^2 is the beam quality factor, $P_L(z)$ is the laser power, $P_{NL}(z)$ is the nonlinear focusing power, and $k_p^2 = \omega_p^2 / c^2$ where $\omega_p^2 = q^2 n_e / m_e \varepsilon_0$ is the square of the plasma frequency, q is the electron charge, n_e is the electron density in the filament, m_e is the mass of the electron, and ε_0 is the permittivity of free space. The plasma defocusing can be evaluated by comparing the magnitude of the last term of Eq. (3.18) to the first two terms, which are of order unity.

The Keldysh parameter determines whether multiphoton ionization or tunneling ionization is dominant. The Keldysh parameter is defined as

$$\gamma_k = 2.31\times 10^6 \left(\frac{U_{ion}[\text{ev}]}{(\lambda^2[\mu\text{m}])(I[\text{W/m}^2])} \right)^{1/2}, \tag{3.19}$$

where U_{ion} is the ionization potential of an electron for a neutral molecule, λ is the wavelength of the laser, and I is the intensity. For our simulations, the Keldysh parameter $\gamma_k \gg 1$, which is the multiphoton ionization regime. The rate of multiphoton ionization of air, e.g., O_2 and N_2 molecules, is given by [5]

$$W_{mp} = \frac{2\pi\omega_0}{(l-1)!}\left(\frac{I(r,z,t)}{I_{mp}}\right)^l \tag{3.20}$$

where $l = \mathrm{Int}[U_{ion}/\hbar\omega_0 + 1]$, the minimum number of photons required for ionization, and $I_{mp} = \hbar\omega_0^2/\sigma_{mp}$ where $\sigma_{mp} = 6.4\times10^{-22}\ \mathrm{m}^2$, which is empirically determined [74,75]. For a $\lambda = 850$ nm pulse, $I_{mp} = 8.14\times10^{17}\ \mathrm{W/m}^2$. For the laser intensities considered in this section, the peak multiphoton ionization rate, $W_{mp} \sim 10^{-5}\ \mathrm{s}^{-1}$, is not high enough to induce significant plasma filamentation or beam defocusing. A 100 fs pulse would raise the electron density by $\sim 10^7\ \mathrm{m}^{-3}$. The last term in Eq. (3.18) is $k_{p0}^2 R^4(z)/4\rho_f^2 \sim 10^{-11} \ll 1$ for the electron density and parameters used in our simulations. Therefore, the contribution from this ionization process is negligible.

A greater source of plasma build up may be through photo detachment of negative ions in the atmosphere and subsequent collisional ionization. In order to show this, we can follow the same process used in Chapter 2 for photo detachment and collisional ionization in the atmosphere [1]. This process, due to single photo detachment of the ambient negative ions in the atmosphere and collisional ionization would produce some level of free electron density above the ambient level with our laser parameters. The free electron density could grow to $\sim 10^9\ \mathrm{m}^{-3}$, which is the density of ambient negative ions in the atmosphere. This is because the laser is able to photo detach the ambient negative ions. However, the laser pulse duration is not long enough near the focus of the pulse to initiate collisional ionization. The maximum collisional ionization rate at the peak intensity is ~10^{11} s^{-1}, while the pulse duration is $T(z) \sim 10^{-13}$. With this level of free electrons, the maximum value for the term $k_{p0}^2 R^4(z)/4\rho_f^2 \sim 10^{-9} \ll 1$. Therefore, ionization processes and plasma defocusing do not play significant roles in the beam propagation.

While multiphoton and collisional ionization processes do not play a role in affecting the pulse spot size, it is possible to use this formulation to investigate parameter regimes where tunneling ionization could generate plasma filaments with densities high enough to cause defocusing. In order to reach this regime, the peak intensity of the pulse on-axis would have to reach ~10^{18} W/m^2. A pulse with length ~1 ps and wavelength of 1 μm could readily ionize the air at this intensity through tunneling ionization. The plasma density would approach air density under these parameters and would cause significant defocusing, as is presented in Section 2.2.5.

3.3. Hybrid Modulation-Filamentation Instability

Laser beams propagating in a nonlinear medium can undergo a transverse filamentation and longitudinal modulation instability. In this section the evolution of the spatial and temporal perturbations on the laser pulse along the propagation direction are analyzed. In the stability model, the equilibrium state of the laser beam is dynamic, wherein the spot size and the pulse length evolve along the propagation path. The various instabilities associated with laser beams are analyzed by perturbing the dynamic equilibrium given in Eqs. (3.15a) and (3.15b). The hybrid filamentation-modulation instability arises from the coupling of the nonlinear refractive index, group velocity dispersion, and diffraction. The field amplitude is

$$A(r,z,\tau) = A_{eq}(r,z,\tau)(1 + a(r,z,\tau)), \tag{3.21}$$

where $A_{eq}a$ is the perturbation on the equilibrium, and $|a| << 1$. Substituting Eq. (3.21) into the full wave equation, Eq. (3.10), neglecting the mixed derivative term, and using the equilibrium equation satisfied by A_{eq} gives the following equation for the perturbation $a(r,z,\tau)$,

$$\begin{aligned}\nabla_\perp^2 a + 2(\nabla_\perp(\ln(A_{eq}))\cdot(\nabla_\perp a) + 2ik_0\frac{\partial a}{\partial z} - k_0\beta_{GVD}(z)\frac{\partial^2 a}{\partial \tau^2} - 2k_0\beta_{GVD}(z)\frac{\partial \ln(A_{eq})}{\partial \tau}\frac{\partial a}{\partial \tau} = \\ -2k_0\gamma_{NL}\left|A_{eq}\right|^2(a + a^* + a(a + aa^* + 2a^*))\end{aligned},$$

(3.22)

where $\nabla_\perp = \hat{\mathbf{e}}_x\partial/\partial x + \hat{\mathbf{e}}_y\partial/\partial y$. In deriving Eq. (3.22) the equilibrium equation in Eq. (3.11) was used together with $\nabla_\perp^2 A = \nabla_\perp^2 A_{eq} + 2(\nabla_\perp A_{eq})\cdot(\nabla_\perp a) + A_{eq}\nabla_\perp^2 a + a\nabla_\perp^2 A_{eq}$. The equilibrium terms in Eq. (3.22) are $\nabla_\perp(\ln(A_{eq})) = -2((1+i\alpha(z))/R^2(z))(x\hat{\mathbf{e}}_x + y\hat{\mathbf{e}}_y)$ and $\partial\ln(A_{eq})/\partial\tau = -2((1+i\beta(z))/T^2(z))\tau$. Substituting these relations into Eq. (3.22), and keeping terms to first order in a gives

$$\begin{aligned}\nabla_\perp^2 a - 4\frac{(1+i\alpha(z))}{R^2(z)}(x\hat{\mathbf{e}}_x + y\hat{\mathbf{e}}_y)\cdot(\nabla_\perp a) + 2ik_0\frac{\partial a}{\partial z} - k_0\beta_{GVD}(z)\frac{\partial^2 a}{\partial \tau^2} + 4k_0\beta_{GVD}(z)\frac{(1+i\beta(z))}{T^2(z)}\tau\frac{\partial a}{\partial \tau} = \\ -2k_0\gamma_{NL}\left|A_{eq}\right|^2(a + a^*)\end{aligned}.$$

(3.23)

Writing $a = a_R + ia_I$, where a_R and a_I are real, gives

$$\frac{\partial a_R}{\partial z} = -\frac{\nabla_\perp^2 a_I}{2k_0} + 2\frac{\mathbf{r}\cdot\nabla_\perp}{k_0R^2}(a_I + \alpha a_R) + \frac{\beta_{GVD}}{2}\frac{\partial^2 a_I}{\partial \tau^2} - \frac{2\beta_{GVD}\tau}{T^2}\frac{\partial(a_I + \beta a_R)}{\partial \tau}, \tag{3.24a}$$

$$\frac{\partial a_I}{\partial z} = \frac{\nabla_\perp^2 a_R}{2k_0} - 2\frac{\mathbf{r}\cdot\nabla_\perp}{k_0R^2}(a_R - \alpha a_I) + 2\gamma_{NL}\left|A_0\right|^2 a_R - \frac{\beta_{GVD}}{2}\frac{\partial^2 a_R}{\partial \tau^2} + \frac{2\beta_{GVD}\tau}{T^2}\frac{\partial(a_R - \beta a_I)}{\partial \tau}, \tag{3.24b}$$

where $A_0(r,\tau) = E(0)\exp\left(-r^2/R^2(z)\right)\exp\left(-\tau^2/T^2(z)\right)$.

3.3.1. Constant, Finite Spot Size and Pulse Duration Limit

In this subsection the laser pulse spot size, R, and pulse duration, T, are taken to be constant, i.e., $R = R_0$ and $T = T_0$ and the curvature and chirp parameters are neglected. The spot size and pulse duration are chosen to be constant in order to analytically calculate the growth rate of the hybrid instability. However, in the numerical simulations, the spot size and pulse duration evolve self-consistently. The equations for a_R and a_I become

$$\frac{\partial a_R}{\partial z} = -\frac{\nabla_\perp^2 a_I}{2k_0} + \frac{\beta_{GVD}}{2}\frac{\partial^2 a_I}{\partial \tau^2} + \frac{\mathbf{r}\cdot\nabla_\perp a_I}{Z_{R0}} - \frac{\tau}{Z_{T0}}\frac{\partial a_I}{\partial \tau}, \tag{3.25a}$$

$$\frac{\partial a_I}{\partial z} = \frac{\nabla_\perp^2 a_R}{2k_0} + 2\gamma_{NL}\left|A_0\right|^2 a_R - \frac{\beta_{GVD}}{2}\frac{\partial^2 a_R}{\partial \tau^2} - \frac{\mathbf{r}\cdot\nabla_\perp a_R}{Z_{R0}} + \frac{\tau}{Z_{T0}}\frac{\partial a_R}{\partial \tau}, \tag{3.25b}$$

where $Z_{R0} = k_0 R_0^2 / 2$ and $Z_{T0} = T_0^2 / (2\beta_{GVD})$. The amplitudes are expressed in the form $a_R = \hat{a}_R(\mathbf{k},\omega)\exp(i\tilde{\psi}(\mathbf{r},\tau)) + c.c.$ and $a_I = \hat{a}_I(\mathbf{k},\omega)\exp(i\tilde{\psi}(\mathbf{r},\tau)) + c.c.$ where $\tilde{\psi}(\mathbf{r},\tau) = \mathbf{k}_\perp\cdot\mathbf{r} + k_z z - \omega\tau$ and $\mathbf{k}_\perp = k_x\hat{\mathbf{x}} + k_y\hat{\mathbf{y}}$ and ω are specified. The initial noise spectrum is represented by $\hat{a}_R$, $\hat{a}_I$ for each combination of k_x, k_y, and ω. Equations (3.25a) and (3.25b) become

$$ik_z\hat{a}_R = \left(\frac{k_\perp^2}{2k_0} - \frac{\beta_{GVD}\omega^2}{2} + i\kappa_{RT}(k_\perp,\omega)\right)\hat{a}_I, \tag{3.26a}$$

$$ik_z\hat{a}_I = \left(-\frac{k_\perp^2}{2k_0} + 2\gamma_{NL}\left|A_0\right|^2 + \frac{\beta_{GVD}\omega^2}{2} - i\kappa_{RT}(k_\perp,\omega)\right)\hat{a}_R, \tag{3.26b}$$

where $\kappa_{R,T}(k_\perp,\omega,R_0,T_0) = \mathbf{k}_\perp\cdot\mathbf{r}/Z_{R0} + \omega\tau/Z_{T0}$ represents the finite spot size and pulse duration effects. The dispersion relation for the hybrid filamentation-modulation instability for a finite spot size and finite laser pulse duration is

$$k_z^2 = \frac{1}{4k_0^2}\left(k_\perp^2 - k_0\beta_{GVD}\omega^2 + 2ik_0\kappa_{RT}\right)\left(k_\perp^2 - k_0\beta_{GVD}\omega^2 - (P_{laser}/P_K)/R_0^2 + 2ik_0\kappa_{RT}\right), \quad (3.27)$$

where $k_\perp^2 = k_x^2 + k_y^2$, $(P_{laser}/P_K) = k_0\gamma_{NL}\left|E_0\right|^2 R_0^2$, and $E_0 = E(z=0)$.

3.3.2. Long, Broad Pulse Limit

In the case where both the spot size and pulse duration are sufficiently large so that $\kappa_{R,T}$ can be neglected, Eqs. (3.25a) and (3.25b) reduce to

$$\frac{\partial a_R}{\partial z} = -\frac{\nabla_\perp^2 a_I}{2k_0} + \frac{\beta_{GVD}}{2}\frac{\partial^2 a_I}{\partial \tau^2}, \quad (3.28a)$$

$$\frac{\partial a_I}{\partial z} = \frac{\nabla_\perp^2 a_R}{2k_0} + 2\gamma_{NL}\left|A_0\right|^2 a_R - \frac{\beta_{GVD}}{2}\frac{\partial^2 a_R}{\partial \tau^2}. \quad (3.28b)$$

Substituting $(a_R, a_I) = (\hat{a}_R, \hat{a}_I)\exp(i\tilde{\psi}(\mathbf{r},\tau)) + c.c.$ into Eqs. (3.28a) and (3.28b) and solving for the axial wavenumber gives

$$k_z^2 = \frac{1}{4k_0^2}\left(k_\perp^2 - k_0\beta_{GVD}\omega^2\right)\left(k_\perp^2 - k_0\beta_{GVD}\omega^2 - 4k_0\gamma_{NL}\left|E_0\right|^2\right), \quad (3.29)$$

where $\hat{a}_R / \hat{a}_I = -i(k_\perp^2/k_0 - \beta_{GVD}\omega^2)/2k_z$. The spatial growth rate, $\Gamma = -\mathrm{Im}[k_z]$, as a function of the parameters $k_\perp, \omega$, and P_{laser}/P_K is shown in Fig. 3.2. It can be seen from Eq. (3.29) that a transverse instability will arise as long as the nonlinear index of refraction is nonzero. An important consequence of Eq. (3.29) is that when the nonlinear refractive index and the group velocity dispersion are nonzero a hybrid transverse-longitudinal instability develops. The growth rate of the hybrid instability is maximum when the combination of $k_\perp$ and ω satisfies

$$k_\perp^2 - k_0\beta_{GVD}\omega^2 = \frac{2}{R_0^2}\frac{P_{laser}}{P_K} \quad (3.30)$$

where we used $k_0\gamma_{NL}\left|E_0\right|^2 = R_0^{-2}P_{laser} / P_K$. The growth rate is non zero in the interval $0 < k_\perp^2 - k_0\beta_{GVD}\omega^2 < 4(P_{laser} / P_K) / R_0^2$ and has the maximum value

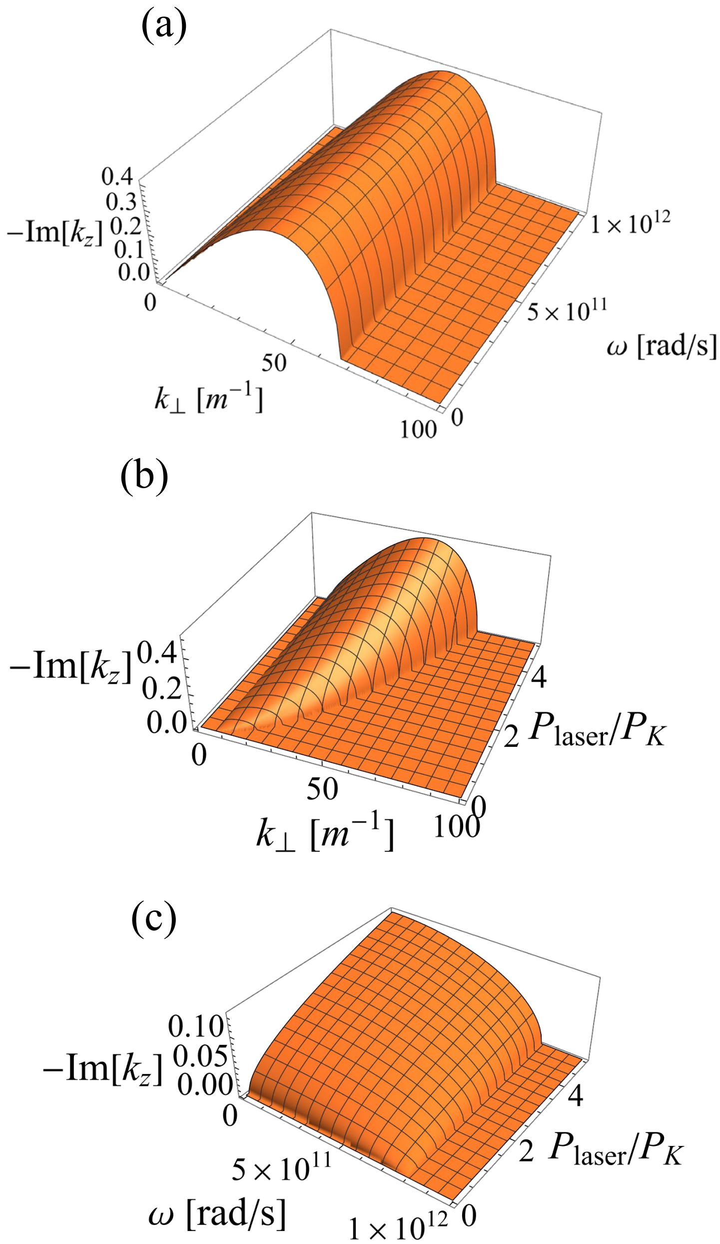

Figure 3.2. Growth rate of the plane wave instability for a pulse with $R_0 = 6$ cm. (a) Plot of the growth rate as a function of $k_\perp$ and ω, $P_L / P_{NL} = 4$. (b) Plot of the growth rate as a function of $k_\perp$ and P_L / P_{NL}, $\omega = 5\times10^{11}$ rad/s. (c) Plot of the growth rate as a function of ω and P_L / P_{NL}, $k_\perp = 10\ \mathrm{m}^{-1}$.

$$\Gamma_{\max} = \frac{1}{k_0 R_0^2}\left(\frac{P_{laser}}{P_K}\right). \tag{3.31}$$

In the absence of group velocity dispersion, we can associate $k_\perp$ at the maximum growth rate with a filament spot size radius of $R_f \approx \pi / 2k_\perp$. The number of optical filaments in the beam, $N_f \approx (R_0 / R_f)^2$, is given by $N_f \approx (8/\pi^2) P_{laser} / P_K$, where N_f is nearly the ratio of P_{laser} / P_K [37].

Figures 3.2(a), (b), and (c) plot the spatial growth rate of the hybrid instability, obtained from Eq. (3.29), as a function of $(k_\perp, \omega)$, $(k_\perp, P_{laser} / P_K)$, and $(\omega, P_{laser} / P_K)$, respectively. In Fig. 3.2(a), the wavenumber cutoff can be seen, which imposes a limit on the minimum size of a filament. Growth of the hybrid instability is limited to the ranges of $k_\perp$ and ω that satisfy Eq. (3.30). Figure 3.2(b) shows the linear relation between the transverse wavenumber with the maximum growth rate and the ratio of laser power to nonlinear focusing power. This relationship supports the fact that filaments contain a power approximately equal to the nonlinear focusing power. Figure 3.2(c) shows the frequency cutoff, above which there is no growth of the instability. This frequency cutoff limits the minimum size of the longitudinal modulations.

3.4. Simulation Results

In this section, simulations of the dynamic equilibrium are presented. Figure 3.3 is a schematic of the laser pulse propagation geometry. In the simulations, the laser pulses are propagated vertically, from ground level, through the atmosphere over distances >50 km. The strength of the turbulence, group velocity dispersion, and air density vary with altitude. The air density decreases with altitude approximately exponentially with an e-folding length of ~7.5 km [76]. The group velocity dispersion and nonlinear refractive index are both proportional to the air

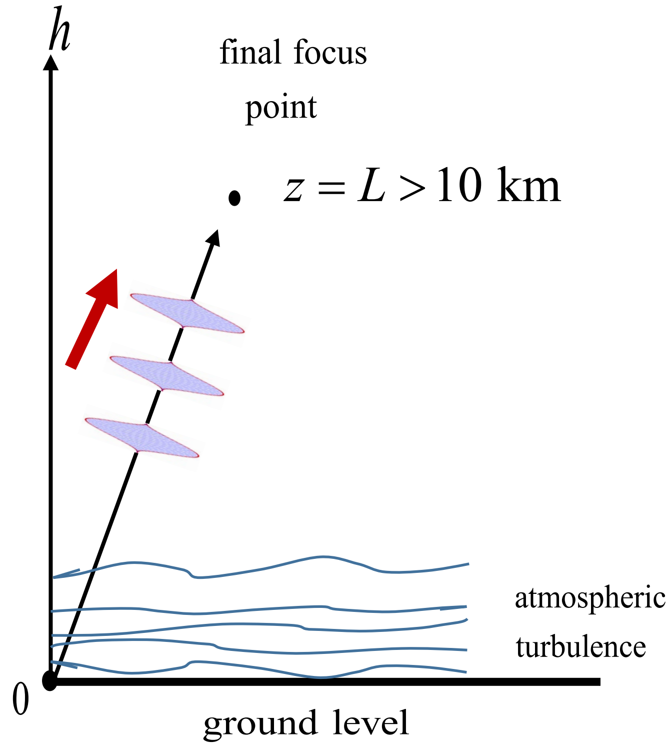

Figure 3.3. Schematic of the vertical propagation of the laser pulses through the atmosphere. The pulses are initiated at ground level and travel through the atmosphere in the direction of the arrow. Various parameters, such as turbulence strength level, group velocity dispersion, and air density vary with altitude.

density. Figure 3.4 shows the variation of the structure constant, C_n^2, associated with turbulence as a function of altitude [77]. The model used in our simulations is

$$C_n^2(z) = \begin{cases} C_n^2(0)\exp\left(-(4h(z)/L_{Turb})^{1/2}\right), & z < 16 \text{ km} \\ C_n^2(0)\exp\left(-(h(z)/L_{Turb})^{3/2}\right), & z \geq 16 \text{ km} \end{cases}, \tag{3.32}$$

where $C_n^2(0)$ is taken to be 10^{-15} $\text{m}^{-2/3}$, $h(z)$ is the altitude, and $L_{Turb} = 8$ km is the characteristic scale length for turbulence. Typical low-to-moderate ground level values of C_n^2 are $10^{-16} - 10^{-14}\,\text{m}^{-2/3}$. The value we have chosen for the example in this section represents low to moderate turbulence. Equation (3.32) was chosen to match the turbulence strength curves in

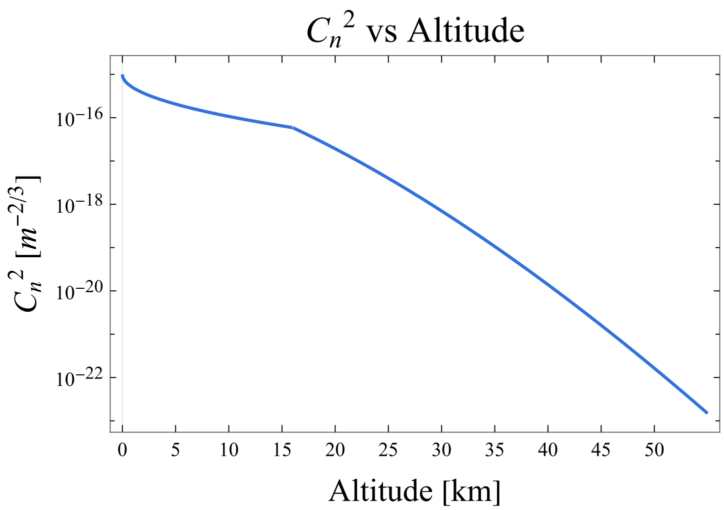

Figure 3.4. Indicates the level of turbulence as a function of altitude in terms of the refractive index structure constant C_n^2 [77].

previous work [77]. This particular model matches the Hufnagel-Valley model in the absence of strong ground-based turbulence.

Initial peak intensity, I_{laser}	7 x 10^{11} W/m^2
Pulse energy, ε	0.21 J
Wavelength, λ_0	850 nm
Initial spot size, R_0	6 cm
Initial pulse duration, T_0	30 ps
Peak pulse power, $P(0)$	4 x 10^9 W
$P_{laser}(0)/P_K(0)$	3.86
Intrinsic beam quality, M_{BQ}^2	1
M^2 due to turbulence, M_{Turb}^2	0-1.5
Structure constant, $C_n^2(0)$	10^{-15} m$^{-2/3}$
Group velocity dispersion, $\beta_{GVD}(0)$	2.1 x 10^{-29} s^2/m
Initial wavefront curvature, $\alpha(0)$	-1.1
Frequency chirp, $\Delta\omega(0)/\omega_0$	-17.2%
Propagation range	50 km

Table 3.1. List of the laser pulse and atmospheric parameters used in the simulations (50 km propagation).

3.4.1. Long-range Dynamic Equilibrium

The dynamic equilibrium equations, Eqs. (7a) and (7b), are numerically solved using the parameters in Table I. The goal of this example is to focus the laser pulse transversely and longitudinally at nearly the same remote location in order to significantly enhance the intensity. Figure 3.5(a) and 3.5(b) show the spot size and pulse duration as a function of propagation distance. Figure 3.5(c) shows the beam quality factor due to turbulence, M_{Turb}^2, as a function of propagation distance. The intensity enhancement as a function of propagation distance is shown in Fig. 3.5(d). The maximum intensity enhancement is ~1000 and occurs at 50 km.

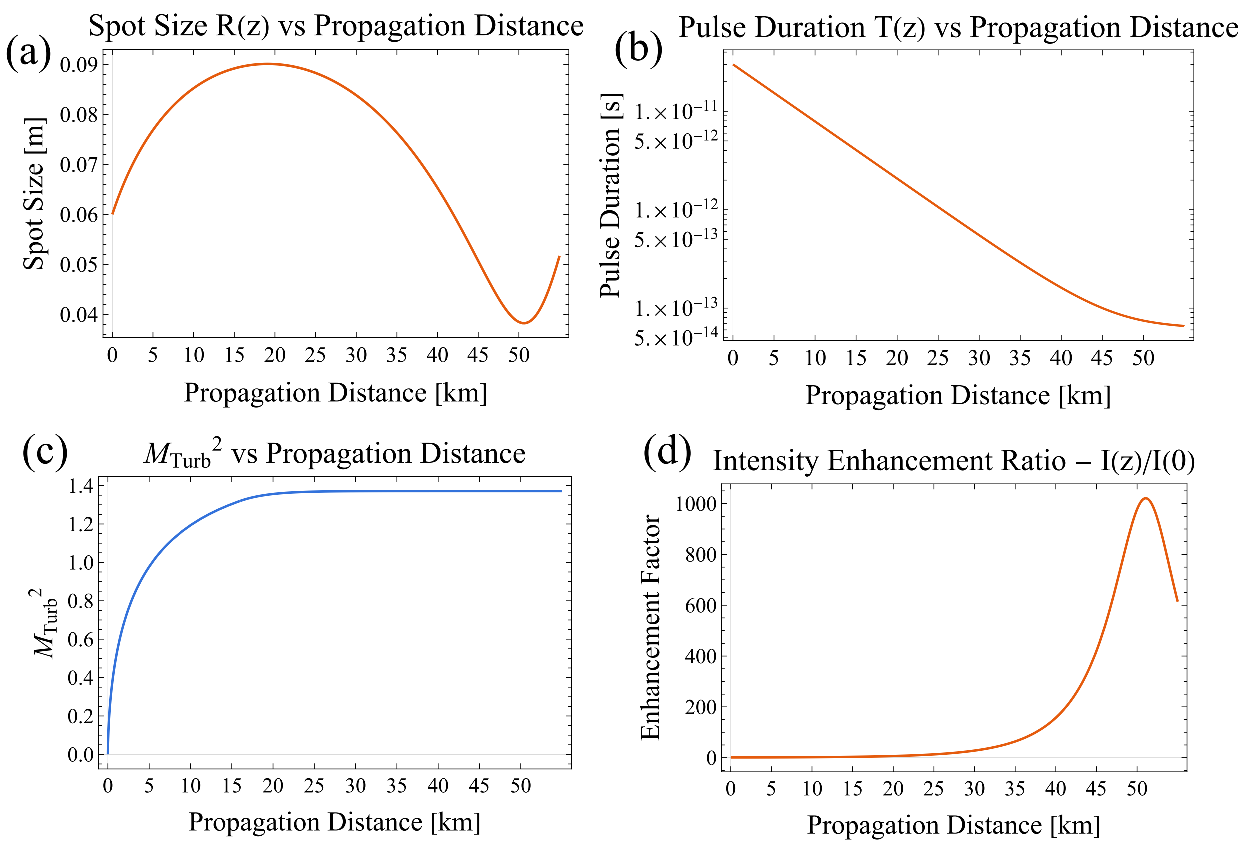

Figure 3.5. (a), (b) Variation of the laser spot size pulse duration as functions of propagation distance. (c) Beam quality factor due to atmospheric turbulence M_{Turb}^2 as a function of altitude. (d) Normalized laser intensity as a function of propagation distance. The peak intensity enhancement occurs at the location where both the spot size and pulse duration are near their minimum values. The parameters for these simulations are listed in Table 3.1.

3.4.2. Hybrid Filamentation-Modulation Instability

In this section simulation results for the hybrid filamentation-modulation instability are presented. The quantities a_R and a_I, defined following Eqs. (3.24a) and (3.24b), can be represented in terms of discrete Fourier series,

$$a_R(x,y,z,\tau)=\sum_{n,l,s} a_{n,l,s}(z)\exp(i\psi_{n,l,s}(x,y,\tau)), \tag{3.33a}$$

$$a_I(x,y,z,\tau)=\sum_{n,l,s} b_{n,l,s}(z)\exp(i\psi_{n,l,s}(x,y,\tau)), \tag{3.33b}$$

where $\psi_{n,l,s}(x,y,\tau)=k_n x+k_l y-\omega_s\tau$ and the sum over the integers n, l, and s is from $-\infty$ to ∞. Since a_R and a_I are real, $a_{n,l,s}=a^*_{-n,-l,-s}$ and $b_{n,l,s}=b^*_{-n,-l,-s}$. In addition, $k_n(z)=2\pi n/NR(z)$, $k_l(z)=2\pi l/NR(z)$, $\omega_s(z)=2\pi s/NT(z)$, and N is a large integer which takes into account the spot size and pulse duration. The spot size $R(z)$ and pulse duration $T(z)$ are obtained from the dynamic equilibrium in Eqs. (3.15a) and (3.15b). Substituting the representations in Eqs. (3.33a) and (3.33b) into Eqs. (3.24a) and (3.24b), multiplying by $\exp(-i\psi_{m,j,q}(x,y,\tau))$, and integrating over x, y, and τ gives

$$\frac{\partial a_{m,j,q}}{\partial z}=\sum_{n,l,s} KA_{m,n,j,l,q,s}a_{n,l,s}+KB_{m,n,j,l,q,s}b_{n,l,s}\ , \tag{3.34a}$$

$$\frac{\partial b_{m,j,q}}{\partial z}=\sum_{n,l,s}-\left(KB_{m,n,j,l,q,s}-\frac{2}{k_0R_0^2}\frac{P_0}{P_{NL}}\left(\frac{E}{E_0}\right)^2 H_{n,m}H_{l,j}F_{s,q}\right)a_{n,l,s}+KA_{m,n,j,l,q,s}b_{n,l,s}\ , \tag{3.34b}$$

where the coefficients are given by

$$\begin{aligned}KA_{m,n,j,l,q,s}=&\frac{2i\alpha}{k_0R^2}\left(k_nG_{n,m}\delta_{l,j}\delta_{s,q}+k_l\delta_{n,m}G_{l,j}\delta_{s,q}\right)+\frac{2i\beta_{GVD}\omega_s}{T^2}\beta\delta_{n,m}\delta_{l,j}J_{s,q}\\ &-i\sum_{n,l,s}\left(\frac{\partial k_m}{\partial z}G_{n,m}\delta_{l,j}\delta_{s,q}+\frac{\partial k_l}{\partial z}\delta_{n,m}G_{l,j}\delta_{s,q}-\frac{\partial\omega_q}{\partial z}\delta_{n,m}\delta_{l,j}J_{s,q}\right)\end{aligned}\ , \tag{3.35a}$$

$$KB_{m,n,j,l,q,s} = \frac{(k_n^2 + k_l^2 - \beta_{GVD} k_0 \omega_s^2)}{2k_0} \delta_{n,m} \delta_{l,j} \delta_{s,q} + \frac{2i}{k_0 R^2} \left(k_n G_{n,m} \delta_{l,j} \delta_{s,q} + k_l \delta_{n,m} G_{l,j} \delta_{s,q} \right) + \frac{2i \beta_{GVD} \omega_s}{T^2} \delta_{n,m} \delta_{l,j} J_{s,q} . \quad (3.35b)$$

The derivation of the coefficients in Eqs. (3.34a), (3.34b), (3.35a), and (3.35b) are given in the Appendix.

The hybrid filamentation-modulation instability is studied by numerically solving Eqs. (3.34a) and (3.34b). The transverse filamentation of the pulse is shown in Figs. 3.6(a) and (b). The

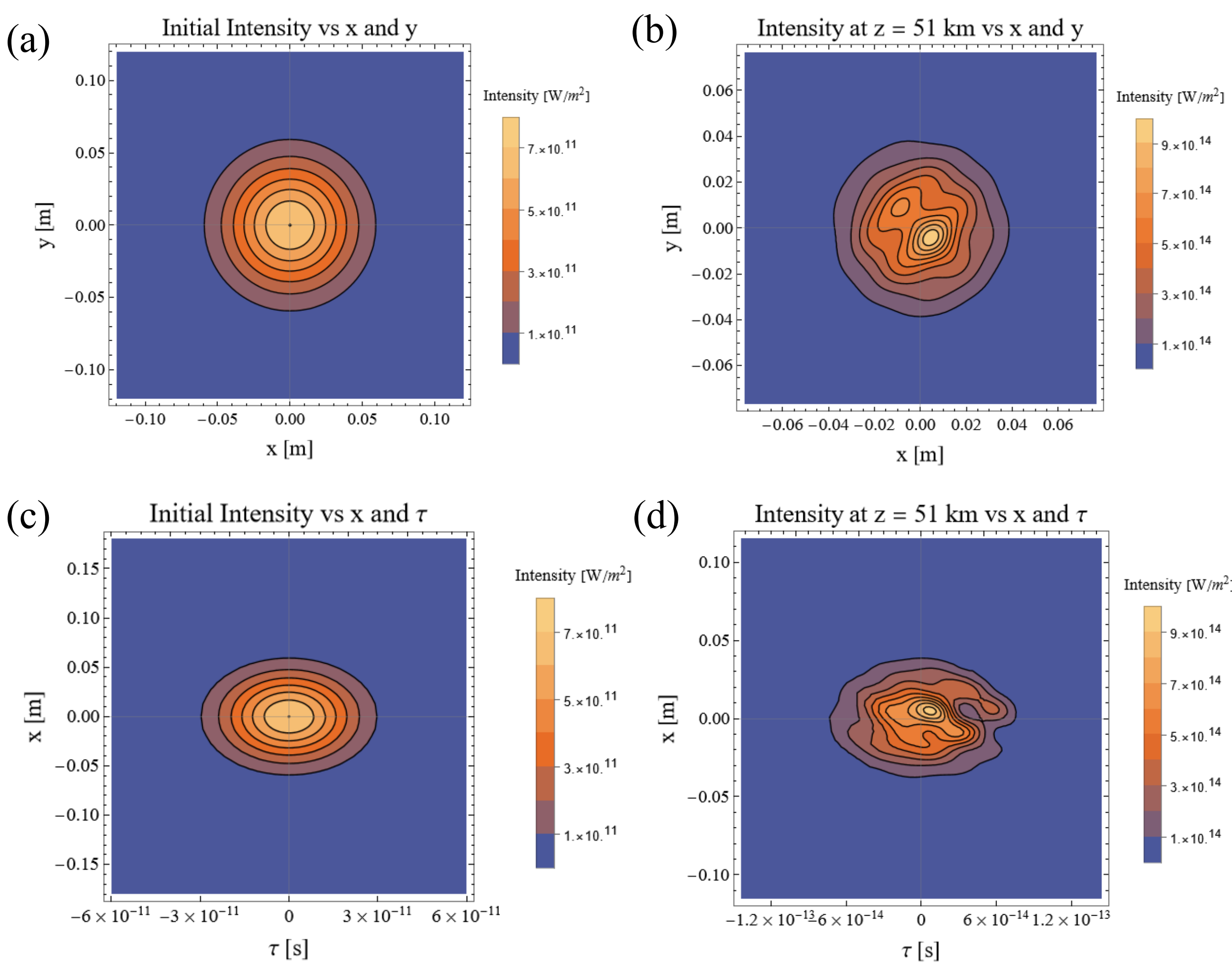

Figure 3.6. Cross sections of the laser pulse as it propagates through the atmosphere. (a), (c) show the initial beam profile and intensity, (b), (d) show the profile and intensity at the point of maximum intensity enhancement, i.e., at 51 km. The top row of figures (a, b) shows the profile in the x-y plane while the bottom row (c, d) shows the profiles in the x-τ plane. The parameters used in these simulations are shown in Table 3.1.

longitudinal modulation of the pulse is shown in Figs. 3.6(c) and (d). The initial noise level in the pulse is not known, therefore, in our simulations the noise levels were chosen such that the absolute value for the perturbation, |a|, approached unity at the focal point for the pulse. The instability undergoes ~25 e-folds in magnitude over the propagation path. This is similar to stimulated Brillouin scattering, which undergoes 25-30 e-folds before reaching saturation [37]. Figures 3.6 and 3.7 show simulation results that were generated using the parameters in Table 3.1, i.e., the 51 km propagation example. Figure 3.6 shows the initial pulse profile in (a) the x-y and (c) x-τ planes, as well as the intensity profiles at the focal points (b, d) after 51 km of propagation. The beam distortion and breakup due to the instabilities can be observed. Figure 3.7 shows a 3D plot of the pulse intensity in (a) the x-y and (b) x-τ plane, where the beam breakup is visible.

The beam breaks up transversely and longitudinally into individual beamlets. The beamlets each contain a power approximately equal to the nonlinear focusing power. These results are consistent with those reported in [5,37,55].

3.5. Discussion

This Chapter presents analysis and simulations of the propagation of laser pulse in the atmosphere. Simulations are performed for vertical propagation from ground level. The varying

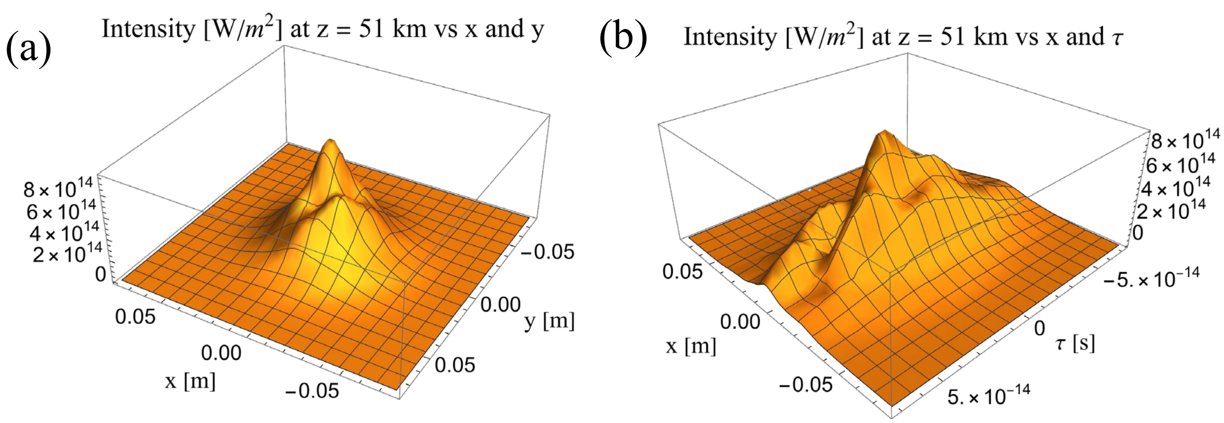

Figure 3.7. Intensity of the beam at 51 km in 3D. (a) Shows the intensity of the beam in the x-y plane and (b) shows the beam in the x-τ plane.

atmospheric density, group velocity dispersion, and level of turbulence as functions of altitude are taken into account. Stability of laser pulses propagating extended distances is analyzed and simulated.

I have derived a set of coupled, nonlinear envelope equations describing the dynamic equilibrium of the laser spot size and pulse duration. The envelope equations include turbulence effects and beam quality effects, as well as linear and nonlinear (Kerr) dispersion. The model is valid in the paraxial approximation, where the electric field envelope varies slowly with respect to the wavelength. By appropriately tailoring the laser pulse parameters, the pulse can be spatially and temporally focused to high intensities in the upper atmosphere. Tailoring of the laser parameters involves the optimum level of i) frequency chirping, ii) initial wave front curvature, and iii) ratio of laser pulse power to the nonlinear focusing power. Our simulations indicate that transverse and longitudinal focusing together can result in significant pulse intensity enhancements.

The hybrid filamentation-modulation instability of the laser pulse is shown to result in transverse and longitudinal pulse breakup. Transverse breakup of the pulse leads to the formation of beamlets, each with a power approximately equal to the nonlinear focusing power, which is consistent with previous results [5,37,55].

The effects of plasma defocusing on the laser pulse are not considered in this section. The laser pulses used in simulations in this section are able to ionize the negative ions in the atmosphere, such as O_2^-, however, the ambient density of negative ions in the atmosphere is not high enough to influence the laser pulse [1,5,31,35]. The effects of multiphoton and collisional ionization from neutral molecules can be neglected. In this study, the intensity of the laser pulses is below the threshold for ionization. However, propagation of laser pulses at high altitudes (>100 km) could be affected by the presence of free electrons in the various ionosphere layers, i.e., E, F, and D regions.

It is possible to use this propagation for pulses that reach intensities high enough for tunneling ionization to occur. By properly tailoring the pulse, a plasma filament could be generated at remote locations with electron densities near air density. This could be used in tandem with a low-intensity LPT which follows the high-intensity pulse. The leading, high-intensity pulse would ionize the air through tunneling ionization. Then, the trailing, low-intensity LPT would drive the electrons in the filament to oscillate and emit RF radiation.

The numerical model allows for laser pulse propagation simulations over extended distances. Using full-scale wave-optics simulations to study these coupled instabilities can be computationally challenging.

Chapter 4: Parametric Frequency Conversion in the Ionosphere for Over-the-Horizon Radar

The ionospheric electron, ion, and neutral densities have a significant effect on over-the-horizon (OTH) radar systems [78,79] and worldwide communication networks, space-based telescopes, and on the life spans of low-earth-orbit (LEO) satellites [80-85]. The ionosphere consists of various layers, D, E, and F [76]. The F layer has the highest concentration of free electrons. In the F layer (150 - 600 km) the electron density is $10^{11} - 10^{12}\ \mathrm{m}^{-3}$, the neutral density is $10^{13} - 10^{17}\ \mathrm{m}^{-3}$, and the electron collision frequency is $10 - 10^{3}\ \mathrm{Hz}$. The ion and electron densities are essentially equal due to charge neutrality and the peak electron density occurs around 300 - 400 km. Over-the-horizon radar systems and navigation systems, such as GPS, depend on knowing ionospheric conditions, i.e., electron, ion, and neutral densities.

Solar flares have a significant effect on the ionosphere and can rapidly increase the ionization levels by up to an order of magnitude [86,87]. Increases in the electron density in the various ionospheric layers, due to enhanced solar activity, can result in sudden OTH radar loss, communication loss, radio blackouts, signal delays, GPS positioning errors, disruption of space-based telescopes, and increased drag on LEO satellites. The US Navy uses atmospheric models, such as the NRL NRLMSISE-00 model, to estimate the ion (electron) concentrations for OTH radar and communication systems. Direct measurements of the electron density can improve these models.

A number of countries have OTH radars which are used for early warning systems of ICBM launches and for surveillance over extended distances, ~ 3000 km [78,79]. Over-the-horizon radar signals rely on reflecting low frequency signals off electron density layers in the ionosphere. These systems generate output power signals in the multi-MW regime, at frequencies in the MHz range. The major OTH radar countries include: the USA, China, Russia, Iran, Canada, UK, Australia, India, France, and Brazil. The transmitting and receiving antennas for these systems are extremely large, extending over distances of many kilometers. The cost of OTH radar systems can be well over a billion dollars each.

In this chapter, I present a mechanism for generating low frequency signals in the ionosphere and propagating them back to the ground far from the source. The concept can be used to develop a compact, mobile, low cost OTH radar system and/or to characterize ionospheric parameters, such as the electron density as a function of altitude.

4.1. Parametric Frequency Conversion Model

In this section, I present the model for generating low frequency signals in the ionosphere and propagating them back to ground level far from the source. The overall schematic describing the configuration is shown in Fig. 4.1. The low frequency signal in the ionosphere is generated by a ground-based, frequency modulated, radio frequency source. The driving source parametrically generates a beat wave in the ionosphere which generates a driving current. Tuning the modulation frequency to the local plasma frequency resonantly excites a current that increases in time and excites a low frequency signal. The low frequency signal propagates back to the observation point on the ground.

The electric fields of the ground-based driving signals are given by $\mathbf{E}_1(z,t) = E_1 \exp\left(i(k_1 z - \omega_1 t)\right)\hat{\mathbf{x}}/2 + c.c.$ and $\mathbf{E}_2(z,t) = E_2 \exp\left(i(k_2 z - \omega_2 t)\right)\hat{\mathbf{x}}/2 + c.c.$. The corresponding magnetic fields are $\mathbf{B}_1(z,t) = E_1 n_1 \exp\left(i(k_1 z - \omega_1 t)\right)\hat{\mathbf{y}}/2c + c.c.$ and $\mathbf{B}_2(z,t) = E_2 n_2 \exp\left(i(k_2 z - \omega_2 t)\right)\hat{\mathbf{y}}/2c + c.c.$, where $n_1 = ck_1/\omega_1$ and $n_2 = ck_2/\omega_2$ are the indices

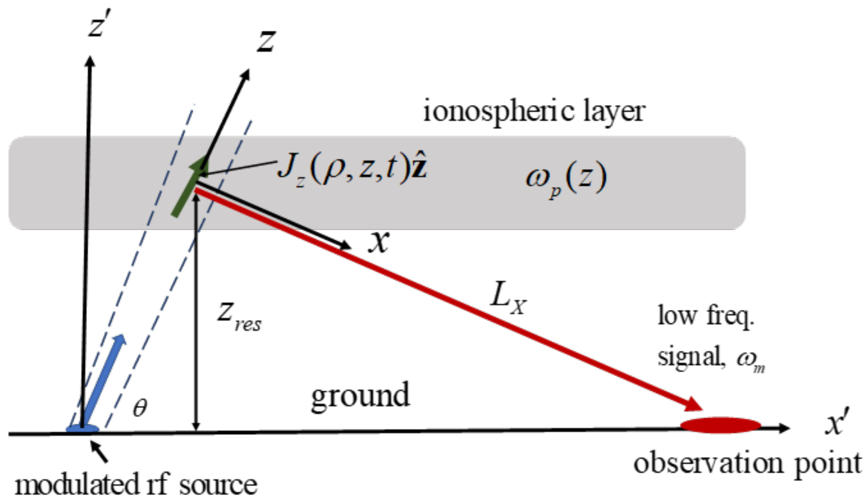

Figure 4.1. Shows the ground-based, modulated RF source propagating into the atmosphere. The ponderomotive forces from the RF source resonantly generate a current at the modulation frequency, i.e., local plasma frequency. The current, in turn, generates a low-frequency signal, which propagates back to the observation point on the ground.

of refraction and *c.c.* denotes complex conjugation. In the ionosphere the driving signal excites a beat wave, i.e., a ponderomotive wave. The axial component of the ponderomotive force is

$$\mathbf{F}_{pond}(z,t) = qE_{pond}\sin(k_m z - \omega_m t)\hat{\mathbf{z}}\,, \tag{4.1}$$

where the modulation frequency and wavenumber of the ponderomotive wave are $\omega_m = \omega_2 - \omega_1$ and $k_m = k_2 - k_1$ and the amplitude is $E_{pond} = qk_m E_1^* E_2 / (2m\omega_1\omega_2)$ [1]. Taking $E_1 = E_2 = E$ and $\omega_1 \approx \omega_2 \approx \omega >> \omega_m$, the ponderomotive wave amplitude is

$$E_{pond} = \frac{qZ_0}{mc}\frac{\omega_m}{\omega^2} I\,, \tag{4.2}$$

where $I = |E|^2 / (2Z_0)$ is the intensity and $Z_0 = \sqrt{\mu_0 / \varepsilon_0}$. Diffraction plays an important role as the ponderomotive field propagates to the ionosphere. The source spot size, with respect to the field amplitude, at ground level, is $R_S(0)$ and the spot size in the ionosphere at altitude z is $R_S(z) = R_S(0)z / Z_R(0) = \lambda z / \pi R_S(0)$, where $Z_R(0) = \pi R_S^2(0) / \lambda$ is the Rayleigh length and

$\lambda = 2\pi c / \omega$ is the source wavelength. The source intensity in the ionosphere, assuming a Gaussian transverse profile, is

$$I(\rho, z) = (R_S(0) / R_S(z))^2 I(0,0) \exp(-2\rho / R_S(z))^2, \tag{4.3}$$

where $I(0,0)$ is the on-axis intensity at ground level.

4.1.1. Low Frequency Driving Current

The fluid model is given by

$$\frac{\partial V(z,t)}{\partial t} + V(z,t)\frac{\partial V(z,t)}{\partial z} + \Gamma V(z,t) = \frac{q}{m}\left(E(z,t) + E_{NL}(z,t)\right) - \frac{k_B T}{mN(z,t)}\frac{\partial N(z,t)}{\partial z}, \tag{4.4a}$$

$$\frac{\partial E(z,t)}{\partial t} = -\frac{J(z,t)}{\varepsilon_0}, \tag{4.4b}$$

$$\frac{\partial N(z,t)}{\partial t} + \frac{\partial\left(N(z,t)V(z,t)\right)}{\partial z} = 0, \tag{4.4c}$$

$$\frac{\partial E(z,t)}{\partial z} = \frac{q}{\varepsilon_0}\left(N(z,t) - N_0(z)\right), \tag{4.4d}$$

where $V(z,t)$ is the electron velocity in the *z*-direction, Γ is the electron collision frequency, $E(z,t)$ is the space charge electric field, $N(z,t)$ is the electron density, k_B is the Boltzmann constant, T is the electron temperature, m is the electron mass, $J(z,t) = qN(z,t)V(z,t)$ is the electric current density, and $N_0(z)$ is the initial electron density. We assume that the magnetic field is negligible in our model, as the fluid velocities are much less than the speed of light. The last term on the right-hand side of Eq. (a) represent the force due to pressure. The force due to pressure is $F_{pressure} = -(mN)^{-1}\partial P / \partial z$ where $P = Nk_B T$, though this term is neglected in this analysis.

The nonlinear fluid equations are analyzed in Appendix D. However, Eqs. (4.4a) - (4.4d) can be linearized to simplify the model. The linearized 1-D fluid equations used to evaluate the low frequency driving current are

$$\frac{\partial V(z,t)}{\partial t}+\Gamma V(z,t)=\frac{q}{m}\left(E(z,t)+E_{pond}(z,t)\right)-\frac{k_B T}{mN_0(z)}\frac{\partial n(z,t)}{\partial z}, \tag{4.5a}$$

$$\frac{\partial E(z,t)}{\partial t}=-\frac{J(z,t)}{\varepsilon_0}, \tag{4.5b}$$

$$\frac{\partial n(z,t)}{\partial t}+\frac{\partial\left(N_0(z)V(z,t)\right)}{\partial z}=0, \tag{4.5c}$$

$$\frac{\partial E(z,t)}{\partial z}=\frac{qn(z,t)}{\varepsilon_0}, \tag{4.5d}$$

where $J(z,t)=qN_0(z)V(z,t)$ is the current density and $n(z,t)$ is the perturbed electron density. The magnetic field is neglected since fluid velocities are much less than c and the model is 1-D. The current density is linearized as $N(z,t)=N_0(z)+n(z,t)$ where $N_0(z)>>n(z,t)$. We have neglected the static pressure term, proportional to $\partial N_0(z)/\partial z$.

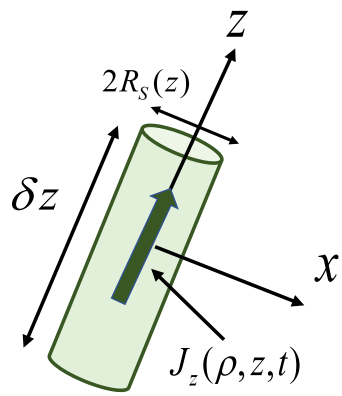

Figure 4.2. Shows the interaction volume where the ground-based source generates a current density in the ionosphere. The *z*-direction is the direction of propagation of the ground-based source. The low-frequency signal propagates radially, perpendicular to the *z*-direction. Note that the origin of the coordinate system is at a height of z_{res} above the ground.

The fluid equations in Eqs. (4.5a) - (4.5d) can be rearranged to obtain an equation for the current density,

$$\frac{\partial^2 J(z,t)}{\partial t^2}+\Gamma\frac{\partial J(z,t)}{\partial t}+\omega_p^2(z)J(z,t)-\mathrm{v}_{th}^2\frac{\partial^2 J(z,t)}{\partial z^2}=\varepsilon_0\omega_p^2(z)\frac{\partial E_{pond}(z,t)}{\partial t}, \tag{4.6}$$

where $\omega_p^2(z)=q^2N_0(z)/m\varepsilon_0$ and $\mathrm{v}_{th}=\sqrt{k_BT/m}$ is the thermal velocity of the electrons. In the F layer, the average electron temperature is ~10^3 K and the thermal velocity is $\mathrm{v}_{th}\sim 10^5$ m/s. The pressure term can be approximated by setting $\partial^2 J(z,t)/\partial z^2\sim(\omega_m/c)^2 J(z,t)$. Since $\mathrm{v}_{th}<<c$ and $(\mathrm{v}_{th}/c)\omega_m<<\omega_p$, the pressure term in Eq. (4.5a) can be neglected. The electron collision frequency, $\Gamma<<\omega_p$, plays an important role in limiting the growth of the induced driving current. The maximum amplitude of $J(z,t)$ is far below the value required to be in the linear regime and is far below the value where the perturbed density, $n(z,t)$, becomes comparable to the background density $N_0(z)$.

The electron collision rate in the ionosphere limits the growth of the current density. The collision rate can vary depending on many factors, such as the time of day and solar activity. The typical range of the electron collision rate in the ionosphere is $\Gamma\sim 10-10^3$ Hz [76]. The collision frequency is found by adding the electron-neutral collision frequency to the electron-ion collision frequency. The equation for the electron-neutral collision frequency is $\Gamma_{e-n}[\mathrm{s}^{-1}]=(5.4\times 10^{-10})n_n[\mathrm{cm}^{-3}]T_e^{1/2}[\mathrm{eV}]$, where n_n is the neutral particle density and T_e is the electron temperature [76]. Both of these quantities are functions of the altitude. The electron temperature in the ionosphere is typically on the order of ~10^3 K, though it increases with altitude. The equation for the electron-ion collision frequency is

$\Gamma_{e-i}[\mathrm{s}^{-1}] = \left(34 + 4.18\ln(T_e^3[\mathrm{eV}]/n_e[\mathrm{cm}^{-3}])\right)n_e[\mathrm{cm}^{-3}]T_e^{-3/2}[\mathrm{eV}]$, where n_e is the free electron density [76]. In the ionosphere, these two collision frequencies are comparable.

Using Eqs. (4.5a) - (4.5d), an equation can be found for the variation of the electron charge distribution,

$$\frac{\partial^2\rho(z,t)}{\partial t^2} + \omega_p^2(z)\rho(z,t) + \frac{\partial\ln(\omega_p^2(z))}{\partial z}\left(\frac{\partial}{\partial t} + \Gamma\right)J(z,t) - \Gamma\frac{\partial J(z,t)}{\partial z} = -\varepsilon_0\omega_p^2(z)\frac{\partial E_{NL}(z,t)}{\partial z}, \quad (4.7)$$

where $\rho(z,t) = qn(z,t)$.

The current density in Eq. (4.6) can be solved exactly. In the limit that $\Gamma << \omega_p(z)$, the solution is $J(z,t) = -\varepsilon_0\omega_p^2(z)\omega_m E_{pond}\int_0^t G(t-t')\cos(k_m z - \omega_m t')dt'$, where $G(t) = \Theta(t)\exp\left(-\Gamma t/2\right)\sin(\Omega(z)t)/\Omega(z)$ is the Green's function, $\Theta(t)$ is the Heaviside function, and $\Omega(z) = \sqrt{\omega_p^2(z) - \Gamma^2/4}$. Evaluating $J(z,t)$ near resonance, where $\delta\omega = \omega_m - \omega_p << \omega_m$, and keeping terms to lowest order in $\delta\omega$, gives

$$J(z,t) = J_c g(t)\exp(i(k_m z - \omega_m t)) + c.c., \quad (4.8)$$

where

$$J_c = \frac{\varepsilon_0}{2}\frac{\omega_p^2(z)}{\omega_m}E_{pond} = \frac{q}{2mc^2}\frac{\omega_p^2(z)}{\omega^2}I(\rho,z), \quad (4.9a)$$

$$g(t) = -i\frac{\omega_m}{\Gamma - 2i\delta\omega}\left(1 - (1 + i\delta\omega t)\exp(-\Gamma t/2)\right). \quad (4.9b)$$

In the case where the system is very close to resonance, i.e., $\delta\omega << \Gamma$, Eq. (4.8) reduces to $J(z,t) = J_{\max}(1 - \exp(-\Gamma t/2))\sin(k_m z - \omega_m t)$, where $J_{\max} = 2J_c\omega_m/\Gamma$ is the maximum current density. In the absence of collisions, Eq. (4.8) reduces to $J(z,t) = -J_c\omega_m t\sin(k_m z - \omega_m t)$. It should be noted that even at the maximum value of the current density, $J_{\max}$, the system parameters are in the linear regime, i.e., $n << N_0$ and $V << c$.

4.1.2. Generation of the Low Frequency Signal

Using Eq. (4.8), the axial current density in the ionosphere at altitude *z*, which drives the low frequency signal, is given by

$$J(\rho,z,t)=\frac{q}{2mc^2}\frac{\omega_p^2(z)}{\omega^2}I(\rho,z)g(t)\exp(i(k_m z-\omega_m t))+c.c.. \tag{4.10}$$

The corresponding axial component of the vector potential in the radiation zone is

$$\mathrm{A}_z(\mathbf{r},t)=\frac{\mu_0}{4\pi r}\int_{V'}dV'J(\mathbf{r}',t_R(\mathbf{r},\mathbf{r}',t)), \tag{4.11}$$

where $t_R(\mathbf{r},\mathbf{r}',t)=t-r/c+\hat{\mathbf{r}}\cdot\mathbf{r}'/c$ is the retarded time, $r=\sqrt{\rho^2+z^2}$, $\rho=\sqrt{x^2+y^2}$, $\hat{\mathbf{r}}=(x\hat{\mathbf{x}}+y\hat{\mathbf{y}}+z\hat{\mathbf{z}})/r$ is a unit vector from the source origin to the observation point, $\mathbf{r}'=x'\hat{\mathbf{x}}+y'\hat{\mathbf{y}}+z'\hat{\mathbf{z}}$ is the vector from the source origin to points within the source, and $dV'=\rho' d\rho' d\varphi' dz'$. Figure 4.2 shows the interaction volume associated with the driving current. Since the radiation is symmetric about the *z*-axis, we evaluate the vector potential along the x-axis, which is directed towards the ground, as shown in Fig. 4.1. The function $g(t)$ is slowly varying in time compared to $1/\omega_m$, therefore, we can replace $g(t_R)$ with $g(t-x/c)$. Along the *x*-axis, i.e., where $r=x$, the retarded time is $t_R(x,\mathbf{r}',t)=t-x/c+(\rho'/c)\cos\varphi'$, since $\hat{\mathbf{r}}\cdot\mathbf{r}'=x'=\rho'\cos\varphi'$.

Substituting Eq. (4.10) into Eq. (4.11), the axial vector potential along the *x*-axis is given by

$$\mathrm{A}_z(x,y=0,z=0,t)=\frac{q\mu_0}{8\pi mc^2}\frac{I(0,0)}{x}g(t-x/c)\exp(-i\omega_m(t-x/c))$$
$$\times\int_{z_p-\delta z/2}^{z_p+\delta z/2}dz'\frac{\omega_p^2(z')}{\omega^2}\frac{R_S^2(0)}{R_S^2(z')}\exp(ik_m z')\int_0^\infty \rho' d\rho' \exp\left(-\frac{2\rho'^2}{R_S^2(z')}\right)\int_0^{2\pi}d\varphi'\exp\left(-i\frac{\omega_m\rho'}{c}\cos\varphi'\right)+c.c. \quad , (4.12)$$

where z_{res} is the altitude at which the modulation frequency is resonant with the plasma frequency, i.e., $\omega_m=\omega_p(z_{res})$, and δz is the interaction length over which the resonance occurs, see Fig. 4.2. Evaluating the φ' and ρ' integrals in Eq. (4.12), the vector potential along the *x*-axis is

$$\mathrm{A}_z(x,0,0,t)=\frac{q\mu_0}{8\pi mc^2\omega^2}\tilde{Z}\frac{P_0(0)}{x}g(t-x/c)\exp(-i\omega_m(t-x/c))+c.c., \tag{4.13}$$

where $\tilde{Z}=\int_{z_{res}-\delta z/2}^{z_{res}+\delta z/2}dz'\omega_p^2(z')\exp(-(1/8)(\omega_m R_s(z')/c)^2)\exp(ik_m z')$ and $P_0(0)=\pi I(0,0)R_S^2(0)/2$ is the power. The integral $\tilde{Z}$ can be approximated assuming ω_p and R_S are constant within the interaction length, which gives $\tilde{Z}\approx 2c\omega_m\exp(-(1/8)(\omega_m R_S(z_{res})/c)^2)\sin(k_m\delta z/2)\exp(ik_m z_{res})$. The axial vector potential along the *x*-axis becomes

$$\mathrm{A}_z(x,0,0,t)=A_{RF}(x,\omega_m,\omega)g(t-x/c)\exp(-i\omega_m(t-x/c-z_{res}/c))+c.c., \tag{4.14}$$

where

$$A_{RF}(x,\omega_m,\omega)=\frac{q\mu_0}{4\pi mc\omega_m}\frac{P_0(0)}{x}\frac{\omega_m^2}{\omega^2}\sin\left(\frac{\omega_m\delta z}{2c}\right)\exp\left(-(1/8)\left(\omega_m R_S(z_{res})/c\right)^2\right). \tag{4.15}$$

The Poynting vector, $\mathbf{S}=\mathbf{E}\times\mathbf{B}/\mu_0$, in the radiation zone is $\mathbf{S}=(1/Z_0)\left|\hat{\mathbf{r}}\times\partial\mathbf{A}(\mathbf{r},t)/\partial t\right|^2\hat{\mathbf{r}}$. The low frequency signal intensity as a function of propagation distance along the *x*-axis, i.e., the Poynting flux in the *x*-direction, is

$$I_{RF}(L_x)=2C_0\left|g(t-L_X/c)\right|^2\frac{P_0^2(0)}{L_x^2}\left(\frac{\omega_m}{\omega}\right)^4\exp(-D_S(z_{res})), \tag{4.16}$$

where L_X is the distance from the source in the ionosphere to the observation point on the ground along the *x*-axis as shown in Fig. 4.1, $C_0 = (q\mu_0 / 4\pi mc)^2 / 2Z_0 = 7.6\times10^{-12}\ \mathrm{s^3/(kg\text{-}m^2)}$, and we have set the factor $\sin^2(\omega_m \delta z / 2c) = 1/2$. The exponent in Eq. (4.16), $D_S(z_{res}) = (\omega_m R_S(z_{res}) / 2c)^2$, plays an important role in determining the intensity of the low frequency signal on the ground.

4.2. Evaluation of Low Frequency Signal

In this section, we evaluate the low frequency RF intensity on the ground given by Eq. (4.16). The factor $(\omega_m / \omega)^4$ in Eq. (4.16) indicates that the intensity on the ground, $I_{RF}(L_X)$, is a rather sensitive function of the ground-based source frequency ω. On the other hand, the exponential factor $\exp\left(-D_S(z_{res})\right)$ in Eq. (4.16) is a sensitive function of the spot-size of the driving source in the ionosphere. This would imply that a high frequency source, which would reduce the spot size $R_S(z_p)$, would be beneficial. These factors tend to compete with each other. The quantity $(\omega_m / \omega)^4 \exp(-D_S(z_{res}))$ has a maximum value when the frequency ratio is $\omega_m / \omega = \sqrt{2} R_S(0) / z$. For the parameters used in the example, the optimum source frequency is 160 GHz. In the example, we use a W-band, ground-based source operating at 94 GHz and at a power of 1MW. The 94 GHz source is modulated at the low frequency ω_m, corresponding to the local plasma frequency, which in our example is $9\,\mathrm{MHz}$.

The parameters associated with the ionosphere are in Table 4.1 and the parameters associated with the RF source are in Table 4.2. Figure 4.3 shows the intensity of the low-frequency signal, at 9 MHz, as a function of time, at the observation point on the ground, at a distance $L_X = 500\,\mathrm{km}$ from the source. Figure 4.4 shows the intensity of the low-frequency signal 500 km from the source as a function of the frequency difference between the modulation frequency and the plasma frequency.

Altitude of the resonance	$z_{res} = 250$ km
Electron density	$n_e(z_{res}) = 10^{12}\ \text{m}^{-3}$
Plasma freq.	$\omega_p(z_{res}) = 5.64\times10^7$ rad/s, $f_p = 9$ MHz
Plasma wavelength	$\lambda_p = 33$ m
Collision freq.	$\Gamma = 10^2$ Hz

Table 4.1. Ionospheric parameters used in the example.

Source freq.	$f = 94$ GHz
Source wavelength	$\lambda = 3.2\times10^{-3}$ m
Source power	$P = 1$ MW
Modulation freq.	$\omega_m = 5.64\times10^7$ rad/s
Spot size at ground level	$R_S(0) = 10$ m
Rayleigh length	$Z_R(0) = 98$ km
Spot size in the ionosphere	$R_S(z_{res}) = 27$ m
Intensity in the ionosphere	$I(z_{res}) = 8.5\times10^2\ \text{W/m}^2$
Distance from source in the ionosphere to the ground	$L_X = 500$ km

Table 4.2. RF source parameters used in the example.

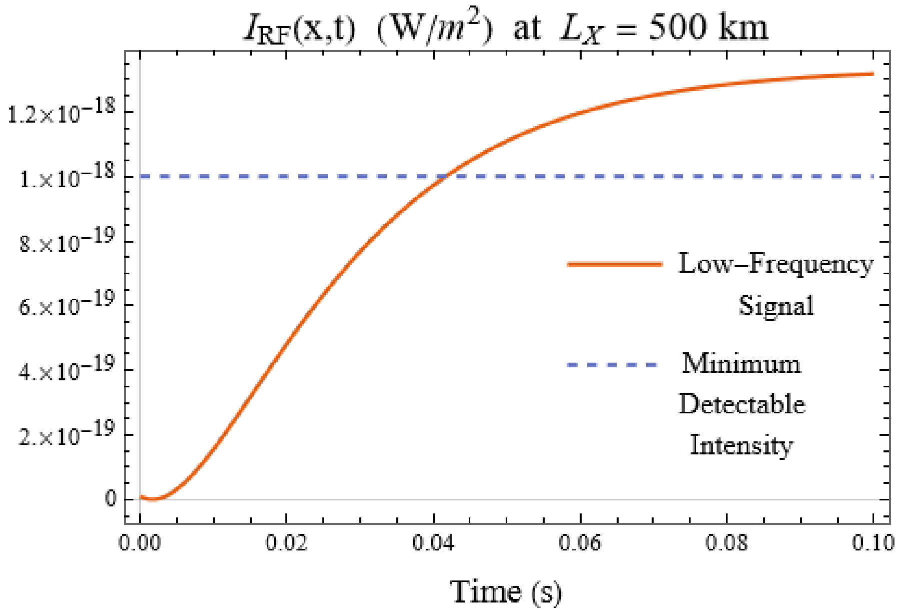

Figure 4.3. Intensity of the low frequency signal as a function of time, 500 km from the source. The minimum detectable intensity is ~ 10^{-18} W/m^2, denoted by the dashed line.

At resonance, i.e., $\omega_m = \omega_p$, the function $g(t - x/c)$ reaches a maximum value of $g_{\max} = \omega_m / \Gamma = 5.64 \times 10^5$ after a time $t \sim 1/\Gamma = 10^{-2}\,\text{s}$. The ground-based source has a carrier frequency of $f = 94\,\text{GHz}$ ($\lambda = 3.2 \times 10^{-3}\,\text{m}$, $\omega = 6.0 \times 10^{11}\,\text{rad/s}$). The spot size of the driving source in the ionosphere is $R_S(z_{res}) = \lambda z_{res} / \pi R_S(0) \approx 27\,\text{m}$. The low frequency intensity on the ground, Eq. (4.24), is $I_{RF}(L_X = 500\text{km}) = 9.6 \times 10^{-16} \exp(-D_S(z_p))\,\text{W/m}^2$, where $\exp(-D_S) = 1.4 \times 10^{-3}$. The value of $I_{RF} \approx 1.3 \times 10^{-18}$ W/m^2 is higher than needed for detection. The rate of photons per second per unit area is $R_{photon}[\text{photons/s} \cdot \text{m}^2] = I[\text{W/m}^2] / \hbar\omega[\text{J}] \sim 10^9\ \text{photons/s} \cdot \text{m}^2$ for the intensity and frequency of our signal.

4.3. Discussion

In this Chapter, I proposed a concept based on a ground-based, mobile, modulated RF source, which generates signals in the ionosphere at frequencies in the MHz range which propagate

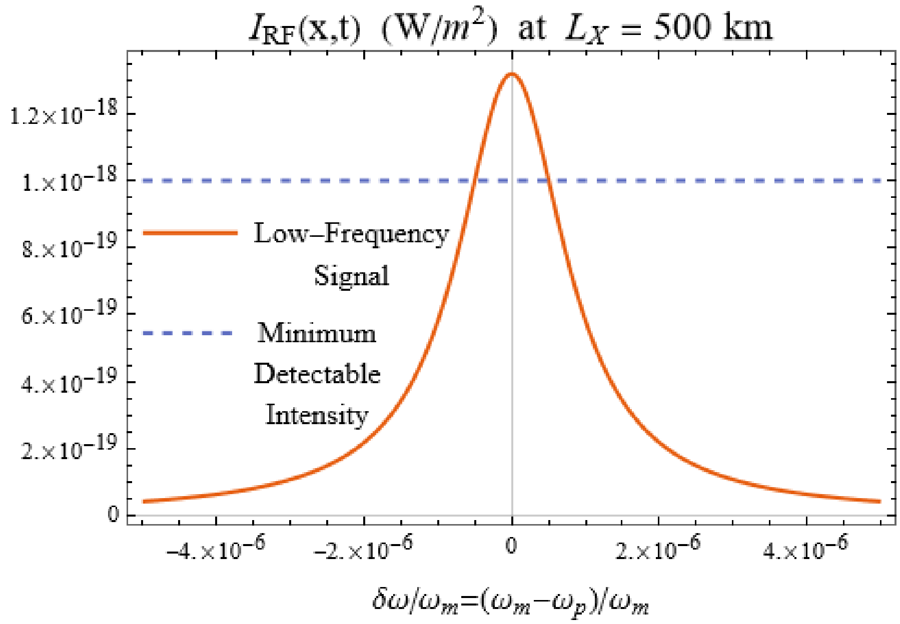

Figure 4.4. Intensity of the low-frequency signal 500 km from the source as a function of the frequency difference between the modulation frequency and the plasma frequency. The minimum detectable intensity is ~ 10^{-18} W/m^2, denoted by the dashed line.

to the observation point on the ground. This concept can be used for an OTH radar or ionospheric monitoring system. The low frequency signal is parametrically generated by the ground-based, modulated, high frequency RF source. A preliminary comparison of sources for this application indicates that sources in the W-band, e.g., 94 GHz, can achieve the intensity level needed for detection of the low frequency signal. Sources at 94 GHz have low atmospheric absorption coefficients and are used in high power radar systems. These sources are based on Gyrotron technology and are commercially available at power levels in the MW regime [88]. On the other hand, a ground-based source in the Ka-band, i.e., 34 GHz, would require a very large ground antenna dish to produce a reasonably small spot size $R_S(z_{res})$ in the ionosphere. It does not appear that a 34 GHz source is feasible for this application. The use of lasers for the ground-based source also does not appear to be feasible. If a modulated CO_2 laser were used, the factor $(\omega_m/\omega)^4 = 8\times10^{-27}$ would result in values of I_{RF} that would be too low for detection.

The RF source used in our example is a modulated 94 GHz source. The low frequency signal intensity at the observation point, 500 km from the ground source, is higher than the minimum detectable intensity level. The rate of photons per second per unit area for the intensity and frequency in the example is $R_{photon} \sim 10^9$ photons/s$\cdot$m^2. The minimum detectable intensity in the 3 MHz – 30 MHz frequency regime is estimated to be $\sim 10^{-18}$ W/m^2; however, the theoretical limit on the minimum intensity level is significantly lower.

If the low frequency signal returns to ground level over seawater, the signal can propagate back to the detector by means of surface waves. Low frequency surface waves can propagate extremely long distances along the surface of seawater. The surface waves are evanescent waves having an e-folding (decay) length that can be extremely long. For frequencies in the low MHz range, the surface wave can propagate distances > 500 km over seawater. The proposed mechanism may have applications for compact, mobile, and low cost OTH radar systems and/or as a method to monitor ionospheric parameters.

Chapter 5: Discussion

In this dissertation, I presented three research projects dealing with laser interactions in the atmosphere. These projects are presented in chapters 2, 3, and 4. In Chapter 2, I presented a mechanism for remotely generating tunable RF signals in the GPS frequency regime (~1.6 GHz) [1]. The laser pulse train (LPT) ionizes the air through photo detachment and collisional ionization, generating a plasma filament. The ponderomotive forces of the LPT drive radial and longitudinal plasma currents. These currents generate radiation at the LPT repetition rate, which can be tuned in the 0.5 – 6.0 GHz range. Of particular interest is the RF generation in the 1.4-1.7 GHz regime which is the operating range of all GPS signals. The analysis and simulation results of the RF radiation are shown to be in agreement with experimental data [2]. The experiments were performed in collaboration with the theory and computational work at the University of Maryland.

Chapter 3 presents the analysis and simulations of laser pulses propagating long distances (>50 km) vertically in the atmosphere. In addition, the hybrid modulation-filamentation instability that causes transverse and longitudinal beam breakup is analyzed and simulated [3]. By tailoring the initial laser pulse parameters, i.e., the wavefront curvature, chirp, and power, the pulse can be focused transversely and longitudinally at remote locations (>50 km) with intensity enhancements of $> 10^3$. Nonlinear self-focusing of the laser pulse and dispersion lead to the growth of a hybrid modulation-filamentation instability, which causes both transverse and longitudinal beam breakup. This hybrid instability is analyzed and numerically simulated for pulses propagating in the atmosphere. The potential application of this research is on the long-range generation of RF signals in a turbulent atmosphere.

In the Chapter 4, I presented a mechanism for generating low frequency signals (3-30 MHz) in the ionosphere and propagating them back to the ground for use as a low-cost, mobile over-the-horizon (OTH) radar system [4]. Conventional OTH radar systems utilize dipole antenna arrays that span multiple kilometers, and can cost ~1 billion dollars. Many major countries employ conventional OTH radar systems, e.g., the USA, Russia, China, UK, Brazil, Canada, Australia, India, and France. The proposed mechanism relies on a ground-based, modulated RF source. By tuning the modulation frequency to the local plasma frequency in the ionosphere (F layer), a current can be resonantly excited by the ponderomotive force of the modulated signal. This current grows in time and generates a low frequency signal at the local plasma frequency, which is in the MHz range. The low frequency signal propagates back to the ground, far from the source, where it can be detected. For a 94 GHz source modulated at 9 MHz and operating at 1 MW, a low frequency signal can be generated above the minimum detectable intensity (~10^{-18} W/m^2). The rate of photons per second per unit area for the intensity and frequency of our signal is $R_{photon} \sim 10^9$ photons/s$\cdot$m^2. This mechanism has the potential to detect OTH objects using a compact, mobile, and far less expensive system than presently exists.

5.1. Future Plans

For the project in Chapter 2, we are continuing to receive new experimental data from our collaborator, Dr. Vladimir Markov, at Advanced Systems and Technologies, Inc. There are always new questions to answer with new experimental results. Currently, we are working on improving our model to explain the directionality of the RF radiation produced in the experiments. The experimental data shows RF being emitted transverse to the direction of propagation of the LPT, while our model and simulations show the RF radiation being emitted in a direction that is angled forward of the transverse plane. This is consistent with the idea that collisions are important for the longitudinal ponderomotive force. If the longitudinal force is dominant, then the RF radiation will be directed transverse to the direction of propagation of the LPT, in agreement with experimental data.

The long-range propagation model presented in Chapter 3 can be used in tandem with the mechanism for generating RF radiation in Chapter 2. This can be accomplished by propagating a high-intensity pulse in such a way that it focuses and ionizes the air in front of a target before the low-intensity LPT arrives. This pre-ionizing pulse would ionize the air primarily through multiphoton/tunneling ionization, providing seed electrons for the LPT. The LPT would continue to build the plasma density through collisional ionization. By utilizing a high-intensity pre-ionizing pulse, this mechanism could be effective for electronic countermeasure applications.

Appendices

Appendix A: Ponderomotive Force

In this Appendix, I present a derivation of the ponderomotive force, including the longitudinal term due to collisions. Expanding the Lorenz force equation to second order in the field amplitudes gives

$$\mathbf{F}_{pond}(\mathbf{r},t) = q\left((\mathbf{r}_1(\mathbf{r},t)\cdot\nabla)\mathbf{E}(\mathbf{r},t) + \mathbf{v}_1(\mathbf{r},t)\times\mathbf{B}(\mathbf{r},t)\right), \tag{A1}$$

where $\mathbf{r}_1$ and $\mathbf{v}_1$ are the position and velocity to first order in the field amplitudes, $\mathbf{E}(\mathbf{r},t) = \hat{\mathbf{E}}(\mathbf{r},t)\exp(-i\omega t) + c.c.$ is the laser electric field, and $\mathbf{B}(\mathbf{r},t) = \hat{\mathbf{B}}(\mathbf{r},t)\exp(-i\omega t) + c.c.$ is the laser magnetic field. The position and velocity vectors are related by $\mathbf{v}_1(\mathbf{r},t) = \partial\mathbf{r}_1(\mathbf{r},t)/\partial t$.

Defining $\mathbf{r}_1(\mathbf{r},t) = \hat{\mathbf{r}}_1(\mathbf{r},t)\exp(-i\omega t) + c.c.$ and $\mathbf{v}_1(\mathbf{r},t) = \hat{\mathbf{v}}_1(\mathbf{r},t)\exp(-i\omega t) + c.c.$, we can solve for the amplitudes $\hat{\mathbf{r}}_1$ and $\hat{\mathbf{v}}_1$ using the fluid equations

$$\frac{\partial\mathbf{v}_1(\mathbf{r},t)}{\partial t} + \Gamma\mathbf{v}_1(\mathbf{r},t) = \frac{q}{m}\mathbf{E}(\mathbf{r},t), \tag{A2}$$

where Γ is the electron collision frequency. Solving for the position and velocity Fourier amplitudes as functions of the electric field amplitude gives

$$\hat{\mathbf{v}}_1(\mathbf{r},t) = i\frac{q}{m}\frac{\hat{\mathbf{E}}(\mathbf{r},t)}{\omega(1+i\Gamma/\omega)}, \tag{A3a}$$

$$\hat{\mathbf{r}}_1(\mathbf{r},t) = -\frac{q}{m}\frac{\hat{\mathbf{E}}(\mathbf{r},t)}{\omega^2(1+i\Gamma/\omega)}. \tag{A3b}$$

The ponderomotive force consists of a DC term which is slowly varying in time, and a term that oscillates at twice the laser frequency. Keeping only the DC term, the ponderomotive force is

$$\mathbf{F}_{pond,DC}(\mathbf{r},t) = q\left((\hat{\mathbf{r}}_1\cdot\nabla)\hat{\mathbf{E}}^* + \hat{\mathbf{v}}_1\times\hat{\mathbf{B}}^* + c.c.\right). \tag{A4}$$

Inserting Eqs. (A3a) and (A3b) into Eq. (A4) gives

$$\mathbf{F}_{pond,DC}(\mathbf{r},t) = -\frac{q^2}{m(\omega^2+\Gamma^2)}\Big(((\hat{\mathbf{E}}\cdot\nabla)\hat{\mathbf{E}}^* + \hat{\mathbf{E}}\times(\nabla\times\hat{\mathbf{E}}^*))(1-i\Gamma/\omega) + c.c.\Big). \tag{A5}$$

Using the identity $(\hat{\mathbf{E}}\cdot\nabla)\hat{\mathbf{E}}^* + \hat{\mathbf{E}}\times(\nabla\times\hat{\mathbf{E}}^*) + c.c. = \nabla(\hat{\mathbf{E}}\cdot\hat{\mathbf{E}}^*)$, Eq. (A5) becomes

$$\mathbf{F}_{pond,DC}(\mathbf{r},t) = -\frac{q^2}{m(\omega^2+\Gamma^2)}\left(\nabla(\hat{\mathbf{E}}\cdot\hat{\mathbf{E}}^*) + 2\frac{\Gamma}{\omega}\mathrm{Im}\Big[(\hat{\mathbf{E}}\cdot\nabla)\hat{\mathbf{E}}^* + \hat{\mathbf{E}}\times(\nabla\times\hat{\mathbf{E}}^*)\Big]\right). \tag{A6}$$

Equation (A6) can be simplified using $\mathrm{Im}\Big[(\hat{\mathbf{E}}\cdot\nabla)\hat{\mathbf{E}}^* + \hat{\mathbf{E}}\times(\nabla\times\hat{\mathbf{E}}^*)\Big] \approx \mathrm{Im}\Big[\hat{E}_x\partial\hat{E}_x^*/\partial z\Big]$, since the transverse electric field dominates the longitudinal field, i.e., $\rho_0 >> \lambda_0$, where ρ_0 is the laser spot size and λ_0 is the wavelength of the laser, for the parameters under consideration. Using this expression, Eq. (A6) becomes

$$\mathbf{F}_{pond,DC} = -\frac{q^2}{m(\omega^2+\Gamma^2)}\left(\nabla\left|\hat{E}\right|^2 - 2\frac{\Gamma}{c}\left|\hat{E}\right|^2\hat{\mathbf{z}}\right). \tag{A7}$$

In the absence of collisions, i.e., $\Gamma = 0$, Eq. (A7) reduces to Eq. (2.3). This derivation is valid under the assumption that the longitudinal laser electric field is small compared to the transverse field, i.e., $E_x >> E_z$, which is true for the parameters considered here.

Appendix B: Dispersion Coefficients

In this Appendix, I present a detailed derivation of the dispersion coefficients. The dispersion coefficients are the coefficients of the time derivative terms for the wave equation. In this appendix, the dispersion coefficients will be derived up to third order. Beginning with the wave equation,

$$\left(\nabla_\perp^2 + \frac{\partial^2}{\partial z^2} - \frac{1}{c^2}\frac{\partial^2}{\partial t^2}\right)E(\mathbf{r}_\perp,z,t) = \mu_0\frac{\partial^2}{\partial t^2}P(\mathbf{r}_\perp,z,t), \tag{B1}$$

where $\nabla_\perp^2 = \partial^2/\partial x^2 + \partial^2/\partial y^2$, $E(\mathbf{r}_\perp, z, t)$ is the electric field, and $P(\mathbf{r}_\perp, z, t)$ is the polarization field. The polarization field can be written as a linear response function to the electric field $P(\mathbf{r}_\perp, z, t) = \int_{-\infty}^{t} dt' \chi(t-t') E(\mathbf{r}_\perp, z, t') = \int_0^\infty dt' \chi(t') E(\mathbf{r}_\perp, z, t-t')$, and the Fourier transform is given by $P(\mathbf{r}_\perp, z, \omega) = \hat{\chi}(\omega)\hat{E}(\mathbf{r}_\perp, z, \omega)$. We define our Fourier transform as $F(t) = \frac{1}{2\pi}\int_{-\infty}^{\infty} d\omega \hat{F}(\omega)\exp(-i\omega t)$ and the inverse transform as $\hat{F}(\omega) = \int_{-\infty}^{\infty} dt F(t)\exp(i\omega t)$. The fields are represented as $E(\mathbf{r}_\perp, z, t) = 1/2 E_0(\mathbf{r}_\perp, z, t)\exp(i(k_0 z - \omega_0 t)) + c.c.$ and $P(\mathbf{r}_\perp, z, t) = 1/2 P_0(\mathbf{r}_\perp, z, t)\exp(i(k_0 z - \omega_0 t)) + c.c.$, where k_0 is the wavenumber and ω_0 is the frequency of the light. Therefore, the polarization field amplitude is $P_0(\mathbf{r}_\perp, z, t) = \int_0^\infty dt' \chi(t') \exp(i\omega_0 t') E_0(\mathbf{r}_\perp, z, t-t')$.

Using these representations for the fields, the wave equation becomes

$$\begin{aligned}&\left(\nabla_\perp^2 + \frac{\partial^2}{\partial z^2} + \frac{\omega_0^2}{c^2} - k_0^2 + 2ik_0\frac{\partial}{\partial z} + 2i\frac{\omega_0}{c^2}\frac{\partial}{\partial t} - \frac{1}{c^2}\frac{\partial^2}{\partial t^2}\right)E_0(\mathbf{r}_\perp, z, t) \\ &\qquad = -\mu_0\omega_0^2\left(1 + \frac{i}{\omega_0}\frac{\partial}{\partial t}\right)^2 P_0(\mathbf{r}_\perp, z, t)\end{aligned} \quad . \tag{B2}$$

Now, we perform a change of variables into the laser pulse frame. That is, $\tau = t - z/\mathrm{v}_t$, $\eta = z$, $\partial/\partial t = \partial/\partial\tau$, and $\partial/\partial z = \partial/\partial\eta - \mathrm{v}_t^{-1}\partial/\partial\tau$, where v_t is the transformation velocity. Setting this velocity equal to the group velocity will greatly simplify the wave equation. The wave equation under this transformation becomes

$$\left(\begin{array}{l}\nabla_\perp^2 + \dfrac{\partial^2}{\partial\eta^2} + \dfrac{1}{\mathrm{v}_t^2}\left(1 - \dfrac{\mathrm{v}_t^2}{c^2}\right)\dfrac{\partial^2}{\partial\tau^2} + \dfrac{\omega_0^2}{c^2} - k_0^2 \\ +2ik_0\left(1 + \dfrac{i}{k_0\mathrm{v}_t}\dfrac{\partial}{\partial\tau}\right)\dfrac{\partial}{\partial\eta} + 2i\dfrac{\omega_0}{c^2}\left(1 - \dfrac{c^2 k_0}{\omega_0\mathrm{v}_t}\right)\dfrac{\partial}{\partial\tau}\end{array}\right)E_0(\mathbf{r}_\perp, z, t) = -\mu_0\omega_0^2\left(1 + \frac{i}{\omega_0}\frac{\partial}{\partial\tau}\right)^2 P_0(\mathbf{r}_\perp, z, t)\,. \tag{B3}$$

The polarization field becomes $P_0(\mathbf{r}_\perp,\eta,\tau)=\int_0^\infty d\tau'\chi(\tau')\exp(i\omega_0\tau')E_0(\mathbf{r}_\perp,\eta,\tau-\tau')$.

In order to evaluate the polarization field, we must expand $E_0(\mathbf{r}_\perp,\eta,\tau-\tau')$ about τ. This is useful in the limit that the pulse length is much greater than the wavelength, i.e., $T(z)\gg\lambda_0/c$. Expanding the electric field gives

$$E_0(\tau-\tau')=E_0(\tau)-\tau'\frac{\partial}{\partial\tau}E_0(\tau)+\frac{\tau'^2}{2}\frac{\partial^2}{\partial\tau^2}E_0(\tau)-\frac{\tau'^3}{6}\frac{\partial^3}{\partial\tau^3}E_0(\tau)+\dots \quad \text{(B4)}$$

The polarization field is then

$$P_0(\mathbf{r}_\perp,\eta,\tau)=\left(\hat{\chi}(\omega_0)+i\frac{\partial\hat{\chi}(\omega_0)}{\partial\omega_0}\frac{\partial}{\partial\tau}-\frac{1}{2}\frac{\partial^2\hat{\chi}(\omega_0)}{\partial\omega_0^2}\frac{\partial^2}{\partial\tau^2}-\frac{i}{6}\frac{\partial^3\hat{\chi}(\omega_0)}{\partial\omega_0^3}\frac{\partial^3}{\partial\tau^3}+\dots\right)E_0(\mathbf{r}_\perp,\eta,\tau), \quad \text{(B5)}$$

where $\hat{\chi}(\omega_0)$ is the electric susceptibility, which defines the linear refractive index as $n_L(\omega_0)=\left(1+\hat{\chi}(\omega_0)/\varepsilon_0\right)^{1/2}$. By combining Eqs. (B3) and (B5) and grouping terms by order in the time derivatives, the wave equation is

$$\left(\nabla_\perp^2+\frac{\partial^2}{\partial\eta^2}+\frac{\omega_0^2}{c^2}-k_0^2+2ik_0\left(1+\frac{i}{k_0\mathrm{v}_g}\frac{\partial}{\partial\tau}\right)\frac{\partial}{\partial\eta}+Q_2\frac{\partial^2}{\partial\tau^2}+Q_3\frac{\partial^3}{\partial\tau^3}\right)E_0(\mathbf{r}_\perp,z,t)=0, \quad \text{(B6)}$$

where

$$Q_2=\frac{1}{\mathrm{v}_t^2}-\frac{1}{c^2}-\mu_0\hat{\chi}(\omega_0)-2\mu_0\omega_0\frac{\partial\hat{\chi}(\omega_0)}{\partial\omega_0}-\frac{\mu_0\omega_0^2}{2}\frac{\partial^2\hat{\chi}(\omega_0)}{\partial\omega_0^2}=-\beta_0\beta_2 \quad \text{(B7a)}$$

$$Q_3=-i\mu_0\left(\frac{\partial\hat{\chi}(\omega_0)}{\partial\omega_0}+\omega_0\frac{\partial^2\hat{\chi}(\omega_0)}{\partial\omega_0^2}+\frac{\omega_0^2}{6}\frac{\partial^3\hat{\chi}(\omega_0)}{\partial\omega_0^3}\right)=-i\left(\frac{\beta_0\beta_3}{3}+\beta_1\beta_2\right). \quad \text{(B7b)}$$

In this equation we have taken $\mathrm{v}_t\equiv\mathrm{v}_g$, where the group velocity is

$$\mathrm{v}_g=\frac{n_L(\omega_0)c}{1+\frac{\hat{\chi}(\omega_0)}{\varepsilon_0}+\frac{\omega_0}{2\varepsilon_0}\frac{\partial\hat{\chi}(\omega_0)}{\partial\omega_0}}=c\left(\frac{\partial(\omega_0 n_L(\omega_0))}{\partial\omega_0}\right)^{-1}=\frac{1}{\beta_1}, \quad \text{(B8)}$$

where $\beta_l = \frac{\partial^l}{\partial \omega_0^l}\left(\frac{\omega_0 n_L(\omega_0)}{c}\right)$.

Typical values for the group velocity dispersion parameters at approximately $\lambda = 1\ \mu$m are $\approx 20\ \text{fs}^2/\text{m}$ for second order dispersion and $\approx 10\ \text{fs}^3/\text{m}$ for third order dispersion in air. It is conventional to include the effects of third order dispersion for pulse lengths <30 fs when there is no chirp [71].

Appendix C: Simulation Coefficients for the Hybrid Instability

In this appendix we derive the equations that are used in the simulation code. Substituting the representations in Eqs. (3.33a) and (3.33b) into Eqs. (3.24a) and (3.24b) gives

$$\begin{aligned}\frac{\partial a_R}{\partial z} = \sum_{n,l,s} \Big[& \frac{1}{2k_0}\left(k_n^2 + k_l^2 - k_0\beta_{GVD}\omega_s^2\right)b_{n,l,s} + 2i\frac{k_n}{k_0 R^2}\left(b_{n,l,s} + \alpha a_{n,l,s}\right)x \\ & + 2i\frac{k_l}{k_0 R^2}\left(b_{n,l,s} + \alpha a_{n,l,s}\right)y + 2i\frac{\beta_{GVD}\omega_s}{T^2}\left(b_{n,l,s} + \beta a_{n,l,s}\right)\tau \ \Big]\exp(i\psi_{n,l,s}(x,y,\tau))\end{aligned}, \tag{C1a}$$

$$\begin{aligned}\frac{\partial a_I}{\partial z} = \sum_{m,n,s} \Big[& -\frac{1}{2k_0}\left(k_n^2 + k_l^2 - \beta_{GVD}k_0\omega_s^2\right)a_{n,l,s} - \frac{2ik_n}{k_0 R^2}\left(a_{n,l,s} - \alpha b_{n,l,s}\right)x \\ & - \frac{2ik_l}{k_0 R^2}\left(a_{n,l,s} - \alpha b_{n,l,s}\right)y - \frac{2i\beta_{GVD}\omega_s}{T^2}\left(a_{n,l,s} - \beta b_{n,l,s}\right)\tau \\ & + \frac{2}{k_0 R_0^2}\frac{P_0}{P_{NL}}\left(\frac{E}{E_0}\right)^2 \exp\left(-2\frac{x^2}{R^2}\right)\exp\left(-2\frac{\tau^2}{T^2}\right)a_{n,l,s} \ \Big]\exp(i\psi_{n,l,s}(x,y,\tau))\end{aligned}. \tag{C1b}$$

Multiplying Eqs. (C1a) and (C1b) by $\exp(-i\psi_{m,j,q}(x,y,\tau))$ and integrating over x, y and τ, i.e., $(8N^3R^2T)^{-1}\int_{-NR}^{NR} dx \int_{-NR}^{NR} dy \int_{-NT}^{NT} d\tau$, gives

$$\frac{\partial a_{m,j,q}}{\partial z} = \sum_{n,l,s} KA_{m,n,j,l,q,s}a_{n,l,s} + KB_{m,n,j,l,q,s}b_{n,l,s}, \tag{C2a}$$

$$\frac{\partial b_{m,j,q}}{\partial z} = \sum_{n,l,s} -\left(KB_{m,n,j,l,q,s} - \frac{2}{k_0 R_0^2}\frac{P_0}{P_{NL}}\left(\frac{E}{E_0}\right)^2 H_{n,m}H_{l,j}F_{s,q}\right)a_{n,l,s} + KA_{m,n,j,l,q,s}b_{n,l,s}, \tag{C2b}$$

where the coefficients are given by

$$KA_{m,n,j,l,q,s} = \frac{2i\alpha}{k_0 R^2}\left(k_n G_{n,m}\delta_{l,j}\delta_{s,q} + k_l \delta_{n,m} G_{l,j}\delta_{s,q}\right) + \frac{2i\beta_{GVD}\omega_s}{T^2}\beta\delta_{n,m}\delta_{l,j}J_{s,q}$$
$$-i\sum_{n,l,s}\left(\frac{\partial k_m}{\partial z}G_{n,m}\delta_{l,j}\delta_{s,q} + \frac{\partial k_l}{\partial z}\delta_{n,m}G_{l,j}\delta_{s,q} - \frac{\partial \omega_q}{\partial z}\delta_{n,m}\delta_{l,j}J_{s,q}\right), \tag{C3a}$$

$$KB_{m,n,j,l,q,s} = \frac{(k_n^2 + k_l^2 - \beta_{GVD}k_0\omega_s^2)}{2k_0}\delta_{n,m}\delta_{l,j}\delta_{s,q} + \frac{2i}{k_0 R^2}\left(k_n G_{n,m}\delta_{l,j}\delta_{s,q} + k_l\delta_{n,m}G_{l,j}\delta_{s,q}\right)$$
$$+\frac{2i\beta_{GVD}\omega_s}{T^2}\delta_{n,m}\delta_{l,j}J_{s,q}. \tag{C3b}$$

The coefficients used in Eqs. (C2) and (C3) are listed below

$$\delta_{n,m} = \frac{1}{2NR}\int_{-NR}^{NR}\exp(i(k_n - k_m)x)dx, \tag{C4}$$

$$G_{n,m}(z) = \frac{1}{2NR}\int_{-NR}^{NR} x\exp(i(k_n - k_m)x)dx, \tag{C5}$$

$$G_{n,m}(z) = -\frac{i}{k_n - k_m}, \text{ for } n \neq m \quad \text{and} \quad G_{n,n}(z) = 0 \text{ for } n = m, \tag{C6}$$

$$H_{n,m}(z) = \frac{1}{2NR}\int_{-NR}^{NR}\exp(-2x^2/R^2)\exp(i(k_n - k_m)x)dx, \tag{C7}$$

$$H_{n,m}(z) = \frac{1}{4N}\sqrt{\frac{\pi}{2}}\exp\left(-\frac{(n-m)^2\pi^2}{2N^2}\right)\left(\mathrm{Erf}\left(\frac{2N^2 - i(m-n)\pi}{\sqrt{2}N}\right) + \mathrm{Erf}\left(\frac{2N^2 + i(m-n)\pi}{\sqrt{2}N}\right)\right), \tag{C8}$$

$$\delta_{s,q} = \frac{1}{2NT}\int_{-NT}^{NT}\exp(-i(\omega_s - \omega_q)\tau)d\tau, \tag{C9}$$

$$J_{s,q}(z) = \frac{1}{2NT}\int_{-NT}^{NT}\tau\exp(-i(\omega_s - \omega_q)\tau)d\tau, \tag{C10}$$

$$J_{s,q}(z) = \frac{i}{\omega_s - \omega_q}, \text{ for } s \neq q \quad \text{and} \quad J_{s,s}(z) = 0 \text{ for } s = q, \tag{C11}$$

$$F_{s,q}(z)=\frac{1}{2NT}\int_{-NT}^{NT}\exp(-2\tau^2/T^2)\exp(-i(\omega_s-\omega_q)\tau)d\tau\,, \tag{C12}$$

$$F_{s,q}(z)=\frac{1}{4N}\sqrt{\frac{\pi}{2}}\exp\left(-\frac{(s-q)^2\pi^2}{2N^2}\right)\left(\mathrm{Erf}\left(\frac{2N^2-i(q-s)\pi}{\sqrt{2}N}\right)+\mathrm{Erf}\left(\frac{2N^2+i(q-s)\pi}{\sqrt{2}N}\right)\right). \tag{C13}$$

Appendix D: Nonlinear Fluid Formulation

In this Appendix, I present a derivation of the nonlinear fluid equations. Equations (4.4a) - (4.4d) are written in the field variables, i.e., z and t. We now convert them to fluid variables z_0 and τ. The transformation is $z=z_0+\int_0^\tau V_e(z_0,\tau')d\tau'$ and $t=\tau$, where $V_e(z_0,\tau)$ is the velocity of the fluid element which started at z_0 as a function of time τ. The transformation rules for the derivatives are $\partial/\partial\tau=\partial/\partial t+V_e(z_0,\tau)\partial/\partial z$ and $\partial/\partial z_0=\left(1+\int_0^\tau\partial V_e(z_0,\tau')/\partial z_0 d\tau'\right)\partial/\partial z$.

Applying these transformation rules to Eqs. (4.4a) - (4.4d) gives

$$\frac{\partial V_e(z_0,\tau)}{\partial\tau}=\frac{q}{m}\left(E(z_0,\tau)+E_{NL}(z_0,\tau)\right), \tag{D1a}$$

$$\frac{\partial E(z_0,\tau)}{\partial\tau}-\frac{V_e(z_0,\tau)}{1+\int_0^\tau\frac{\partial V_e(z_0,\tau')}{\partial z_0}d\tau'}\frac{\partial E(z_0,\tau)}{\partial z_0}=-\frac{q}{\varepsilon_0}N_e(z_0,\tau)V_e(z_0,\tau), \tag{D1b}$$

$$\frac{\partial N_e(z_0,\tau)}{\partial\tau}+\frac{N_e(z_0,\tau)}{1+\int_0^\tau\frac{\partial V_e(z_0,\tau')}{\partial z_0}d\tau'}\frac{\partial V_e(z_0,\tau)}{\partial z_0}=0, \tag{D1c}$$

$$\frac{1}{1+\int_0^\tau\frac{\partial V_e(z_0,\tau')}{\partial z_0}d\tau'}\frac{\partial E(z_0,\tau)}{\partial z_0}=\frac{q}{\varepsilon_0}\left(N_e(z_0,\tau)-N_0(z_0)\right). \tag{D1d}$$

Combining Eqs. (D1b) and (D1d) gives

$$\frac{\partial E(z_0,\tau)}{\partial\tau}=-\frac{q}{\varepsilon_0}N_0(z_0)V_e(z_0,\tau). \tag{D2}$$

Combining Eq. (D1a) and Eq. (D2) gives

$$\frac{\partial^2 V_e(z_0,\tau)}{\partial \tau^2} + \omega_p^2(z_0) V_e(z_0,\tau) = \frac{q}{m}\frac{\partial E_{NL}(z_0,\tau)}{\partial \tau}, \tag{D3}$$

where $\omega_p^2(z_0) = q^2 N_0(z_0)/m\varepsilon_0$ is the plasma frequency. Introducing the definition $V_e(z_0,\tau) \equiv \partial z_e(z_0,\tau)/\partial\tau$, where $z_e(z_0,0)=0$, yields

$$\frac{\partial^2 z_e(z_0,\tau)}{\partial \tau^2} + \omega_p^2(z_0) z_e(z_0,\tau) = \frac{q}{m} E_{NL}(z_0,\tau), \tag{D4}$$

where $E_{NL}(z_0,\tau) = -i(1/2)E_{pond}\exp(i\Delta kz)\exp\left(i(\Delta k z_e(z_0,\tau)-\Delta\omega\tau)\right)+c.c.$. Inserting the definition for the nonlinear electric field into Eq. (D4) gives

$$\frac{\partial^2 z_e(z_0,\tau)}{\partial \tau^2} + \omega_p^2(z_0) z_e(z_0,\tau) = -i\Delta\omega V_{pond}\exp\left(i(\Delta kz-\Delta\omega\tau)\right)\exp\left(i\Delta k z_e(z_0,\tau)\right)+c.c., \tag{D5}$$

where $V_{pond} = qE_{pond}/2m\Delta\omega$. Equation (D5) describes the full nonlinear plasma dynamics in 1D.

The fluid quantities $E(z_0,\tau)$, $N_e(z_0,\tau)$, and $J_e(z_0,\tau)$ can all be derived in terms of $z_e(z_0,\tau)$. From Eq. (D2), we find

$$E(z_0,\tau) = -\frac{q}{\varepsilon_0} N_0(z_0) z_e(z_0,\tau). \tag{D6}$$

Using Eq. (D1d) with Eq. (D6) gives

$$N_e(z_0,\tau) = \frac{N_0(z_0) - (\partial N_0(z_0)/\partial z_0) z_e(z_0,\tau)}{1+\partial z_e(z_0,\tau)/\partial z_0}. \tag{D7}$$

Using the definition for the electric current density, we find

$$J_e(z_0,\tau) = q\left(\frac{N_0(z_0) - (\partial N_0(z_0)/\partial z_0) z_e(z_0,\tau)}{1+\partial z_e(z_0,\tau)/\partial z_0}\right)\frac{\partial z_e(z_0,\tau)}{\partial \tau}. \tag{D8}$$

The electric current density is necessary for determining the HF signal generated by the interaction of the electric field with the plasma. The current density must be converted back to the field variables in order to find the vector potential of the HF radiation.

Bibliography

[1] G. Blair and P. Sprangle, "Generation of rf radiation by low-intensity laser pulse trains in air," Phys. Rev. E **108**, 015203 (2023).

[2] G. Blair, I. Marienko, V. Markov, and P. Sprangle, "RF radiation generated by laser pulse trains in air," accepted for publication in the Journal of Directed Energy (2025).

[3] G. Blair, B. Hafizi, and P. Sprangle, "Propagation and stability of laser pulses in the atmosphere," Phys. Rev. A **112**, 033502 (2025).

[4] P. Sprangle and G. Blair, "Frequency conversion in the ionosphere for over-the-horizon radar," Phys. Rev. App. **24**, 054040 (2025).

[5] P. Sprangle, J.R. Peñano, & B. Hafizi, "Propagation of intense short laser pulses in the atmosphere," Phys. Rev. E **66**(4), 046418 (2002).

[6] P. Sprangle, J.R. Peñano, B. Hafizi, and C.A. Kapetanakos, "Ultrashort laser pulses and electromagnetic pulse generation in air and on dielectric surfaces," Phys. Rev. E **69**, 066415 (2004).

[7] X. Liu, et al., "Long lifetime air plasma channel generated by femtosecond laser pulse sequence," Opt. Express **20**, 5968 (2012).

[8] S. Eisenmann, J. Peñano, P. Sprangle, and A. Zigler, "Effect of an energy resovior on the atmospheric propagation of laser-plasma filaments," Phys. Rev. Lett. **100**, 155003 (2008).

[9] S. Varma, Y.-H. Chen, and H.M. Milchberg, "Trapping and destruction of long-range high-intensity optical filaments by molecular quantum wakes in air," Phys. Rev. Lett. **101**, 205001 (2008).

[10] A. Ting, I. Alexeev, D. Gordon, E. Briscoe, J. Peñano, R. Fischer, R. Hubbard, P. Sprangle, and G. Rubel, "Remote atmospheric breakdown for standoff detection by using an intense short laser pulse," Appl. Opt. **44**, 5315 (2005).

[11] A.J. Peurrung, "On the long-range detection of radioactivity using electromagnetic radiation," Nuclear Instruments and Methods in Physics Research Section A: Accelerators, Spectrometers, Detectors and Associated Equipment **481**(1), 731 (2002).

[12] Y.E. Geints and A.A. Zemlyanov, "Single and multiple filamentation of multi-terawatt CO_2-laser pulses in air: numerical simulations," J. Opt. Soc. Am. B **31**, 788 (2014).

[13] Y.E. Geints and A.A. Zemlyanov, "Near- and mid-IR ultrashort laser pulse filamentation in a molecular atmosphere: a comparative analysis," Appl. Opt. **56**(5), 1397 (2017).

[14] A. Houard, V. Jukna, G. Point, Y-B. André, S. Klingebiel, M. Schultze, K. Michel, T. Metzger, and A. Mysyrowicz, "Study of filamentation with a high power high repetition rate ps laser at 1.03 µm," Opt. Express **24**, 7437 (2016).

[15] A. Schmitt-Sody, H. Kurz, L. Bergé, S. Skupin, P. Polynkin, "Picosecond laser filamentation in air," New J. Phys. **18**, 093005 (2016).

[16] I. Larkin, J. Griff McMahon, A. Schweinsberg, A. Goffin, A. Valenzuela, and H. Milchberg, "Full path single-shot imaging of femtosecond pulse collapse in air turbulence," Opt. Lett. **45**, 2518 (2020).

[17] E. Rosenthal, N. Jhajj, I. Larkin, S. Zahedpour, J. Wahlstrand, and H. Milchberg, "Energy deposition of single femtosecond filaments in the atmosphere," Opt. Lett. **41**, 3908 (2016).

[18] E. Rosenthal, I. Larkin, A. Goffin, T. Produit, M. Schroeder, J.–P. Wolf, and H. Milchberg, "Dynamics of the femtosecond laser-triggered spark gap," Opt. Express **28**, 24599 (2020).

[19] Y.E. Geints, A.A. Zemlyanov, "Filamentation of ultrashort laser pulse train in air," Atmos. Ocean Opt. **31**, 112 (2018).

[20] V. Markov (private communications).

[21] D. Reyes, H. Kerrigan, J. Peña, N. Bodnar, R. Bernath, M. Richardson, and S.R. Fairchild, "Temporal stitching in burst-mode filamentation," Jour. of the Opt. Soc. of America B **36**(10), G52 (2019).

[22] D.J. Cook and R.M. Hochstrasser, "Intense terahertz pulses by four-wave rectification in air," Opt. Lett. **25**, 1210 (2000).

[23] K.Y. Kim, J H. Glownia, A. J. Taylor, and G. Rodriguez, "Terahertz emission from ultrafast ionizing air in symmetry-broken laser fields," Opt. Express **15**, 4577 (2007).

[24] G. Blair, V. Markov, P. Sprangle, *Generation of RF radiation by laser pulse trains in air*, Proc. SPIE 12237, Laser Communication and Propagation through the Atmosphere and Oceans XI, San Diego, CA (30 September 2022).

[25] S.A. Uryupin and A.A. Frolov, "Generation of low-frequency radiation by laser pulse trains in air," Jour. of Exp. and Theor. Phys. **114**(5), 878 (2012).

[26] M.N. Shneider and R.B. Miles, "Coherent microwave radiation from a laser induced plasma," Appl. Phys. Lett. **101**(26), 264105 (2012).

[27] C. D'Amico, A. Houard, M. Franco, B. Prade, and A. Mysyrowicz, "Coherent and incoherent radial THz radiation emission from femtosecond filaments in air," Opt. Express **15**, 15274 (2007).

[28] R. Schwartz, D. Woodbury, J. Isaacs, P. Sprangle, and H. Milchberg, "Remote detection of radioactive material using mid-IR laser-driven electron avalanche," Sci. Adv. **5**, eaav6804 (2019).

[29] L.G. Christophorou, *Atomic and Molecular Radiation Physics*, (Wiley-Interscience, 1971), pg. 530.

[30] Y.S. Dimant, G.S. Nusinovich, P. Sprangle, J. Penano, C.A. Romero-Talamas, and V.L. Granatstein , "Propagation of gamma rays and production of free electrons in air," J. of Appl. Phys. **112**, 083303 (2012).

[31] J. Isaacs, C. Miao, and P. Sprangle, "Remote monostatic detection of radioactive material by laser-induced breakdown," Phys. Plasmas **23**, 033507 (2016).

[32] Y.B. Zel'dovich and Y.P. Raizer, *Physics of Shock Waves and High Temperature Hydrodynamic Phenomena,* (Dover, Mineola, NY, 2002), pg. 342, 388, 389.

[33] J. Jackson, *Classical Electrodynamics*, (Wiley, 1998).

[34] A. Zangwill, *Modern Electrodynamics*, (Cambridge University Press, 2012).

[35] P. Sprangle, B. Hafizi, H. Milchberg, G. Nusinovich, and A. Zigler, "Active remote detection of radioactivity based on electromagnetic signatures," Phys. Plasmas **21**(1), 013103 (2014).

[36] E.S. Tanenbaum**,** *Plasma Physics*, **(**McGraw-Hill, Blacklick, OH, 1967).

[37] R. Boyd, *Nonlinear Optics*, (Academic Press, 2008).

[38] G. Blair, V. Markov, P. Sprangle, *Low Intensity Laser Pulse Train Propagation in Air: Part I: Analysis and Simulations*, Proc. SPIE 12691, Laser Communication and Propagation through the Atmosphere and Oceans XII, San Diego, CA (2023).

[39] V. Markov, I. Marienko, G. Blair, P. Sprangle, *Low Intensity Laser Pulse Train Propagation in Air: Part II: Experimental Studies*, Proc. SPIE 12691, Laser Communication and Propagation through the Atmosphere and Oceans XII, San Diego, CA (2023).

[40] M. Rodriguez, R. Bourayou, G. Mejean, J. Kasparian, J. Yu, E. Salmon, A. Scholz, B. Stecklum, J. Eisloffel, U. Laux, A.P. Hatzes, R. Sauerbrey, L. Woste, and J.-P. Wolf, "Kilometer-range nonlinear propagation of femtosecond laser pulses," Phys. Rev. E **69**, 036607 (2004).

[41] S. Hosseini, O. Kosareva, N. Panov, V.P. Kandidov, A. Azarm, J.-F. Daigle, A. B. Savel'ev, T.-J. Wang, and S.L. Chin, "Femtosecond laser filament in different air pressures simulating vertical propagation up to 10 km," Laser Phys. Lett. **9**, 868 (2012).

[42] Y.E. Geints., "Pressure scaling of femtosecond laser filamentation in air: prospects for long-range atmospheric propagation," Opt. Commun. **573**, 131007 (2024).

[43] D. Thul, R. Bernath, N. Bodnar, H. Kerrigan, D. Reyes, J. Pena, P. Roumayah, L. Shah, D. Maukonen, J. Bradford, M. Baudelet, S. Rostami Fairchild, and M. Richardson, "The mobile ultrafast high energy laser facility," Opt. Lasers Eng. **140**, 106519 (2021).

[44] Y.-Y. Ma, X. Lu, T.-T. Xi, Q.-H. Gong, and J. Zhang, "Widening of long-range femtosecond laser filaments in turbulent air," Opt. Express **16**(12), 8332 (2008).

[45] Y. Hu, J. Nie, K. Sun, L. Wang, "Filamentation of femtosecond laser pulse influenced by the air turbulence at various propagation distances," Opt. Commun. **383**, 281 (2017).

[46] M. Helle, G. DiComo, S. Gregory, A. Mamonau, D. Kaganovich, R. Fischer, J. Palastro, S. Melis, and J. Peñano, "Beating optical-turbulence limits using high-peak-power lasers," Phys. Rev. Appl. **12**, 054043 (2019).

[47] R.L. Fante, "Electromagnetic beam propagation in turbulent media," in *Proceedings of IEEE* **63**, 1669 (1975).

[48] L.C. Andrews and R.L. Phillips, *Laser Beam Propagation through Random Media* (SPIE Press, Bellingham, WA 2005).

[49] A. Jurado-Navas, J.M. Garrido-Balsells, M. Castillo-Vazquez, and A. Puerta-Notario, "Numerical model for the temporal broadening of optical pulses propagating through weak atmospheric turbulence," Opt. Lett. **34**(23), 3662 (2009).

[50] D.E.T.T. Sjin Kelly and L.C. Andrews, "Temporal broadening and scintillations of ultrashort optical pulses," Waves in Random Media **9**, 3 (1999).

[51] E.D. Caldwell, W.C. Swann, J.L. Ellis, M.I. Bodine, C. Mak, N. Kuczun, N.R. Newbury, L.C. Sinclair, A. Muschinski, and G.B. Rieker, "Optical timing jitter due to atmospheric turbulence: comparison of frequency comb measurements to predictions from micrometeorological sensors," Opt. Express **28**(18), 26661 (2020).

[52] C.Y. Young, L.C. Andrews, and A. Ishimaru, "Time-of-arrival fluctuations of a space-time Gaussian pulse in weak optical turbulence: an analytic solution," Appl. Opt. **37**(33), 7655 (1998).

[53] G.P. Berman, V.N. Gorshkov, and S.V. Torous, “Scintillation reduction for laser beams propagating through turbulent atmosphere,” J. Phys. B.: At. Mol. Opt. Phys. **44**(5), 055402 (2011).

[54] L.D. Landau, E.M. Lifshitz and L.P. Pitaevskiĭ, *Electrodynamics of Continuous Media* (Butterworth-Heinemann, Oxford, UK, 2008).

[55] G.P. Agrawal, *Nonlinear Fiber Optics*, 5th ed. (Elsevier Inc., 2013).

[56] Y.E. Geints, A.A. Zemlyanov, A.A. Ionin, S.I. Kudryashov, L.V. Seleznev, D.V. Sinitsyn, and E.S. Sunchugasheva, “Nonlinear propagation of a high-power focused femtosecond laser pulse in air under atmospheric and reduced pressure,” Quantum Electron. **42**, 319 (2012).

[57] S.V. Chekalin and V.P. Kandidov, “From self-focusing light beams to femtosecond laser pulse filamentation,” Phys.-Usp. **56**, 123 (2013).

[58] L. Berge, S. Skupin, F. Lederer, G. Mejean, J. Yu, J. Kasparian, E. Salmon, J.P. Wolf, M. Rodriguez, L. Woste, R. Bourayou, and R. Sauerbrey, “Multiple filamentation of terawatt laser pulses in air,” Phys. Rev. Lett. **92**, 225002 (2004).

[59] N.A. Panov, O.G. Kosareva, and I.N. Murtazin, “Ordered filaments of a femtosecond pulse in the volume of a transparent medium,” J. Opt. Technol. **73**(11), 778 (2006).

[60] E. Mitina, D. Uryupina, N. Zhidovstev, R. Volkov, O. Kosareva, and A. Savel’ev, “Long-range robust multifilament arrays from terawatt femtosecond beam,” Laser Phys. Lett. **19**(1), 015201 (2021).

[61] S. Champeaux and L. Bergé, “Long-range multifilamentation of femtosecond laser pulses versus air pressure,” Opt. Lett. **31**(9), 1301 (2006).

[62] P.A. Zhokhov and A.M. Zheltikov, “Scaling laws for laser-induced filamentation,” Phys. Rev. A **89**, 043816 (2014).

[63] P. Sprangle, E. Esarey, and B. Hafizi, “Propagation and stability of intense laser pulses in partially stripped plasmas,” Phys. Rev. E **56**, 5894 (1997).

[64] J. Peñano, B. Hafizi, A. Ting, and M. Helle, “Theoretical and numerical investigation of filament onset distance in atmospheric turbulence,” J. Opt. Soc. Am. B **31**(5), 963 (2014).

[65] P. Sprangle, B. Hafizi, and J. Peñano, “Laser pulse modulation instabilities in plasma channels,” Phys. Rev. E **61**, 4381 (2000).

[66] C.E. Max, J. Arons, and A.B. Langdon, “Self-modulation and self-focusing of electromagnetic waves in plasmas,” Phys. Rev. Lett. **33**, 209 (1974).

[67] B. Hafizi, J. Peñano, J.P. Palastro, R.P. Fischer, and G. DiComo, "Laser beam self-focusing in turbulent dissipative media," Opt. Lett. **42**(2), 298 (2017).

[68] B. Hafizi, J. Isaacs, J. P. Palastro, and J. Peñano, "Nonlinear propagation of chirped laser pulses through a dispersive and turbulent atmosphere," J. Opt. Soc. Am. B **41**(6), 1457 (2024).

[69] J. Peñano, J.P. Palastro, B. Hafizi, M.H. Helle, G.P. DiComo, "Self-channeling of high-power laser pulses through strong atmospheric turbulence," Phys. Rev. A **96**, 013829 (2017).

[70] H. Elder, A. Khizhnyak, V. Markov, and P. Sprangle, *Nonlinear dynamics of the laser spot size and pulse duration in turbulence*, in Proc. of SPIE 11834, Laser Communication and Propagation through the Atmosphere and Oceans X, San Diego, CA (2021).

[71] P.J. Wrzesinski, D. Pestov, V.V. Lozovoy, J.R. Gord, M. Dantus, and S. Roy, "Group-velocity-dispersion measurements of atmospheric and combustion-related gases using an ultrabroadband-laser source," Opt. Express **19**(6), 5163 (2011).

[72] P. Sprangle, A. Ting, J. Peñano, R. Fischer, and B. Hafizi, "Incoherent combining and atmospheric propagation of high-power fiber lasers for directed-energy applications," IEEE Jour. of Quan. Elec. **45**(2), 138 (2009).

[73] P.W. Milonni and J.H. Eberly, *Laser Physics*, (John Wiley and Sons, Inc., 2010).

[74] J. Kasparian, R. Sauerbrey, and S.L. Chin, "The critical laser intensity of self-guided light filaments in air," Appl. Phys. B: Lasers Opt. **71**, 877 (2000).

[75] A. Talebpour, J. Yang, and S.L. Chin, "Semi-empirical model for the rate of tunnel ionization of N_2 and O_2 molecule in an intense Ti:Sapphire laser pulse," Opt. Commun. **163**, 29 (1999).

[76] M.C. Kelley, *The Earth's Ionosphere: Plasma Physics and Electrodynamics*, (Academic Press Inc., 1989).

[77] G.C. Valley, "Isoplanatic degradation of tilt correction and short-term imaging systems," Appl. Opt. **19**(4), 574 (1980).

[78] G.A. Fabrizio, *High frequency over-the-horizon radar: fundamental principles, signal processing, and practical applications* (McGraw Hill, New York, 2013).

[79] B.Y. Liu, "Over-the-horizon radar system performance and analysis," Master's thesis, Naval Postgraduate School, 2007.

[80] K. Yeh and C. Liu, "Ionospheric effects on radio communication and ranging pulses," IEEE Transactions on Antennas and Propagation **27**(6), 747 (1979).

[81] J.M. Goodman, *Effect of the Ionosphere on Space Systems and Communications*, Naval Research Laboratory, Washington, D.C. (1975).

[82] J.M. Goodman and J. Aarons, "Ionospheric effects on modern electronic systems," in *Proceedings of the IEEE* **78**(3), 512 (1990).

[83] D.E. Hastings, “A review of plasma interactions with spacecraft in low Earth orbit,” J. Geophys. Res., **100**(A8), 14457 (1995).

[84] P.C. Anderson, “Characteristics of spacecraft charging in low Earth orbit,” J. Geophys. Res. **117**, A07308 (2012).

[85] M.v.d. Kamp, P.S. Cannon, and M. Terkildsen, "Effect of the ionosphere on defocusing of space-based radars," Radio Science **44**(01), 1 (2009).

[86] L. Liu, W. Wan, Y. Chen, and H. Le, “Solar activity effects of the ionosphere: A brief review,” Chin. Sci. Bull. **56**, 1202 (2011).

[87] A.P. Mitra, *Ionospheric Effects of Solar Flares* (Springer, Dordrecht, 1974).

[88] M. Thumm, “State-of-the-art of high-power gyro-devices: 2025 update,” Journal of Infrared, Millimeter, and Terahertz Waves **46**, 35 (2025).